Title
Modeling of Lead Rubber Bearings at Large Strains and Effects on Structural Response

Author
Marquez, Joaquin Fabian

Publication Date
2021

UNIVERSITY OF CALIFORNIA SAN DIEGO

Modeling of Lead Rubber Bearings at Large Strains and Effects on Structural Response

A dissertation submitted in partial satisfaction of the

requirements for the degree

Doctor of Philosophy

in

Structural Engineering

by

Joaquin Fabian Marquez

Committee in charge:

Professor Gilberto Mosqueda, Chair
Professor Jiun-Shyan Chen
Professor Michael Holst
Professor Pui-Shum Shing
Professor Chia-Ming Uang

2021

The Dissertation of Joaquin Fabian Marquez is approved, and it is acceptable in quality and form for publication on microfilm and electronically.

University of California San Diego

2021

DEDICATION

To my parents Ignacio Marquez and Martha Marquez who have made countless sacrifices and shown unconditional love to my brothers and me. To my father showing me what hard-work and dedication consist of by working at times 12-14 hour shifts to provide stability for our household. My mother for her immeasurable nurture and care for me always ensuring to provide us with every need. For ensuring I always did good in school, not being able to speak the language and courageously going to my school to ask how I was doing academically. For everything they did for us. Thank you.

To my grandparents, Augustin Galvez and Joaquin Marquez who passed away this past year. They were truly the first engineers in the family, quite literally building their homes and designing a better future for generations to come in the Galvez and Marquez family. For that I am forever grateful. Love and miss you. Rest in Peace.

TABLE OF CONTENTS

LIST OF FIGURES

LIST OF TABLES

ACKNOWLEDGEMENTS

I am grateful for the opportunity to work with incredible people during my PhD studies. The experiences shared with in this program were invaluable for aiding my intellectual and personal development.

Firstly, I would like to give my deepest gratitude to my advisor, Professor Gilberto Mosqueda for his guidance, support, and friendship. I am forever grateful for his advice and confidence in me. I am grateful for his encouragement when the tribulations of my PhD journey arose. Thank you.

I wanted to thank my committee Professor Chen, Professor Holst, Professor Shing, and Professor Uang for all their support and feedback.

I wanted to thank all my friends for all their unconditional support. I wanted to thank Dr. Alireza Sarebanha for being so inviting to our then research group, for all his advice and guidance. I would like to extend my gratitude to Dr. Manuel Vega and Lucas Deyglun for friendship and guidance. I would like to thank my research group Ricardo Bustamante and Claudio Contreras for their friendship and feedback. I would like to thank Dr. John Nieman for his endless support and guidance throughout my academic career.

I would like to thank my friends Parwiz Ahmadi, Fernando Altamirano, and Stephanie Macias for their support and their camaraderie.

I would like to thank my family my parents, Ignacio Marquez and Martha Marquez and brothers David Marquez and Jorge Marquez for their endless support and love. I would like to extend my thanks to the Marquez and Galvez family. I would like to thank my sister-in-law Araceli

Marquez, my cousins, Vanessa Galvez, Liliana Galvez, Omar Galvez, Beatriz Galvez, Andrew Preciado for their support and love.

Lastly, thank you Llesenia Aleman, for all your love and patience through this difficult journey. Thank you for all your support when I needed it most. Grateful to have you in my life.

Chapter 3,in part, is a reprint of the material as it appears in “Response of a Seismically Isolated Structure with Lead Rubber Bearings Considering Heating Effects.” Marquez, J. F., and Mosqueda, G., *Proceedings of the 11th National Conference in Earthquake Engineering, Earthquake Engineering Research Institute (2018).* The dissertation author was the primary investigator and author of this paper.

Chapter 4, in part, is a reprint of the material as it appears in “Modeling of Lead Rubber Bearings Under Large Cyclic Material Strains.” Marquez, J.F., Mosqueda, G., & Kim, M.K., *ASCE Journal of Structural Engineering (2021).* The dissertation author was the primary investigator and author of this paper.

Chapter 5, consists of only investigations conducted by the author of this dissertation, from material in “Considerations for modeling of base isolated nuclear power plants subjected to beyond design basis shaking.” Sarebanha, A., Marquez, J., Hughes, P., & Mosqueda, G., *Nuclear Engineering and Design (2021).* The dissertation author was the co-investigator and co-author of this paper.

VITA

2015	Bachelor of Science, University of California, Irvine
2017	Master of Science, University of California San Diego
2021	Doctor of Philosophy, University of California San Diego

PUBLICATIONS

Journal Papers:

Marquez, J.F., Mosqueda, G., & Kim, M.K. (2021). “Modeling of Lead Rubber Bearings Under Large Cyclic Material Strains.” *ASCE Journal of Structural Engineering*, 49 (12): 1197-1215.

Sarebanha, A., Marquez, J., Hughes, P., & Mosqueda, G. (2021). Considerations for modeling of base isolated nuclear power plants subjected to beyond design basis shaking. *Nuclear Engineering and Design*, *379*, 111236.

An, G., Kim, M., Jung, J.-W., Mosqueda, G., and Marquez, J. F. (2020). “Evaluation of Clearance to Stop Requirements in A Seismically Isolated Nuclear Power Plant.” *Energies*, 13(22), 6156.

Conference Papers:

Marquez, J.F., Mosqueda, G. (2020). “Advance Modeling of Lead Rubber Bearings Under High Strains with Experimental Verification” *17th World Conference on Earthquake Engineering, Sendai, Japan.*

Mosqueda, G., Marquez, J. F., and J. Hughes, P. (2019). “Modeling of Base Isolated Nuclear

Power Plant Subjected to Beyond Design Basis Shaking.” *Transactions, 25th International Conference on Structural Mechanics in Reactor Technology (SMiRT-25).*

Marquez, J. F., and Mosqueda, G. (2018). “Response of a Seismically Isolated Structure with Lead Rubber Bearings Considering Heating Effects.” *Proceedings of the 11th National Conference in Earthquake Engineering*, Earthquake Engineering Research Institute, Los Angeles, California

ABSTRACT OF THE DISSERTATION

Modeling of Lead Rubber Bearings at Large Strains and Effects on Structural Response

By

Joaquin Fabian Marquez

Doctor of Philosophy in Structural Engineering

University of California San Diego, 2021

Professor Gilberto Mosqueda, Chair

Seismic isolation is an effective method to mitigate the damaging effects of horizontal ground motions. The flexible layer, typically placed at the base of the structure, reduces forces transmitted from ground shaking at the expense of concentrated displacements at the seismic isolation layer. Base isolation systems within a basement of a building require a free clearance to allow for such displacements to occur. A surrounding moat wall can be placed to constrain the isolation devices from exceeding their displacement capacity. However, impact to the moat wall can be damaging to the structure with recent studies concluding that the required clearance to stop

(CS) specified by building design codes is insufficient for high consequence low-frequency ground motions.

The Lead Rubber Bearing (LRB) is widely used in practice for implementation of seismic isolation. Current models for LRB are not able to capture the salient characteristics of bearing behaviors observed in experimental data, especially under large displacement demands. Therefore, the large strain lead rubber bearing (LSLRB) model is proposed to better predict the response of base isolated structures under extreme earthquake shaking considering the combined effects of lead core heating, and material strain hardening in the lead and rubber. The LSRLB model was implemented in a full-scale Nuclear Power Plant (NPP) numerical model under earthquake loading and demonstrated to reduce displacement demands and lower velocities in the case of impact to a moat wall. Consideration of extending the moat wall clearance and allowing the bearings to reach strain hardening at large displacements showed to be effective in improving the overall seismic response under large ground motions. In terms of the effect of bearing models on the critical internal contents of NPPs, the LSLRB model showed a reduction in floor spectral accelerations throughout the superstructure compared to current models utilized in practice. The results presented are also highly dependent on modeling of the moat wall impact. Current models are reviewed and extended to better predict the amount of moat wall deformation considering the concrete retaining wall, soil contribution and coefficient of restitution.

Chapter 1 INTRODUCTION

Seismic isolation systems are utilized to elongate the lateral vibration period of a building structure as a means of protecting the structure from seismic shaking. The added flexibility, typically placed at the base of the structure, provides many benefits for isolated structures. First, for short period structures, it elongates the fundamental period and reduces the effective seismic forces by shifting the vibration frequency away from the most damaging higher frequency earthquake shaking. Second, the isolation system can inherently dissipate significant energy or supplemental damping (i.e. dampers) can be added to limit displacements at the isolation level and the shear forces in the superstructure. Lastly, the increase in flexibility results in larger displacement demands, however these displacements are confined to the bearings themselves that can endure large deformations without permanent damage. For buildings, the base isolation system is typically placed within a moat at the basement level to allow for these displacements to be achieved without obstructions. A surrounding moat wall can function as a stop to limit isolator displacements and prevent their failure. However, recent investigations of moat wall clearance requirements as specified by building design codes have indicated that the design displacements may be insufficient for acceptable performance of isolated buildings under large earthquakes.

Two types of bearings are commonly used for base isolation: elastomeric and friction bearings. This dissertation focuses on modeling of a type of elastomeric bearing known as the Lead Rubber Bearing (LRB), to more accurately capture the behaviors produced by these bearings at large strains. A new model is proposed and compared to experimental data from large amplitude cyclic testing of two identical large bearings under a constant axial load to focus on the material nonlinear response. Capturing the behavior of the bearings is highly dependent on the variation of axial load and the size of the bearing (i.e. shape factors) which is not examined here (Sheridan et al. 2012). The benefits of the proposed model in terms of predicting maximum displacements of the isolation system and the potential for impact to moat walls under high consequence low-frequency earthquakes is examined.

1-1 Lead Rubber Bearings

The use of lead rubber bearings (LRB) for seismic isolation was proposed in 1974 in New Zealand by Skinner et al. (1974), and since then they have been the subject of various research studies. They were developed in detail by Robinson and Tucker (1977) experimentally demonstrating that the isolation system performed as anticipated. Since then, LRBs have become one of the most widely applied devices for seismic isolation. The LRB consists of alternating thin rubber layers and steel shims that allow for horizontal flexibility while the steel shims prevent bulging of the rubber and produce a high vertical stiffness. The lead is typically placed at the center of the bearing as a form of hysteretic energy dissipation. The lead core's material makeup allows for the mechanical properties of the lead to be recovered within minutes of previous excitations and allows for repeated use of the LRB under multiple earthquakes. The rubber shims are made of an unfilled elastomer typically known as natural rubber. The mechanical behavior of the elastomer is well established at low to intermediate strains, and because of its low damping properties, it is often simplified as an elastic material.

Although the behavior of LRBs have been heavily researched, one persistent challenge is capturing the exact response of bearings due to various factors such as scragging, rate effects, contamination, temperature, initial lead hardening, and distance travelled. Current design codes conservatively account for these complex behaviors in an estimated sense, using property modification factors such as in ASCE 7-16 (2017). Furthermore, simple models currently implemented in software and widely used by practicing engineers seem to capture the response of LRBs accurately for design level earthquake shaking. However, a recent emphasis of examining the response of seismically isolated buildings under extreme earthquake shaking requires more advanced models that capture the aforementioned behaviors.

Ideally, a mathematical model for LRBs should capture all the various nonlinear behaviors observed at small to large strains: scragging, rate effects, initial lead hardening, contamination, temperature, and distance travelled. Modeling all these behaviors is impractical, therefore being able to strategically select the features that are most important towards determining key response parameters is critical. The most practical approach to pinpointing the contributions of the complex behavior demonstrated by LRBs is to separate the main components and understand their key material properties.

The rubber portion of LRBs at low to intermediate strains of the model can simply be modeled as an elastic material, however at higher strains it develops hardening and softening effects, behaving similar to that of the High Damping Rubber (HDR) (Diani et al. 2009). Rubber damage referred to as scragging and Mullins effect, are more prominent at higher strains and may consequently develop hardening and softening ‘unloading’ effects that result in a widening of the hysteresis at peak displacements. Regardless of the root of this phenomenon, these nonlinear effects need to be accounted for when conducting analysis of critical structures (Dall'Asta and Ragni, 2008).

The heating of the lead core has shown to be an important behavior of the LRB, it is the passive energy dissipation component of the bearing and highly influential in the overall behavior. A recently developed model in OpenSees (2014) named *LeadRubberX*, has the ability of predicting the strength degradation due to heating of the lead core. One feature that has not been fully identified is the initial lead hardening of the lead core and has been speculated to occur due to high-speed error or instrumental error. However, accounting for this initial lead hardening is beneficial in determining the actual characteristic strength of the LRB.

1-2 Research Objectives

A key response parameter in the analysis of seismically isolated structures is the displacement at the isolation level. The displacement demands on the isolation system and LRBs can be limited by a surrounding moat wall and exceeding this displacement limit results in impact causing possible detrimental effects on the structural response. Current design standards, specifically for NPPs, aim to limit the occurrence of impact by specifying the minimum required clearance to stop (CS) as the lognormal 90th percentile horizontal displacement for Beyond Design Basis Earthquake (BDBE) shaking defined as a high consequence low frequency earthquake event with a return period of 100,000 years (U.S. NRC 2014). Recent studies have shown that impact of an isolated structure to a moat wall can result in a significant amplification in the seismic response of the structure (Komodromos 2008; Masroor and Mosqueda 2015; Sarebanha et al. 2018). For the isolation systems, recent studies conducted on various structural systems by Kitayama and

Constantinou (2018, 2019), discuss the significance of the stiffening behavior of the isolators and restraints to improve the performance of isolated structures. Increasing the displacement capacity of the isolators, resulted in lower probability of collapse when considering Maximum Credible Earthquake (MCE) ground motions (ASCE 2017) or a high consequence low frequency event.

One key objective of this dissertation is to examine LRB subjected to large displacement demands and to develop accurate models capable of capturing the various nonlinear behaviors ranging from initial lead hardening at small displacements to rubber hardening and damage effects at large displacements. Reliable models can better predict displacement demands, and the potential for minimizing or reducing the velocity before impact to moat walls, thus reducing the damage to the superstructure and contents. In the case of impact, an extension of an existing moat wall model is further explored to accurately predict the amount of moat wall deformation given an impact velocity and moat wall properties.

1-3 Organization of Thesis

An overview of the sequence of each chapter and brief summaries are provided in this section. In Chapter 2, existing experimental work is examined to identify the complex behavior of LRBs and the sources of the various nonlinear behaviors. The various existing bearing models are reviewed to gain insight on their capabilities and limitations. Finally, recommendations for advancement in LRB models are proposed.

In Chapter 3, the recently developed *LeadRubberX* model is examined in order to understand its performance under earthquake excitations. The model is compared against a Bouc-Wen (smooth bilinear) model using ASCE code requirements by applying property modification factors to observe if the *LeadRubberX* model can provide similar conservative results as the code.

The *LeadRubberX* model was found to be sensitive to long-duration ground motions resulting in excessive displacements, caused by excessive heating of the lead core, which resulted in exceedance of the bounds.

Chapter 4 presents experimental data to examine the nonlinear behavior in a large sized LRB subjected to large strains. A combination of existing bearing models is utilized to fully capture experimental data. A nonlinear time history analysis (NLRHA) is conducted on a SDOF system with the novel parallel model named, Large Strain Lead Rubber Bearing (LSLRB), and is compared against current LRB models to demonstrate differences in response prediction with these models.

In Chapter 5, the parallel model is implemented for nonlinear response history analysis (NLRHA) on a full-scale Nuclear Power Plant (NPP) model to understand the potential benefits of including the nonlinear behaviors observed in LRBs. The clearance to stop (CS), distance to the moat wall, will be examined in order to observe any benefits of the LRBs hardening effects may have on reducing impact velocities and consequently reducing superstructure demand. For impacts, an extension of a previous moat wall deformation prediction model is revisited to predict the moat wall deformation given an impact velocity and the moat wall properties.

In Chapter 6, an improvement to the parallel model named Large Strain Lead Rubber Bearing (LSLRB), is extended to account for bidirectional behavior. The model includes the ability to capture initial lead hardening, lead core heating, high strain hardening, anisotropic damage behavior, and softening “unloading” effects from scragging and Mullins effects. The advantage of the LSLRB model is that the calibration is done for one set of parameters for various levels of strains and strain rates. The model is implemented in OpenSees software and a NLRHA is conducted on a SDOF system in order to understand the behavior compared to other simpler models.

In Chapter 7, a NLRHA is conducted on a full-scale Nuclear Power Plant (NPP) model in OpenSees with the implementation of the novel LSLRB model. The analysis provides insight for the potential benefits of extending the moat wall, and in preventing or reducing impact velocities to the moat wall. Although recent studies have shown extending the moat wall may be desirable, this analysis helps identify at what levels of strain this may be useful and the costs and benefits of allowing large strains for the LSLRB model. The previously updated moat wall deformation prediction model is considered and proves to be a viable design solution to provide conservative predictions.

Chapter 8, summarizes the research work that was conducted for this dissertation, emphasizes the main contributions and provides recommendations for future work.

1-4 References

ASCE. (2017). *Minimum Design Loads and Associated Criteria for Buildings and Other Structures*. ASCE/SEI Standard 7, Reston, VA.

Dall'Asta, A., and Ragni, L. (2008). "Nonlinear behavior of dynamic systems with high damping rubber devices." *Engineering Structures*, Elsevier Ltd, 30(12), 3610–3618.

Diani, J., Fayolle, B., and Gilormini, P. (2009). "A review on the Mullins effect." *European Polymer Journal*, Elsevier Ltd, 45(3), 601–612.

Kitayama, S., and Constantinou, M. C. (2018). "Collapse performance of seismically isolated buildings designed by the procedures of ASCE/SEI 7." *Engineering Structures*, Elsevier, 164(March), 243–258.

Kitayama, S., and Constantinou, M. C. (2019). "Probabilistic seismic performance assessment of seismically isolated buildings designed by the procedures of ASCE/SEI 7 and other enhanced criteria." *Engineering Structures*, Elsevier Ltd, 179, 566–582.

Komodromos, P. (2008). "Simulation of the earthquake-induced pounding of seismically isolated buildings." *Computers and Structures*.

Masroor, A., and Mosqueda, G. (2015). "Assessing the collapse probability of base-isolated buildings considering pounding to moat walls using the FEMA P695 Methodology." *Wiley Earthquake Engineering and Structural Dynamics*, 31(4), 2069–2086.

OpenSees. (2014). "Open system for earthquake engineering (Version 2.4.4)."

Robinson, W. H., and Tucker, A. G. (1977). "A lead-rubber shear damper." *Bulletin of the New Zealand National Society for EarthquakeEngineering*.

Sarebanha, A., Mosqueda, G., Kim, M. K., and Kim, J. H. (2018). "Seismic response of base isolated nuclear power plants considering impact to moat walls." *Nuclear Engineering and Design*.

Sheridan, P. M., James, F. O., and Miller, T. S. (2012). "Design of Components." *Engineering with Rubber*, A. N. Gent, ed., Carl Hanser Verlag GmbH & Co. KG, München, 259–293.

Skinner, R. I., Beck, J. L., and Bycroft, G. N. (1974). "A practical system for isolating structures from earthquake attack." *Earthquake Engineering & Structural Dynamics*, 3(3), 297–309.

U.S. Nuclear Regulatory Commission. (2014). "Design Response Spectra for Seismic Design of Nuclear Power Plants." *Regulatory Guide No. 1.60, Revision 2*.

Chapter 2 REVIEW OF MODELS AND EXPERIMENTS FOR LEAD RUBBER BEARING

In an effort to develop reliable bearing models that are able to capture the behavioral characteristics of lead-rubber bearings (LRB) under large amplitude cyclic displacements, existing experimental work of such characteristics are first reviewed. Characteristics of interest include the strength reduction in the bearing due to the heating of the lead core as well as initial lead core hardening. With respect to the behavior of the rubber, a model that can capture high strain hardening effects as well as the softening “unloading” effects is desired. While certain models capture key characteristics, a model demonstrating to capture the full complex response of LRBs was not identified. Before remedying extant deficiencies, a clear understanding of existing experimental work is first reviewed in order to pinpoint the sources of the nonlinear behaviors exhibited in LRBs. Then, examination of existing bearing models is conducted to understand the capabilities and the limitations these models may have in capturing these nonlinear effects.

2-1 Existing Experiments

In this section, experiments of LRBs will be examined to identify the complex behaviors that the bearings may exhibit. LRBs have continuously shown to develop various nonlinear characteristics ranging from the initial lead core hardening followed by degradation from heating of the lead core. Additionally, at larger strain levels, the rubber in LRBs develops hardening, softening “unloading” effects, and anisotropic effects. Existing experimental work will be presented in order to identify the various nonlinear behaviors.

2-1-1 Lead core behavior

Many experimental tests have been conducted on LRBs since they were first introduced by Skinner et al. (1974). Experimental data is a natural way to gain knowledge and understanding of the behavior of such composite systems. Shear tests of solely the lead core were conducted in order to understand the behavior of the lead core itself (Aramaki et al. 2004). The dimensions of the lead specimen are shown in Figure 2-1a, and the resulting hysteresis from a cyclic shear test is shown in Figure 2-1b. The lead specimen clearly undergoes strength degradation associated with heating of the lead material. Moreover, in the initial cycle, material strain hardening can be observed and is often overlooked in experimental results of LRBs. Some researchers have speculated that this initial lead hardening phenomenon may occur due to instrumental error or high-speed testing. However, this slow experiment (at 0.1Hz) along with others, oppose this speculation as the initial lead hardening phenomena have been observed in other various experimental tests of LRBs (Eem and Hahm 2019; Kalpakidis and Constantinou 2009a; McVitty and Constantinou 2015; Sanchez et al. 2013; Tyler and Robinson 1984b).

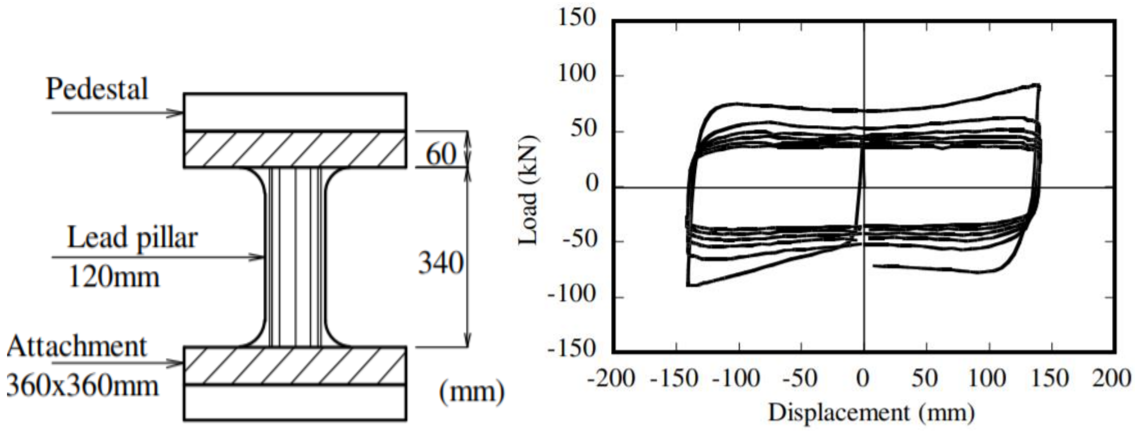

a.) b.)

Figure 2-1 Fatigue testing at 0.1Hz a.) Lead Core Specimen b.) Load-Displacement Hysteresis (Aramaki et al. 2004)

In Figure 2-2, the force-displacement loops are shown for a cyclic shear test of a LRB demonstrating the same variation in strength as the lead specimen. A decrease in the width of the hysteresis by cycle is evident due to the strength degradation of the lead core. Furthermore, the initial loading cycle in the negative direction demonstrates an initial hardening of the lead core. This phenomenon has not been investigated for LRB and may be of importance especially for short duration near fault type ground motions having few cycles of response. Kalpakidis and Constantinou (2009a) investigated the heating of the lead core in LRBs from cyclic loading by utilizing thermodynamic equations to find the relationship between shear displacements and strength degradation due to the heating of the lead core (described in section 2-2-2-1).

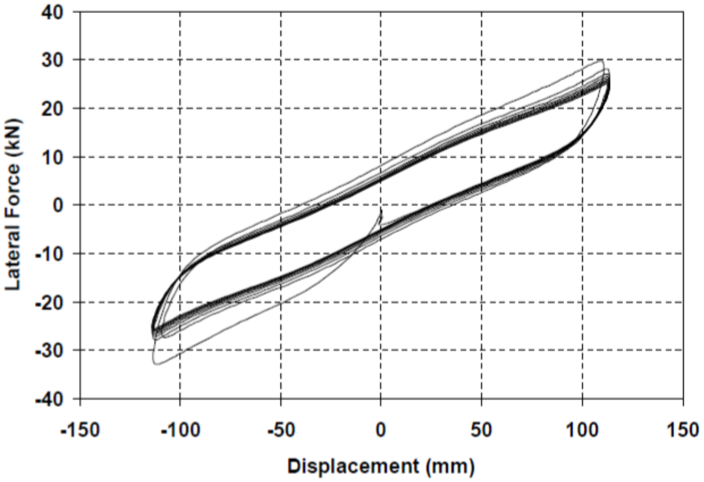

Figure 2-2 Force-Displacement Loops of LRB Load=67kN, Displacement Amplitude=114mm and Frequency =0.5Hz (Kalpakidis and Constatinou 2008)

2-1-2 Rubber Behavior

Natural rubber exhibits linear elastic behavior at low to medium strains, however at higher strains it begins to develop hardening effects behaving similar to High Damping Rubber (HDR) (Diani et al. 2009). Harwood and Payne were able to demonstrate that natural rubber (NR) experiences the same level of softening effects when the natural rubber sustains the same amount of stress as the HDR specimen (Harwood et al. 1965; Mullins 1969). As shown in Figure 2-3, the natural rubber undertaken to the same level of stress as the NR filled with 80 to 20 phr (Parts per Hundred Rubber**)** of carbon black (CB) experienced similar softening effects, however only at larger strains. While the focus of this dissertation is on LRBs, experimental observations and models for HDR bearings will also be examined since similar nonlinear behavior is observed in LRBs only at large strains.

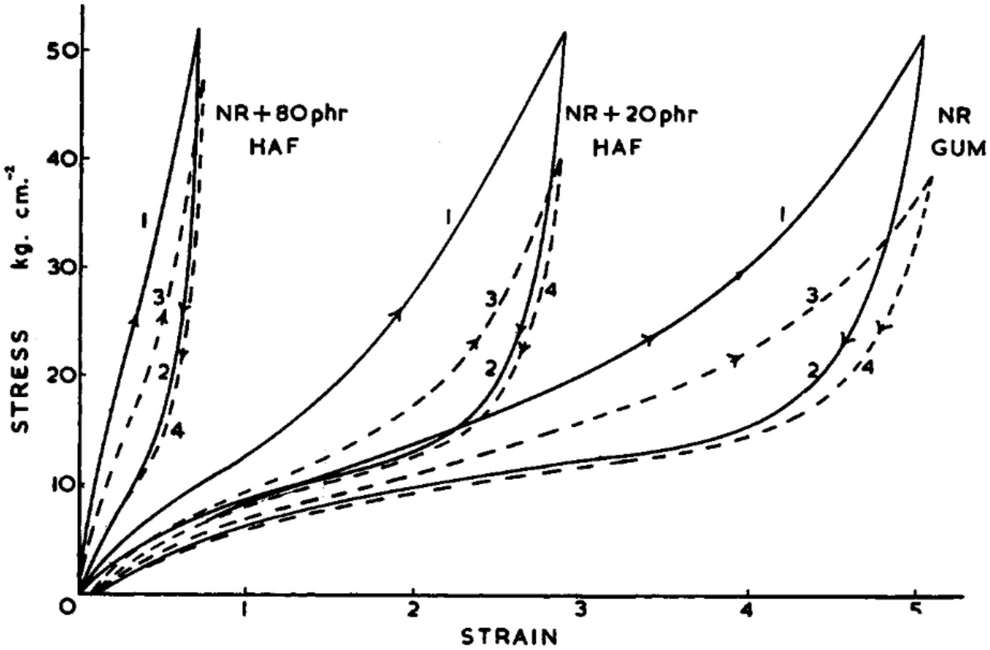

Figure 2-3 Stress (referred to original cross-section) versus strain for (a) gum vulcanizate, (b) vulcanizate containing 20 phr HAF, and (c) vulcanizate containing 80 phr HAF: (I) initial stressing curve; (2) first retraction curve; (3) second stressing curve; (4) second retraction curve (Harwood et al. 1965)

Ishida et al. (1991) tested three identical bearings: a natural rubber bearing (NRB), a lead rubber bearing (LRB), and a high damping rubber (HDR) bearing. The purpose of the study was to gain insight of the bearings undergoing various loading types and deform the bearing to large shear deformations to understand the safety margins and ultimate characteristics (or failure). In Figure 2-4, the loading types applied on the NRB and LRB were a static cyclic, static monotonic, and dynamic monotonic testing. The authors of this study deduced important implications of these bearings: regardless of the strain rate and the amount of previous cycles (or damage), the bearing failed at 500% shear strain. First, it is important to note that both the NRB and the LRB exhibit rubber hardening at these large strains. Second, the pronounced softening ‘unloading’ effects can be observed for both bearings which may be attributed to Mullins effect or scragging damage.

More recently, tests were conducted on large LRBs for NPPs imposing various characterization tests of up to 500% shear strain without failure, exhibiting various nonlinear behaviors such as rubber hardening and softening ‘unloading’ effects along with lead core strength degradation due to heating and initial lead hardening (Eem and Hahm 2019). An et al. (2020) conducted many experimental tests on LRBs shearing the bearing with various axial loads to failure, resulting in failures occurring at greater than 400% shear strain, implicating the LRBs extensive capacity. These tests are presented in more detail later as they are used for the development of the models proposed here.

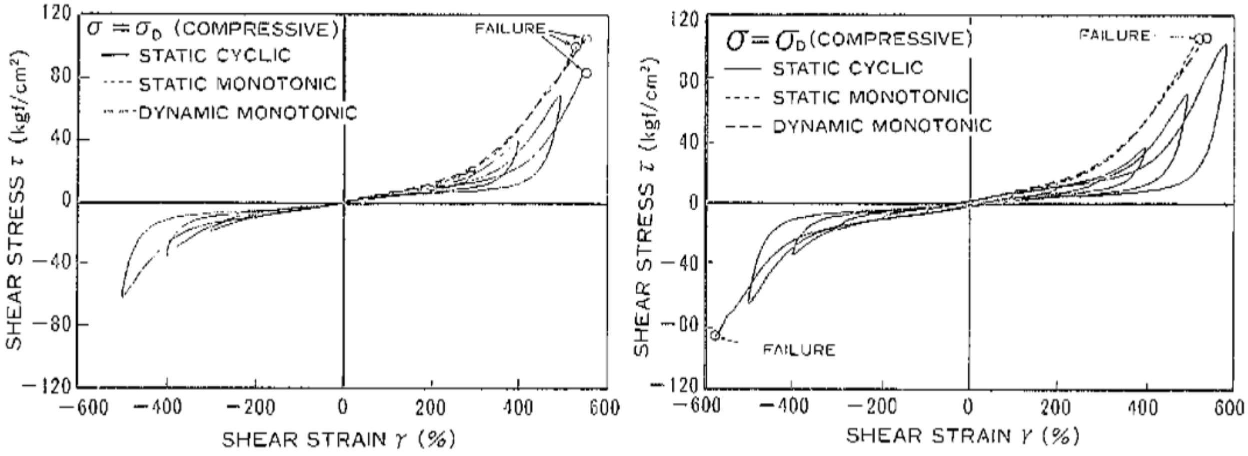

(a.)NRB (b.) LRB

Figure 2-4 Shear stress-strain curves a.) Natural Rubber Bearing (NRB) b.) Lead Rubber Bearing (LRB) (Ishida et al. 1991)

Experimental tests of single layer HDR specimens were tested in various directions and it was recognized that the accumulated rubber damage behaved in an anisotropic manner. Accordingly, a model capable of capturing such effects was proposed by Tubaldi et al. (2017). Ragni et al. (2018) to further understand the anisotropic behavior of the HDR material, a circular pad was imposed to the shear strain history shown in Figure 2-5. The idea of imposing the strain history was to observe the cyclic shear response in the reference direction versus the rotated direction with increasing shear strain.

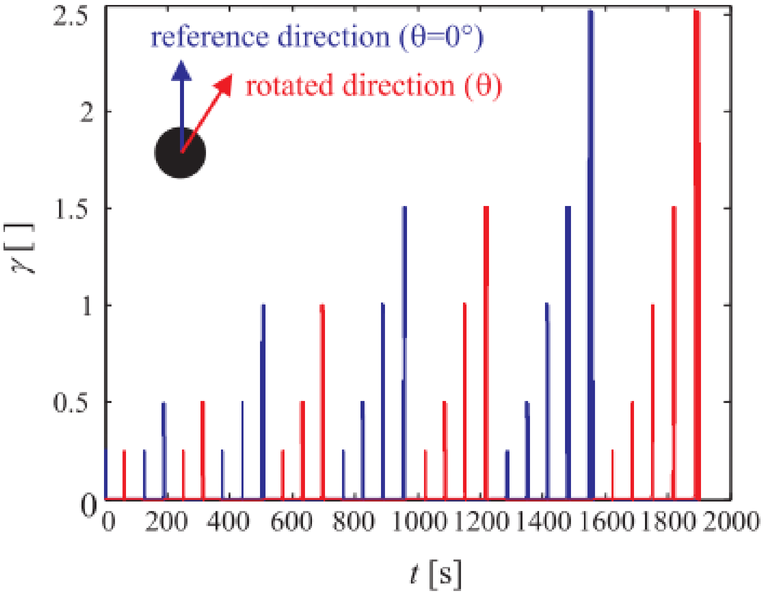

Figure 2-5 Imposed strain history of the rotated double shear test (Ragni et al. 2018)

With the imposed shear strain history, the shear stress of the rubber specimen was obtained showing anisotropic behavior (Figure 2-6). The authors concluded that when the rubber specimen is rotated by 180° (Figure 2-6f) the response is essentially equivalent to the reference direction. However, when the bearing is displaced in the same direction (Figure 2-6a) evident damage had developed in the bearing and as the angle increased the amount of damage decreased. These experimental results verify that the cumulative damage is in fact anisotropic and implementing the idea of representative directions (Freund and Ihlemann 2010) along with damage formulations developed in (Tubaldi et al. 2017) were deemed necessary to account for such effects for calibration of 2D tests (Ragni et al. 2018). Considering these HDR tests, when carefully observing Figure 2-4, the LRB and NRB exhibit roughly the same amount of stress at the positive and negative directions suggesting anisotropic behavior, similar behavior as observed in HDR bearing (Figure 2-6).

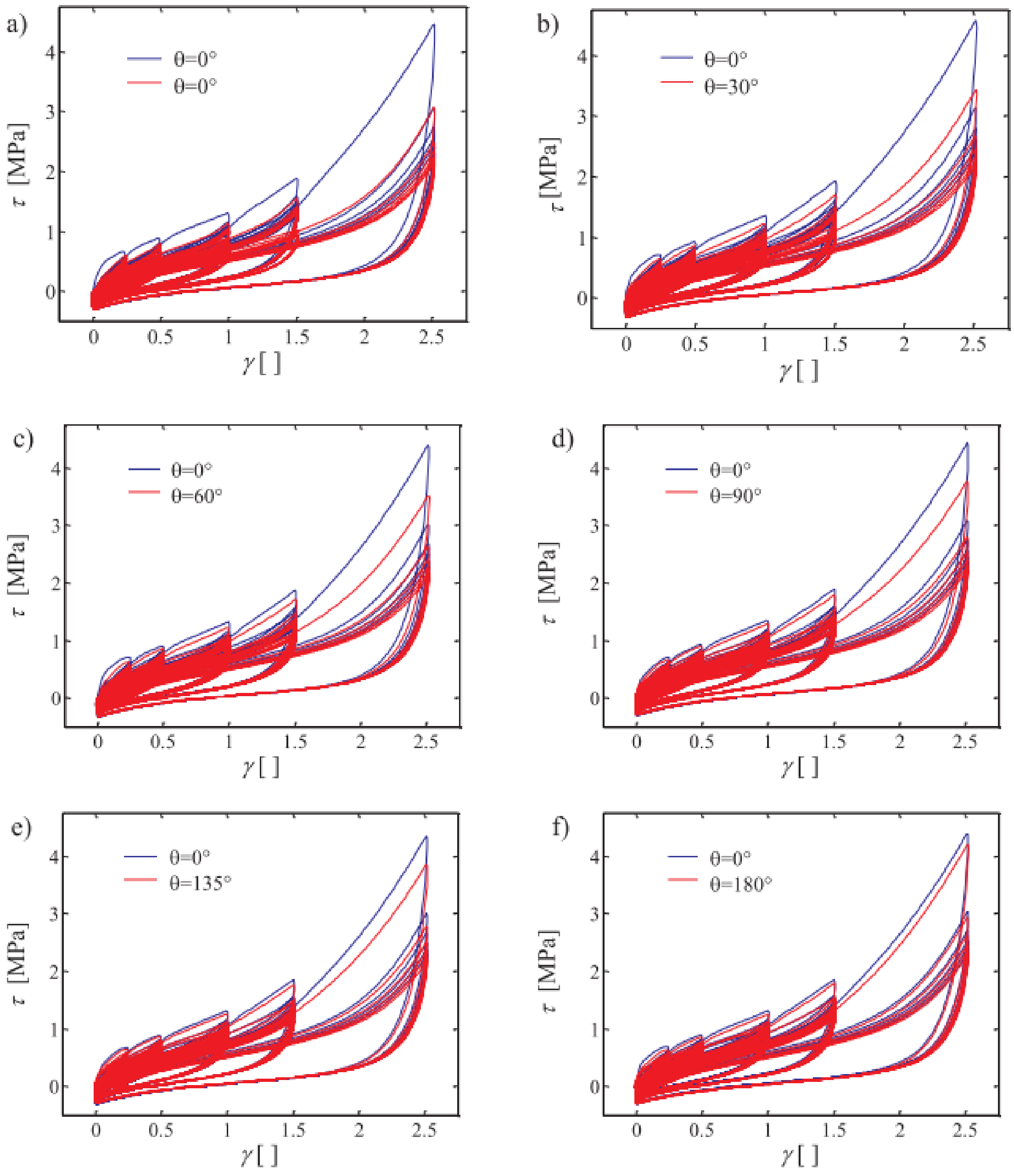

Figure 2-6 Double shear tests on rotated test pieces: (a) $\theta = 0°$ (b) $\theta = 30°$ (c) $\theta = 60°$ (d) $\theta = 90°$ (e) $\theta = 135°$ (f) $\theta = 180°$ (Ragni et al. 2018)

2-2 Existing Bearing Models

2-2-1 Linearized viscoelastic model

In design of buildings, computational time is costly and therefore performing a simplified analysis is often desired. In order to defer extraneous analyses, certain requirements have to be met in order to perform an Equivalent Lateral Force (ELF) analysis, sometimes referred as Equivalent Linear Analysis (ELA), Linear Static Analysis, or Equivalent Static Analysis (ASCE 2017; BSSC 1997; CEN 2004). For base isolated buildings, the idea of performing an ELF analysis is based on the observation that the response is dominated by its first mode of vibration, in which the horizontal displacements are concentrated at the isolation level, while the superstructure moves like a rigid body. For that reason, base isolated buildings can then be modeled as an equivalent elastic SDOF system, whose stiffness is taken as the effective stiffness of the isolation system, evaluated for the design displacement. For US design standards (ASCE, 2017) to allow such analysis, the following criteria have to be met:

1.) The Base-isolated structure cannot exceed certain height requirements depending on the lateral force system.
2.) Fixed-base period must be well separated from the isolated period.
3.) The isolation system must have an adequate restoring force.
4.) The isolated structure may be on Site Classes A, B, C, or D without restriction on S_1, with effective isolated periods up to 5s, and with moderate irregularities.

With the requirements met for ELA, the isolation system can be reduced to a SDOF linearized system. When considering a linear damped system, the differential equation is expressed as:

$$M\ddot{x}_{eq}(t) + C_{eq}\dot{x}_{eq}(t) + K_{eq}x_{eq}(t) = -M\ddot{x}_g(t) \qquad (2-1)$$

where M, C_{eq}, and K_{eq} are the mass, equivalent viscous damping, and equivalent stiffness of the system and the overdot denotes differentiation with respect to time. The acceleration, velocity, and displacement of the single degree of freedom (SDOF) system with respect to the ground are expressed as $\ddot{x}_{eq}(t), \dot{x}_{eq}(t)$, and $x_{eq}(t)$, respectively. As shown in Figure 2-7, the hysteretic behavior of the isolation system is simplified and represented by an equivalent linearized system that includes an elastic spring force and viscous damping force. Although, this type of analysis may be desired, it may not capture the actual behavior of isolation system and often the stringent requirements of the code require nonlinear representation of such isolation systems. Models for nonlinear time history analysis are described next.

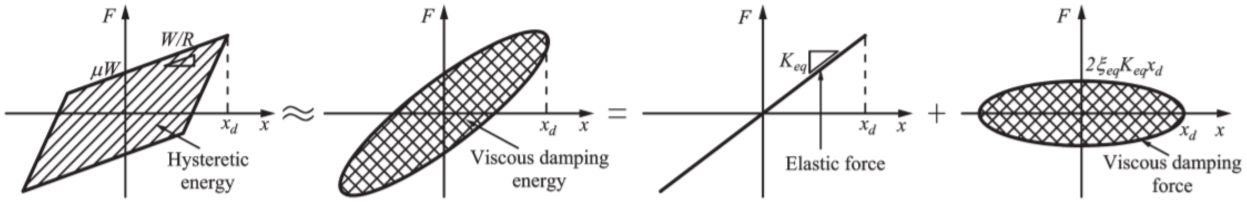

Figure 2-7 Linear analysis method (Liu et al. 2014).

2-2-2 Bouc-Wen Model

One of the most utilized hysteretic models in structural engineering is the Bouc-Wen model (Bouc 1967; Wen 1976). The attraction of this model is the versatility it has in modeling different types of hysteretic systems. The equations of motion along with the Bouc-Wen model restoring force is expressed as:

$$M\ddot{x}(t) + C\dot{x}(t) + F(t) = -M\ddot{x}_g(t) \qquad (2-2)$$

where F(t) is the Bouc-Wen restoring force. The restoring force is given by,

$$F(t) = \alpha K_{initial} x(t) + (1-\alpha) K_{initial} z(t) \qquad (2-3)$$

where α is the ratio of post-yield stiffness to the pre-yield stiffness, $K_{initial}$. The non-observable hysteretic parameter $z(t)$, sometimes referred to as the hysteretic displacement, is a nonlinear differential equation with zero initial condition *z(0)=0*, and has dimensions of length:

$$\dot{z}(t) = \dot{x}(t)\left\{A - \left[\beta sign\big(z(t)\dot{u}(t)\big) + \gamma\right]|z(t)|^{n}\right\} \qquad (2-4)$$

The *sign* denotes signum function, and A, β are always positive values. Parameters γ and n are dimensionless quantities controlling the behaviour of the model (i.e. $n = \infty$ generates an elastoplastic hysteresis), with more details found in Wen (1976). The dimensionless constants $A, \beta,$ and γ must satisfy the following A/($\beta + \gamma$) =1 (Mokha et al. 1993). Typically for elastomeric bearings, A is set equal to 1 and both β and γ are set to 0.5. One of the benefits of this model is that it can more accurately capture the transition between the pre-yield and the post-yield stiffness both at its initial state and at reversals (Wong 2014). The robustness of this model allows for the model to be easily adaptable for many applications. The following subsections comprises two models that have been modified for the use of various applications such as lead core heating and rubber hardening.

2-2-2-1 Lead Core Heating Model

In order to include the lead core heating that is observed in LRBs, the Bouc-Wen model was extended to include strength degradation. To accurately implement the strength degradation due to heating of the lead core, the relationship between temperature and shear strength of the lead core were examined by Kalpakidis and Constantinou (2009b). A formulation was proposed to calculate the heating from cyclic loading and the model was later implemented in OpenSees (2014), labeled *LeadRubberX*, capable of capturing the lead-core heating effects using the temperature-lead strength relationship (Kumar et al. 2014). The backbone of this model is the Bouc-Wen formulation, the coupled bi-directional hysteretic model is isotropic and allows degradation of the hysteresis (i.e. the characteristic strength of the lead). The restoring force components F_x and F_y are in terms of displacements U_x and U_y, along orthogonal directions x and y as follows:

$$\begin{Bmatrix} F_x \\ F_y \end{Bmatrix} = c_d \cdot \begin{Bmatrix} \dot{U}_x \\ \dot{U}_y \end{Bmatrix} + K_2 \cdot \begin{Bmatrix} U_x \\ U_y \end{Bmatrix} + (\sigma_{YL}(T_L) A_L) \cdot \begin{Bmatrix} Z_x \\ Z_y \end{Bmatrix} \qquad (2-5)$$

$$Y \cdot \begin{Bmatrix} \dot{Z}_x \\ \dot{Z}_y \end{Bmatrix} = (A \cdot [\boldsymbol{I}] - B \cdot [\Omega]) \cdot \begin{Bmatrix} \dot{U}_x \\ \dot{U}_y \end{Bmatrix} \qquad (2-6)$$

$$[\Omega] = \begin{Bmatrix} Z_x^2 \cdot [sgn(\dot{U}_x Z_x) + 1] & Z_x Z_y \cdot [sgn(\dot{U}_y Z_y) + 1] \\ Z_x Z_y \cdot [sgn(\dot{U}_x Z_x) + 1] & Z_y^2 \cdot [sgn(\dot{U}_y Z_y) + 1] \end{Bmatrix} \qquad (2-7)$$

In Equations 2-5 through 2-7, $[\boldsymbol{I}]$ is the identity matrix and dimensionless parameters Z_x and Z_y, are bounded by the values of ±1. In this formulation, the Bouc-Wen model from Equation 2-3 is extended to capture the biaxial interaction of hysteretic systems (Park et al. 1986). The Bouc-Wen model is further simplified from Equation 2-3, by imposing B=β=γ=0.5. The quantities A and B should be related with the following expression (A=2B) in order for the equations to properly function, therefore A=1 is imposed. These equations produce a typical hysteretic response of a smooth bilinear Bouc-Wen model with the addition of yield strength degradation of the lead core is included and expressed as a function of the temperature of the lead core, $\sigma_{YL}(T_L)$. The temperature of the lead increases as the bearing is being cycled (Kalpakidis and Constantinou 2009b), and consequently, the strength of lead core decreases. The thermodynamic relationship of strength degradation and cyclic displacement were derived using experimental temperature-tensile strength relationship. Various assumptions were deduced such as the interface temperature increases at half the increase of the bulk of the lead core and that perfect contact exist between the lead core and steel plates along with others (Kalpakidis and Constatinou 2008). The formulation for strength degradation, $\sigma_{YL}(T_L)$, using the assumptions described and solution type 2, which considers the heat conduction through steel plates (more accurate) are as follows:

$$\dot{T}_L = \frac{\sigma_{YL}(T_L)\cdot\sqrt{Z_x^2+Z_y^2}\cdot\sqrt{\dot{U}_x^2+\dot{U}_y^2}}{\rho_L c_L h_L} - \frac{k_S\cdot T_L}{r\cdot\rho_L\cdot c_L\cdot h_L}\cdot\left(\frac{1}{F}+1.274\cdot\left(\frac{t_s}{a}\right)\cdot(\tau)^{-\frac{1}{3}}\right) \qquad (2-8)$$

$$F = \left\{\begin{array}{c} 2\cdot\left(\frac{\tau}{\pi}\right)^{\frac{1}{2}}-\frac{1}{2}\cdot\left[2-\left(\frac{\tau}{4}\right)-\left(\frac{\tau}{4}\right)^2-\frac{15}{4}\cdot\left(\frac{\tau}{4}\right)^3\right],\ \tau<0.6 \\ \frac{8}{3\pi}-\frac{1}{2(\pi\cdot\tau)^{\frac{1}{2}}}\cdot\left[1-\frac{1}{3\cdot(4\tau)}+\frac{1}{6\cdot(4\tau)^2}-\frac{1}{12\cdot(4\tau)^3}\right],\tau\geq 0.6 \end{array}\right\} \qquad (2-9)$$

$$\tau = \frac{\alpha_S t}{r^2} \qquad (2-10)$$

$$\sigma_{YL}(T_L) = \sigma_{YL0}\cdot\exp(-E_2 T_L) \qquad (2-11)$$

Eqs. (2-8) to (2-11) shown above, are used to find the current shear yield stress of the lead core by solving for the temperature of the lead, T_L. The geometric parameters found in Equation 2-8 are represented as the following: h_L is the height of the lead core, r is the radius of the lead core, and t_s is the total shim plate thickness. The material properties in Equation 2-8 are the following: ρ_L is the density of lead, c_L is the specific heat of lead, α_s is the thermal diffusivity of steel, k_s is the thermal conductivity of steel, and σ_{YL0} is the effective yield stress of lead at the reference (starting) temperature. The dimensionless quantity, τ, is dimensionless time and t, is the time since the beginning of the motion. Note that Equation 2-11 describes the dependency of the lead core strength on its increase in temperature. The value of the lead core strength $\sigma_{YL}(T_L)$, given the temperature, is related by the parameter E_2 which describes the rate of the degradation. The material parameter values chosen for typical LRBs are the following: ρ_L=11,200 kg/m^3, c_L = 130 J/(kg◦C), k_L =50W/(m◦C), α_S= 1.41×10−5 m^2/s, and E_2 =0.0069/◦C. Figure 2-8 shows the typical hysteresis of the Bouc-Wen model including strength degradation when considering Equations 2-8 and 2-11.

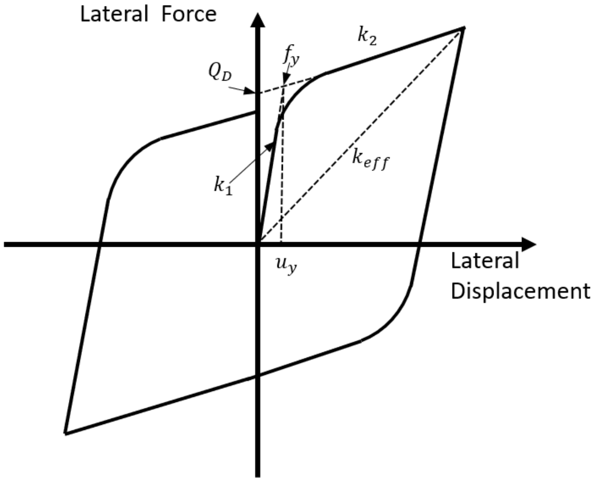

Figure 2-8 Hysteresis for Bouc-Wen model including strength degradation.

The initial stiffness k_1, post-yield stiffness k_2, and the characteristic strength Q_d are the primary parameters of an LRB model. Note, the characteristic strength degrades as it returns to zero lateral displacement. The hysteresis for the modified Bouc-Wen model is smooth in transition from pre-yield to post-yield stiffness. The characteristic strength is calculated by multiplying the yield shear stress by the cross-sectional area of the lead.

2-2-2-2 Bouc-Wen with Prager's Rule

In order to capture hardening effects that may occur in various hysteretic systems, the Bouc-Wen model was further modified to include Prager's rule (Bouc 1967; Casciati 1989). The model was later implemented in OpenSees by Schellenberg et al. (2015) as shown in Figure 2-9, with hardening at larger strains.

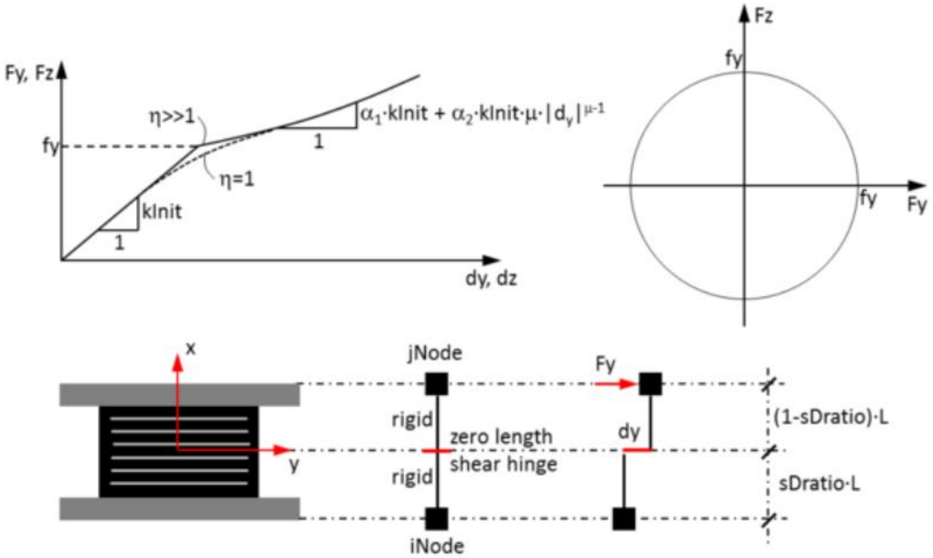

Figure 2-9 Bouc-Wen Hardening Element (Schellenberg et al. 2015)

Prager's rule was introduced into the Bouc-Wen model by Casciati (1989) being solely phenomenological. Alongside the hardening capability captured in the model, the hysteresis loops allow for rounded corners which resemble the physical behavior of elastomeric bearings as described by Casciati (1989). Casciati advanced the classical plasticity theory for bearing behavior by connecting the discontinuity between the elastic and plastic phases. The formulation is as follows:

$$\begin{Bmatrix} F_x \\ F_y \end{Bmatrix} = K_2 \cdot \begin{Bmatrix} U_x \\ U_y \end{Bmatrix} + (Q_D) \cdot \begin{Bmatrix} Z_x \\ Z_y \end{Bmatrix} + K_3 \cdot \mathrm{sgn} \begin{Bmatrix} U_x \\ U_y \end{Bmatrix} \cdot \begin{vmatrix} U_x^{\mu} \\ U_y^{\mu} \end{vmatrix} \qquad (2-12)$$

$$K_3 = \alpha_2 \cdot K_{initial} \qquad (2-13)$$

where the first two terms in the restoring force formulation consists of the post-yield stiffness, K_2, and the constant characteristic strength, Q_D, resembling that of a typical Bouc-Wen model. The model deviates with the last term of the equation, in which the hardening term is aggregated. The parameter, α_2, is the post-yield stiffness ratio of non-linear hardening component and K_3 is the post-yield nonlinear stiffness. The restoring force formulation reaffirms that the model can be highly nonlinear depending on the value of μ. The hardening effects can be observed in Figure 2-9, as the displacement increases the stiffness increases. For instance, if the value of μ is set high, then the hardening can occur prematurely, conversely, if the value is set low then the hardening will occur at higher strains. One of the setbacks for this model is that the stiffness is dependent on each orthogonal direction therefore making this system uncoupled.

2-2-3 Huang model

The model implemented by Huang et al. (2000) is based on the rate independent plasticity theory (Lubliner and Moran 1992). The model can capture the behavior of elastomeric bearings utilizing a yield function formulation consisting of the back force $\boldsymbol{\alpha_y}$**,** and a radius Q_D as follows:

$$\mathrm{f_y} = \left\|\boldsymbol{F} - \boldsymbol{\alpha_y}\right\| - Q_D \qquad (2-14)$$

where,

$$\boldsymbol{F} = K_1 \cdot \boldsymbol{U^e} = K_1(\boldsymbol{U} - \boldsymbol{U^p}) \qquad (2-15)$$

and the restoring force, $\boldsymbol{F} = \left[F_x \;\; F_y\right]^T$, in a bearing is assumed to depend only on the shear deformation, $\boldsymbol{U} = \left[\,U_x \;\; U_y\right]^T = \boldsymbol{U^e} + \boldsymbol{U^p}$, in orthogonal horizontal directions, decomposed into elastic and plastic parts. In this formulation it can be considered linearly isotropic, with the force related to the displacement by a constant stiffness parameter, K_1. An associative flow has shown to describe LRBs and HDR bearings at low to intermediate strains (Huang 2002). The implication of associative flow is that the evolution of the plastic displacement vector is always normal to the yield surface in force space, giving the following:

$$\dot{\boldsymbol{U}}^p = \dot{\gamma}\frac{\partial f_y(\boldsymbol{F}, \boldsymbol{\alpha}_y)}{\partial \boldsymbol{F}} = \dot{\gamma}\boldsymbol{n} \qquad (2-16)$$

Where $\dot{\gamma}$ is the consistency parameter and $\boldsymbol{n}$ is defined as follows:

$$\boldsymbol{n} = \frac{\partial f_y(\boldsymbol{F}, \boldsymbol{\alpha}_y)}{\partial \boldsymbol{F}} = \frac{\boldsymbol{F} - \boldsymbol{\alpha}_y}{\left\| \boldsymbol{F} - \boldsymbol{\alpha}_y \right\|} \qquad (2-17)$$

The consistency parameter, $\dot{\gamma}$, must satisfy the Kuhn-Tucker conditions (Lubliner and Moran 1992) as follows:

$$f_y \leq 0, \qquad \dot{\gamma} f_y = 0\,, \qquad \dot{\gamma} \geq 0 \qquad (2-18)$$

The Kuhn-Tucker conditions in Equations (2-18) establishes the following two requirements: Elastic force states to lie on or inside the yield surface ($\dot{\gamma} = 0$), for plastic force it states ($\dot{\gamma} > 0$) to lie on the yield surface. Finally, the consistency condition must be satisfied, given by:

$$\dot{\gamma} \dot{f}_y = 0 \qquad (2-19)$$

This forbids the force point from abandoning the yield surface during plastic flow. Lastly, a linear kinematic hardening rule is specified as:

$$\dot{\boldsymbol{\alpha}}_{\boldsymbol{y}} = K_2 \dot{\boldsymbol{U}}^p = K_2 \dot{\gamma} \boldsymbol{n} \qquad (2-20)$$

where K_2 is a constant hardening modulus. When considering 1-D, the pre-yield stiffness is simply K_1, and the post-elastic stiffness is αK_1, the hardening modulus is given by:

$$K_2 = K_1 \frac{\alpha}{1 - \alpha} \qquad (2-21)$$

Where α is the ratio of post-yield stiffness to the pre-yield stiffness.

2-2-4 HDR Element

The HDR element consists of an elastic component and a hysteretic component (Grant et al. 2004). The elastic component uses the Mooney-Rivlin strain energy function, with five elasticity constants. The elastic component is denoted by $\boldsymbol{F_1}$, as shown in Eq. 2-22, and is a function of the displacement and the damage evolution parameters D_s and D_M which account for scragging and Mullins' damage effects, respectively.

The hysteretic component, represented by $\boldsymbol{F_2}$ in Eq. 2-22, uses an approach that is similar to bounding surface plasticity (Dafalias and Popov 1975). The formulation may be defined in terms of the magnitude of the displacement vector. The hysteretic force evolves towards the direction of the velocity vector, such that, even under a sudden change in loading direction, the change in $\boldsymbol{F_2}$ is smooth. Unlike Huang's formulation, it provides a continuous response under load reversals without restrictions to harmonic loading (Huang 2002). In the restoring force equations below, the latter part of the equation is not only a function of the magnitude of the displacement but also the normalized velocity vector $\mathbf{n}$, with addition to scragging damage effects, denoted by D_s.

$$\boldsymbol{F}(\boldsymbol{U},\boldsymbol{n},D_s,D_M)=\boldsymbol{F_1}(\boldsymbol{U},D_s,D_M)+\boldsymbol{F_2}(\boldsymbol{U},\boldsymbol{n},D_s) \qquad (2-22)$$

This phenomenological model consists of 10 parameters, three of which account for the hyper-elastic component (a_1-a_3), three for the hysteretic component (b_1-b_3), and four for the damage parameters (c_1-c_4) for scragging and Mullins effects.

2-2-4-1 Elastic Component

Isotropic strain energy functions are typically utilized for constitutive models of elastomers, considering a hyperelastic stress-strain relationship. The generalization of the

Mooney-Rivlin strain energy function is considered, with five elasticity constants where a similar function can be found in Haupt and Sedlan (2001):

$$\Psi(\boldsymbol{C}) = c_1(\mathrm{I}-3) + c_2(\mathrm{II}-3) + c_3(\mathrm{I}-3)(\mathrm{II}-3) + c_4(\mathrm{II}-3)^2 + c_5(\mathrm{I}-3)^3 \qquad (2-23)$$

where c_1 to c_5 are material parameters. The right Cauchy-Green strain tensor is denoted by, $\boldsymbol{C}$. The first two invariants of the right Cauchy-Green strain tensor I and II are as follows:

$$\mathrm{I} = tr\,\boldsymbol{C} \qquad \mathrm{II} = \frac{1}{2}[(tr\,\boldsymbol{C})^2 - tr(\boldsymbol{C})^2] \qquad (2-24)$$

Simple shearing of the entire bearing may be represented by a single state of stress and plain strain. The deformation gradient, **F**, and right Cauchy-Green tensor for this deformation are given by:

$$\mathbf{F} = \begin{bmatrix} 1 & \gamma & 0 \\ 0 & 1 & 0 \\ 0 & 0 & 1 \end{bmatrix} \qquad \boldsymbol{C} = \boldsymbol{F}^{\boldsymbol{T}}\boldsymbol{F} = \begin{bmatrix} 1 & \gamma & 0 \\ \gamma & 1+\gamma^2 & 0 \\ 0 & 0 & 1 \end{bmatrix} \qquad (2-25)$$

where γ represents the shear strain. It is important to note that this assumption is equivalent to representing the entire bearing by a single Gauss integration point and does not consider localized effects caused by bearing boundary conditions. The first two invariants both simplify to:

$$\mathrm{I} = \mathrm{II} = \gamma^{\mathbf{2}} + 3 \qquad (2-26)$$

In design practice, the Cauchy stresses are of engineering significance. They are obtained from the second Piola-Kirchoff stress tensor by transforming to the ‘spatial description’ of solid mechanics, through the following relationship:

$$\boldsymbol{\sigma} = J^{-1}\boldsymbol{F}\boldsymbol{S}\boldsymbol{F}^{T} \qquad (2-27)$$

where J =1 is the Jacobian of the transformation. The second Piola-Kirchoff stress tensor, $\boldsymbol{S}$, is derived as described in (Bonet and Wood 2008). The form for the Cauchy stress tensor is obtained after some calculations:

$$\boldsymbol{\sigma} = \begin{bmatrix} E(\gamma^6) & O(\gamma^5) & 0 \\ O(\gamma^5) & E'(\gamma^4) & 0 \\ 0 & 0 & E'(\gamma^4) \end{bmatrix} \qquad (2-28)$$

where the terms $O(\gamma^n)$ and $E(\gamma^n)$ are odd and even polynomials of the nth order of the shear strain, γ, and the apostrophes signify that the functions are different for each component, though the matrix is symmetric. The coefficients of each polynomial are given by factors of the material parameters c_1 to c_5. The shear component of Equation 2-28 is shown below:

$$\sigma_{12} = O(\gamma^5) = (2c_1 + 8c_2)\gamma + (4c_2 + 2c_3)\gamma^3 + (12c_3 + 8c_4 + 22c_5)\gamma^5 \qquad (2-29)$$

It is important to note that the shear stress is symmetrical $\sigma_{12} = \sigma_{21}$, and that the shear stress components are of importance in bearing models. A potential simplified two parameter model is the Gent model (Gent 1996), performing similar steps as in the formulation of for the Mooney-Rivlin function, the shear component of Equation 2-28 simplifies as follows:

$$\sigma_{12} = \frac{\mu J_m \gamma}{J_m - \gamma^2} \qquad (2-30)$$

where μ is the shear modulus and $J_m = I_m - 3$ where I_m is the limiting value. The model can exhibit the severe strain hardening effects in the stress response. However, it tends to deviate at moderate levels of shear strain. Therefore, the Mooney-Rivlin is considered, with simplification of the equation, the model reduces to a fifth order equation with three constants a_1, a_2, and a_3 as shown below:

$$\boldsymbol{F_1} = K_{S1} K_M [a_1 + a_2 \|\boldsymbol{U}\|^2 + \ a_3 \|\boldsymbol{U}\|^4] \boldsymbol{U} \qquad (2-31)$$

where, $\|\boldsymbol{U}\|$ denotes the displacement magnitude and K_{S1} and K_M are the scragging and Mullins damage parameters commencing at one and decaying to a fraction of one. These damage parameters will be later detailed in a subsequent section 2-2-4-3.

2-2-4-2 Hysteretic Component

The second term in Equation 2-32, the hysteretic component, is based on Dafalias and Popov (1975), where $\boldsymbol{F_2}$, represents the hysteretic force of the bearing. The bounding surface in force space, with radius R(||U||), is defined as follows:

$$B(\boldsymbol{U}) = \|\boldsymbol{F_2}\| - R(\|\boldsymbol{U}\|) \qquad (2-32)$$

The radius R is isotropic, rate independent, and utilizes a quadratic relationship between the radial force and the current magnitude of the displacement as defined below and shown in Figure 2-10.

$$R = b_1 + K_{S2} b_2 \|\boldsymbol{U}\|^2 \qquad (2-33)$$

where b_1 and b_2 are material parameters, and K_{S2} is a reduction factor due to scragging effects (described in section 2-2-4-3).

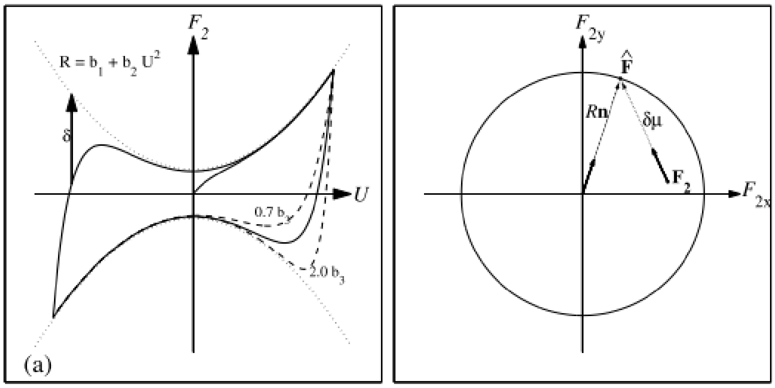

Figure 2-10 Evolution of hysteretic force, (a) Unidirectional and (b) bidirectional evolution of hysteretic component of force (Grant et al. 2004).

As shown in Figure 2-10, a scalar distance variable, δ, captures the distance of the force vector relative to the bounding surface. The unit direction vector, $\boldsymbol{\mu}$, defines along which direction the distance is measured. Both terms are derived from the “image force”, $\widehat{\boldsymbol{F}}$, which performs a role analogous to the “image stress” in bounding surface plasticity (Dafalias and Popov 1975). The image force is projected from the origin onto the bounding surface as follows:

$$\widehat{\boldsymbol{F}} = R\boldsymbol{n} \qquad (2-34)$$

where the $\boldsymbol{n}$ is the velocity unit vector. The parameter δ can be interpreted as the magnitude of the vector pointing from the current force point to the image force and the parameter $\boldsymbol{\mu}$ as the unit direction as follows:

$$\delta = \left\|\widehat{\boldsymbol{F}} - \boldsymbol{F_2}\right\| \quad and \quad \boldsymbol{\mu} = \frac{\widehat{\boldsymbol{F}} - \boldsymbol{F_2}}{\left\|\widehat{\boldsymbol{F}} - \boldsymbol{F_2}\right\|} \qquad (2-35)$$

The magnitude of the change is given implicitly in terms of a scalar evolutionary equation for δ:

$$\dot{\delta} = -b_3\delta\left\|\dot{\boldsymbol{U}}\right\| \qquad (2-36)$$

the equation above defines the smooth transition, with a rate dictated by the material parameter, b_3. The appearance of the rate form in Equation 2-36 can be misleading insinuating rate dependence; however it is important to note that the time derivatives appear on both sides of the equation resulting in a rate-independent model. Furthermore, it is important to note that a sudden change of load direction changes the direction and magnitude of the vector $\delta\boldsymbol{\mu}$, according to Equation 2-36. However, this formulation does not experience the “overshooting” phenomenon of conventional bounding surface plasticity. In order to further elucidate the parameter δ, the equations are integrated using backward euler method producing the following equations:

$$n = \frac{\boldsymbol{U} - \boldsymbol{U_n}}{||\boldsymbol{U} - \boldsymbol{U_n}||} \qquad (2-37)$$

$$\delta = \frac{\delta_n}{1 + b_3||\boldsymbol{U} - \boldsymbol{U}_n||} \qquad (2-38)$$

Considering $\boldsymbol{U}$ and $\boldsymbol{U_n}$ represent the current time step and previous time step, respectively. Note, that Equation 2-38 allows for the smooth transition, dictated by the material parameter b_3, regardless of any abrupt changes in the displacement path.

2-2-4-3 Damage parameters for HDR model

Scragging and Mullins effect are included in both the hyperelastic and hysteretic formulation of the HDR model. The equations to account for the damage effects are formulated as exponential degradation equations as follows:

$$K_{S1} = \exp\left(-c_1 D_S^3\right) \qquad (2-39)$$

$$K_{S2} = \exp\left(-c_2 D_S^3\right) \qquad (2-40)$$

$$K_M = c_3 + (1 - c_3)\exp\left(-c_4 D_M^3\right) \qquad (2-41)$$

The parameters c_1 through c_4 are input parameters that are calibrated with experimental data. K_{S1} and K_M are damage factors that affect the hyperelastic component of the HDR model, whereas K_{S2} effects the plasticity portion, more specifically, the hardening in the bounding surface as shown in Equation 2-33. Parameters c_1 and c_2, are the damage parameters that account for degradation due to scragging effects and parameters c_3 and c_4 account for degradation due to Mullins effect. The c_4 parameter represents the rate of damage, while the c_3 parameter varies from zero to one dictating the limit of damage. The evolution of the damage parameters can be seen in Figure 2-11, where D_S is the scragging damage parameter and D_M is the damage parameter for Mullins' effect. The scragging damage parameter, D_S, represents the 'permanent' damage induced in the bearing. The evolution parameter $D_{S,0}^{+}$, acts as a placeholding damage from any previous maximum damage. If $\|\boldsymbol{U}\|$ extends past the previous maximum displacement, $D_{S,0}^{+}$, then the D_S^{-} accumulates as a placeholder of the amount of damage, as shown in Figure 2-11 (between t_1 and t_2). Once the displacement norm reduces below the threshold of the D_S^- parameter (between t_3 and t_4), then the scragging damage, D_S, increases. For a damage amount of D_S, the formulations (Equations 2-39 and 2-40) would undergo exponential decay for both $\boldsymbol{F_1}$ and $\boldsymbol{F_2}$ at a rate dependent on the material parameters c_1 and c_2. The evolution of the scragging parameter, D_S, is summarized as follows:

$$\begin{cases} if\ \|\boldsymbol{U}\| = D_S^+\ and\ \dot{\overline{\|\boldsymbol{U}\|}} > 0 \\ \qquad \dot{D}_S^+ = \dot{D}_S^- = \dot{\overline{\|\boldsymbol{U}\|}} \\ \qquad \dot{D}_S = 0 \\ if\ \|\boldsymbol{U}\| = D_S^-\ and\ \dot{\overline{\|\boldsymbol{U}\|}} > 0 \\ \qquad \dot{D}_S^+ = 0 \\ \qquad \dot{D}_S^- = \dot{\overline{\|\boldsymbol{U}\|}} \\ \qquad \dot{D}_S = -\dot{\overline{\|\boldsymbol{U}\|}} \end{cases} \qquad (2-42)$$

As for Mullins effect, unlike scragging, the degradation occurs over successive cycles of loading, regardless of previous peak magnitude displacements $\|\boldsymbol{U}\|$. Mullins' effect accumulates damage as the displacement norm experiences reversals. The rate of increase of D_M is given by the rate of decrease of the displacement norm, $\|\boldsymbol{U}\|$. The initial Mullins damage parameter evolution parameter, $D_{M,0}$, provides an initial short-term damage that may have previously existed. The damage evolution equations are summarized below and the evolution of D_M from a general displacement history is shown in Figure 2-11(b). Unlike scragging parameter D_S, Mullins' effect parameter D_M increases whenever the magnitude displacement is decreasing (t_2 to t_4 and t_5 to t_7), and does not consider any thresholds.

$$\begin{cases} if \qquad \dot{\overline{\|\boldsymbol{U}\|}} > 0 \\ \qquad \dot{D}_M = 0 \\ if \qquad \dot{\overline{\|\boldsymbol{U}\|}} < 0 \\ \qquad \dot{D}_M = -\dot{\overline{\|\boldsymbol{U}\|}} \end{cases} \qquad (2-43)$$

The Mullins effect formulation (Equation 2-43) limits the amount of damage and tends to become insignificant after several cycles. Note, Mullins effect only affects the hyperelastic component, $\boldsymbol{F_1}$.

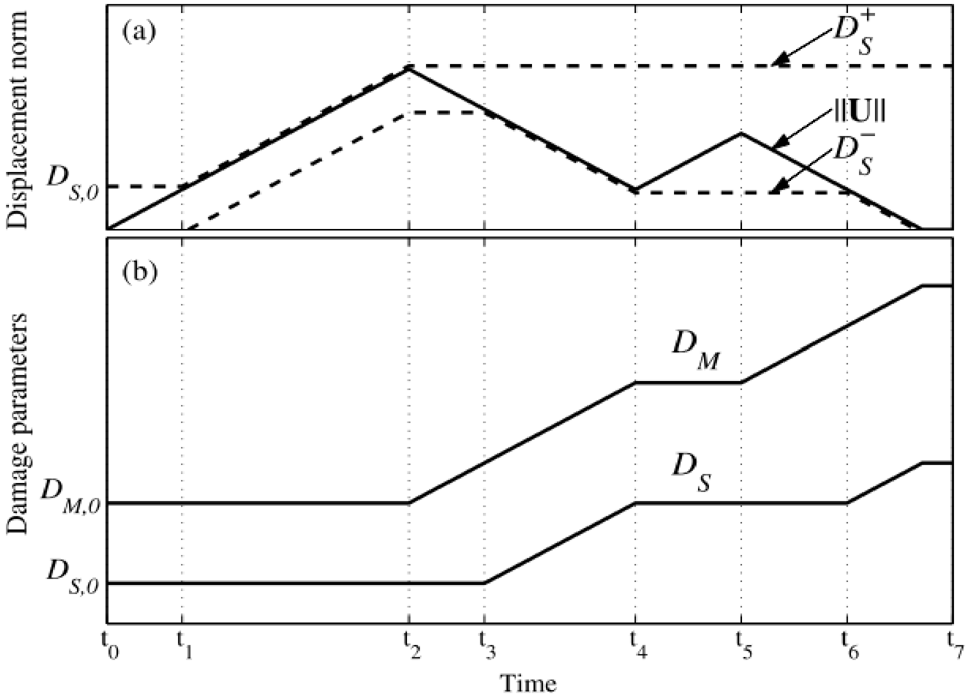

Figure 2-11 (a) Arbitrary history of displacement norm, $\|\boldsymbol{U}\|$, and scragging parameter upper and lower thresholds, D_S^- and D_S^+ and (b)evolution of scragging and Mullins' effect damage parameters, D_S and D_M (Grant et al. 2004)

2-2-5 Anisotropic model

Ragni et al. (2018) used a similar hyperelastic model but modified the formulation by extending the formulation proposed in Tubaldi et al. (2017). The modification was made due to experimentally finding that high damping rubber inherently experiences damage in an anisotropic manner. By experimentally demonstrating that the stress softening, or damage, only occurs if the rubber specimen is displaced in the same direction; proving that if the bearing is displaced in an increasing angle of its original displacement the bearing would begin to develop similar stresses as in the original displacement. The following formulations were utilized in order to model such anisotropic behavior:

$$\sigma_{me} = \alpha_e(1 - q_e^{+})\sigma_e \quad \text{for } \epsilon^{\theta} > 0 \qquad (2-44)$$

$$\sigma_{me} = \alpha_e(1 - q_e^{-})\sigma_e \quad \text{for } \epsilon^{\theta} < 0 \qquad (2-455)$$

where σ_e is the hyperelastic model from Equation 2-31 and α_e is the initial damage parameter. The q_e^{+} and q_e^{-} are damage evolution parameters for the positive and negative directions (opposite directions). For example, the evolution laws of the elastic damage parameters for $\epsilon^{\theta} > 0$ are posed in the following form:

$$\dot{q}_e^{-} = 0 \qquad (2-46)$$

$$\dot{q}_e^{+} = \zeta_e \left| \dot{\epsilon}^{\theta} \right| \left(\left(\frac{\epsilon^{\theta}}{\gamma_{mod}} \right)^{\beta} - q_e^{+} \right) \; if \; q_e^{+} < \left(\frac{\epsilon^{\theta}}{\gamma_{mod}} \right)^{\beta} \qquad (2-47)$$

$$\dot{q}_e^{+} = 0 \; if \; q_e^{+} \geq \left(\frac{\epsilon^{\theta}}{\gamma_{mod}} \right)^{\beta} \qquad (2-48)$$

where ϵ^{θ} is the one-dimensional (1D) displacement along a representative direction (Equation 2-49). For $\epsilon^{\theta}<0$, similar evolution laws are used except roles for $\dot{q}_e^{+}$ and $\dot{q}_e^{-}$ are interchanged in Equations 2-46 to 2-48, and ϵ^{θ} is replaced with $\left|\epsilon^{\theta}\right|$. During a cyclic strain history, both the damage parameters q_e^{+} and q_e^{-} tend to the same limit value, depending on the amplitude of the strain cycle, and the velocity of the damage evolution which is controlled by the parameter ζ_e. The maximum value that can be reached by q_e^{+} and q_e^{-} for strain amplitudes not exceeding $\left|\epsilon^{\theta}\right|$ is given by the expression $\left(\epsilon^{\theta}/\gamma_{mod}\right)^{\beta}$, where γ_{mod} is the maximum amplitude for which the model is deemed valid. Equation 2-47 ensures that damage is not decreased and that they do not increase further once the limit is reached by the current strain. The material parameters $(\alpha_e, \zeta_e, \gamma_{mod}, \beta)$ are calibrated by utilizing experimental data. This model was further extended to include the idea of representative directions (Lubliner and Moran 1992) which allows the use of a one dimensional material law with damage parameters to simulate more complex 2D or 3D material behaviors. Ragni et al. (2018) implemented the idea of representative directions in order to extend the anisotropic model for bidirectional experimental data of HDR specimens. The homogenization technique, considering in reference to 2D shear, is based on the selection of uniformly distributed directions in the plane. Then the 2D shear strain state, γ, are projected onto the unit vector representative direction via $\boldsymbol{n}^{\theta}$. The unit vector $\boldsymbol{n}^{\theta}$ represents the direction corresponding to the angle θ, the projection along that direction identifies the one-dimensional strain:

$$\boldsymbol{\epsilon}^{\theta} = \gamma \cdot \boldsymbol{n}^{\theta} \qquad (2-49)$$

For each direction, a 1D constitutive law relates the one-dimensional deformation measure ϵ^{θ} with the associated stress σ^{θ}, oriented as $\boldsymbol{n}^{\theta}$. The set of internal variables is required to describe the damage dissipative phenomena. These variables can be collected in the vector $\boldsymbol{v}^{\theta}$as their values may differ from direction to direction. The response in the individual directions is known with evolution laws and internal variables are expressed as:

$$\dot{\boldsymbol{v}}^{\theta} = g\left(\epsilon^{\theta}, \dot{\epsilon}^{\theta}; \boldsymbol{v}^{\theta}\right) \qquad (2-50)$$

And the corresponding stress is a derived quantity can be expressed as:

$$\sigma^{\theta} = f(\epsilon^{\theta}, \dot{\epsilon}^{\theta}; \boldsymbol{v}^{\theta}) \qquad (2-51)$$

If the selected directions are homogenously and continuously distributed, the global 2D shear stress τ_m due to Mullins effect can be attained from the following integral,

$$\tau_m(\gamma, \dot{\gamma}; \boldsymbol{v}) = \frac{1}{\pi}\int_0^{\pi} f(\epsilon^{\theta}, \dot{\epsilon}^{\theta}, \boldsymbol{v}^{\theta})\boldsymbol{n}^{\theta} d\theta \qquad (2-52)$$

where $\boldsymbol{v}$ contains the state variables for the specified directions. It is important to note the summation is extended to only π rather than 2π due to the fact that the generic angle θ represents fibers along both the positive and negative directions. For numeric applications, finite amount of fibers will be utilized thus Equation 2-51 can be approximated to a sum over all discrete directions and the state vector function reduces to a finite number of internal variables. Implementation of representative directions utilize the evolution laws from Equations 2-45 to 2-49 with the extension to each individual homogenous fiber.

2-3 Conclusions

In this section various plasticity, elastic, and damage models were reviewed to demonstrate the current state of practice for modeling elastomeric bearings. The complex behavior of the bearing materials of LRBs, the lead core and rubber, are verified through experimental data. Of particular interest for LRBs, the lead core nonlinear behaviors range from lead core heating to initial lead core hardening. The nonlinear behaviors in the rubber ranged from hardening, scragging/Mullins' damage effects, pronounced softening 'unloading' effects, and anisotropic behaviors. While the models presented aimed at capturing one or more of these behaviors, a model that captures all these behaviors was not found. In the following chapter, a parallel model will be introduced, demonstrating its capabilities in capturing the behaviors of interest as observed in LRB experiments undergoing large strains.

2-4 References

An, G., Kim, M., Jung, J.-W., Mosqueda, G., and Marquez, J. F. (2020). “Evaluation of Clearance to Stop Requirements in A Seismically Isolated Nuclear Power Plant.” *Energies*, 13(22), 6156.

Aramaki, S., Uno, K., and Noyori, K. (2004). “Study of Lead Pillar Damper for the Earthquake Resistance Reinforcement of an Established Road Bridge.” *Proc. of the 13th World Conference on Earthquake Engineering. Paper No. 364, Mira Digital Publishing,St. Louis, MO.*, Vancouver, B.C., Canada.

ASCE. (2017). *Minimum Design Loads and Associated Criteria for Buildings and Other Structures*. ASCE/SEI Standard 7, Reston, VA.

Bonet, J., and Wood, R. D. (2008). *Nonlinear continuum mechanics for finite element analysis, 2nd edition*. *Nonlinear Continuum Mechanics for Finite Element Analysis, 2nd Edition*.

Bouc, R. (1967). “Forced Vibration of Mechanical Systems with Hysteresis.” *Proc. of the Fourth Conference on Nonlinear Oscillations, Prague, Czech Republic: Academia*.

Building Seismic Safety Council. (1997). *NEHRP guidelines for the seismic rehabilitation of buildings, FEMA-273*. *Federal Emergency Management Agency*, Federal Emergency Management Agency: Washington D.C.

Casciati, F. (1989). “Stochastic dynamics of hysteretic media.” *Structural Safety*, 6(2–4), 259–269.

Comite´Europe´en de Normalisation (CEN). (2004). *Eurocode 8, Design of Structures forEarthquake Resistance-Part 1: General Rules, Seismic Actions and Rules for Buildings*. Brussels, Belgium.

Dafalias, Y. F., and Popov, E. P. (1975). “A model of nonlinearly hardening materials for complex loading.” *Acta Mechanica*, 21(3), 173–192.

Diani, J., Fayolle, B., and Gilormini, P. (2009). “A review on the Mullins effect.” *European Polymer Journal*, Elsevier Ltd, 45(3), 601–612.

Eem, S., and Hahm, D. (2019). “Large strain nonlinear model of lead rubber bearings for beyond design basis earthquakes.” *Nuclear Engineering and Technology*, 51(2), 600–606.

Freund, M., and Ihlemann, J. (2010). “Generalization of one-dimensional material models for the finite element method.” *ZAMM Zeitschrift fur Angewandte Mathematik und Mechanik*.

Gent, A. N. (1996). “A New Constitutive Relation for Rubber.” *Rubber Chemistry and Technology,* Allen Press, 69(1), 59–61.

Grant, D. N., Fenves, G. L., and Whittaker, A. S. (2004). “Bidirectional Modelling of High-Damping Rubber Bearings.” *Journal of Earthquake Engineering*, 8(1), 161–185.

Harwood, J. A. C., Mullins, L., and Payne, A. R. (1965). “Stress softening in natural rubber vulcanizates. Part II. Stress softening effects in pure gum and filler loaded rubbers.” *Journal of Applied Polymer Science*, 9(9), 3011–3021.

Haupt, P., and Sedlan, K. (2001). “Viscoplasticity of elastomeric materials: Experimental facts and constitutive modelling.” *Archive of Applied Mechanics*, 71(2–3), 89–109.

Huang, W.-H. (2002). “Bi-directional testing, modeling, and system response of seismically isolated bridges.” *Civil and Environmental Engineering*, University of California, Berkeley.

Huang, W., Fenves, G. L., Whittaker, A. S., and Mahin, S. A. (2000). “Characterization of Seismic Isolation Bearings for Bridges from Bi-Directional Testing.” *Proceedings 12th World Conference on Earthquake Engineering*, 1–8.

Ishida, K., Shiojiri, H., Iizuka, M., Mizukoshi, K., and Takabayashi, K. (1991). “Failure Tests of Laminated Rubber Bearings.” *Proceedings of the 11th international conference on structural mechanics in reactor technology*, IASMiRT, Tokyo,Japan, 241–246.

Kalpakidis, I., and Constatinou, M. (2008). *Effects of heating and load history on the behavior of lead-rubber bearings. Technical Rep.No. MCEER-08-0027*, Multidisciplinary Center for Earthquake Engineering Research, Buffalo, N.Y.

Kalpakidis, I. V., and Constantinou, M. C. (2009a). “Effects of Heating on the Behavior of Lead-Rubber Bearings. II: Verification of Theory.” *Journal of Structural Engineering*, 135(12), 1450–1461.

Kalpakidis, I. V., and Constantinou, M. C. (2009b). “Effects of Heating on the Behavior of Lead-Rubber Bearings. I: Theory.” *Journal of Structural Engineering*, 135(12), 1440–1449.

Kumar, M., Whittaker, A. S., and Constantinou, M. C. (2014). “An advanced numerical model of elastomeric seismic isolation bearings.” *Earthquake Engineering & Structural Dynamics*, 43(13), 1955–1974.

Liu, T., Zordan, T., Briseghella, B., and Zhang, Q. (2014). “An improved equivalent linear model of seismic isolation system with bilinear behavior.” *Engineering Structures*, 61, 113–126.

Lubliner, J., and Moran, B. (1992). “Plasticity Theory.” *Journal of Applied Mechanics*.

McVitty, W. J., and Constantinou, M. C. (2015). “Property modification factors for seismic isolators: Design guidance for buildings.” *MCEER Report,* 15–0005.

Mokha, A. S., Constantinou, M. C., and Reinhorn, A. M. (1993). “Verification of Friction Model of Teflon Bearings under Triaxial Load.” *Journal of Structural Engineering,* 119(1), 240–261.

Mullins, L. (1969). “Softening of Rubber by Deformation.” *Rubber Chemistry and Technology*, 42(1), 339–362.

OpenSees. (2014). “Open system for earthquake engineering (Version 2.4.4).”

Park, Y. J., Wen, Y. K., and Ang, A. H. (1986). “Random vibration of hysteretic systems under bi-directional ground motions.” *Earthquake Engineering & Structural Dynamics*.

Ragni, L., Tubaldi, E., Dall’Asta, A., Ahmadi, H., and Muhr, A. (2018). “Biaxial shear behaviour of HDNR with Mullins effect and deformation-induced anisotropy.” *Engineering Structures,* 154, 78–92.

Sanchez, J., Masroor, A., Mosqueda, G., and Ryan, K. (2013). “Static and dynamic stability of elastomeric bearings for seismic protection of structures.” *Journal of Structural Engineering (United States),* 139(7), 1149–1159.

Schellenberg, A. H., Sarebanha, A., Schoettler, M. J., Mosqueda, G., Benzoni, G., and Mahin, S. A. (2015). “Hybrid Simulation of Seismic Isolation Systems Applied to an APR-1400 Nuclear Power Plant.” *PEER Reports, Headquaters at the University of California*.

Skinner, R. I., Beck, J. L., and Bycroft, G. N. (1974). “A practical system for isolating structures from earthquake attack.” *Earthquake Engineering & Structural Dynamics*, 3(3), 297–309.

Tubaldi, E., Ragni, L., Dall’Asta, A., Ahmadi, H., and Muhr, A. (2017). “Stress softening behaviour of HDNR bearings: modelling and influence on the seismic response of isolated structures.” *Earthquake Engineering & Structural Dynamics,* 46(12), 2033–2054.

Tyler, R., and Robinson, W. (1984). “High-strain tests on lead-rubber bearings for earthquake loadings.” *Bulletin of the New Zealand Society for Earthquake Engineering*, 17(2), 90–105.

Wen, Y. K. (1976). “Method for Random Vibration of Hysteretic Systems.” *Journal of the Engineering Mechanic Division,* 102(2), 249–263.

Wong, J. B. (2014). “Assessment of the Effect of Different Isolation Systems on Seismic Response of a Nuclear Power Plant.” University of California, Berkeley.

Chapter 3 RESPONSE OF A SEISMICALLY ISOLATED STRUCTURE WITH LEAD RUBBER BEARINGS CONSIDERING HEATING EFFECTS

3-1 Introduction

There are several factors that contribute towards the complex behavior of the Lead rubber bearing (LRB) response such as scragging, rate effects, contamination, temperature, and distance travelled. In design, these effects are conservatively bounded in an estimated sense by an analysis with upper and lower bound property modification factors to capture the range of response (McVitty and Constantinou 2015). In an effort to more accurately predict bearing behavior, more advanced models are examined in this chapter. Specifically, the temperature effect in the lead core of LRBs are examined by comparing simple, more widely used, models with the recently developed *LeadRubberX* model (Kumar et al. 2014). A base isolated structure using various models for the isolation system is examined under various types of ground motions to evaluate the performance of the model.

Upper and lower bound values for bearing properties are used by applying property modification factors to the LRB's post elastic stiffness and characteristic strength, in an effort to bound the response of the isolators. The factors that are applied to obtain the upper and lower bound are used to account for any possible response it may have throughout the isolator's design life. In the current design approach, the method used for analyzing upper and lower bound, is typically done to bound the possible maximum forces and the maximum displacements. The lower bound mainly accounts for the maximum displacements. The upper bound is conducted to find the maximum forces that can be achieved in the isolators due to the increased characteristic strength of the isolator along with scragging effects of the rubber.

Various studies have examined the effects of isolation bearing properties on the structural system response using bounding analyses. A recent study examined the *LeadRubberX* model for strength degradation by conducting a nonlinear response time history analysis (NLRHA) on an isolated hospital in Turkey subjected to near fault excitations (Özdemir and Avşar 2017). It was reported that the upper and lower bounds of bearing properties were able to, for the most part, bound the response. In this study, a similar analysis will be conducted however only applying the modification factors to the characteristic strength of the bearing to observe if the heating effects of the *LeadRubberX* model is bounded by the lower and upper bounds. An isolated ordinary concentric braced frame (OCBF) will be analyzed using lower and upper bound analysis comparing against the strength degrading model for short and long-duration ground motions scaled using procedures in ASCE 7 (2017)

3-2 Building Model

The 3-story building investigated here is based on the hypothetical model that was designed by professional engineers and described by Erduran et al. (2011). The building consists of a 4 by 6 bay OCBF building modeled in OpenSees (2014) with the layout shown in Figure 3-1. The buildings center of gravity was purposefully placed off-centered to incite torsional effects.

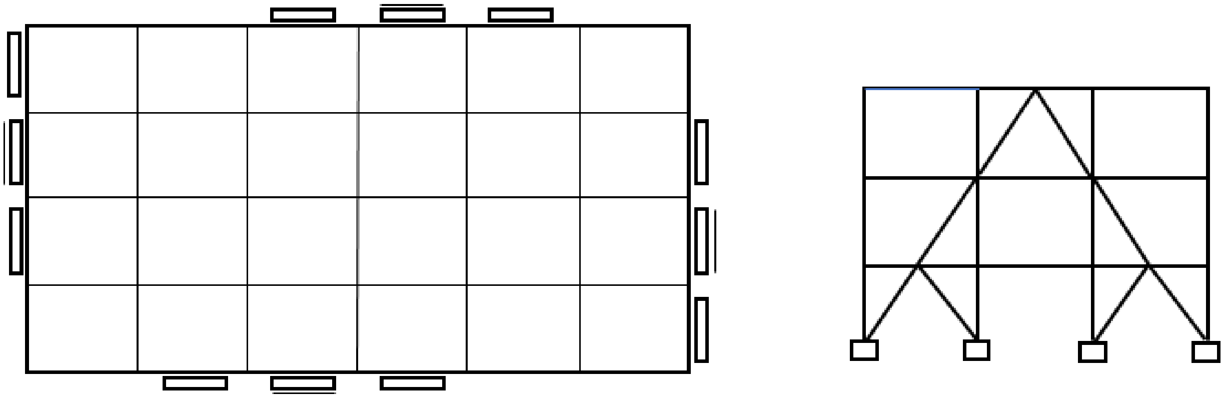

Figure 3-1 OCBF building model in OpenSees (Left: Plan view of building model and brace layout. Right: Brace Configuration.)

This office building (occupancy category II and importance factor of I=1.) was designed to meet the requirements of the Equivalent Lateral Force (ELF) Method (Erduran et al. 2011). The building was designed at the location (34.50N, 118.2W) in Los Angeles on stiff soil (site class D with reference shear wave velocity of 180 to 360 m/s). The spectral values have changed since the building was designed, however to be consistent with previous studies, the same values were used in this study. The mapped spectral accelerations for this location are S_S=2.2g for short periods and S_1=0.74g for a 1-s period (g=gravitational acceleration).

For this building, the fundamental time period was chosen to be $T_M = 3.07\ sec$ and $\beta_M = 15.8\%$. The design displacement is calculated by using the equation from ASCE (2017) as follows:

$$D_M = \frac{gS_{M1}T_M}{4\pi^2 B_M} \qquad (3-1)$$

where B_M is the coefficient for damping and S_{M1} is 1-s spectral accelerations for the corresponding events. The design displacement resulted in D_M=24.3 inches and with the accidental torsion effects considered D_{TM}= 29.16 inches.

3-3 Numerical Modeling

The LRB model utilized for analysis is the *LeadRubberX* model which was implemented in OpenSees (2014) by Kumar et al. (2014). The model includes the addition of the lead core heating effects (Kalpakidis and Constantinou 2009a) by modifying the generalized bidirectional Bouc-Wen mathematical model (Park et al. 1986; Wen 1976). The hysteretic portion of the model allows for degradation by incorporating the temperature dependence of the yield strength, $\sigma_{YL}(T_L)$. The forces F_x and F_y and displacements U_x and U_y along orthogonal directions x and y, respectively, are as follows:

$$\begin{Bmatrix} F_x \\ F_y \end{Bmatrix} = c_d \cdot \begin{Bmatrix} \dot{U}_x \\ \dot{U}_y \end{Bmatrix} + K_d \cdot \begin{Bmatrix} U_x \\ U_y \end{Bmatrix} + (\sigma_{YL}(T_L)A_L) \cdot \begin{Bmatrix} Z_x \\ Z_y \end{Bmatrix} \qquad (3-2)$$

In Equation 3-2, the overdot denotes differentiation with respect to time, $[I]$ is the identity matrix and dimensionless parameters Z_x and Z_y, are bounded by the values of ±1. The post-elastic stiffness is denoted by K_d. For LRBs, typically c_d is the viscous damping in the rubber, however for natural rubber it is typically set to zero and only shown here for completeness.

3-3-1 Bounding Analyses

With the obtained design values (Equation 3-1), the material properties such as the post elastic stiffness and characteristic strength were obtained. With the given quantities, it was possible to deduce dimensions of the bearing required for the *LeadRubberX* model (Kumar et al. 2014). As seen in Figure 3-2, the dimensions of the interior isolator are shown.

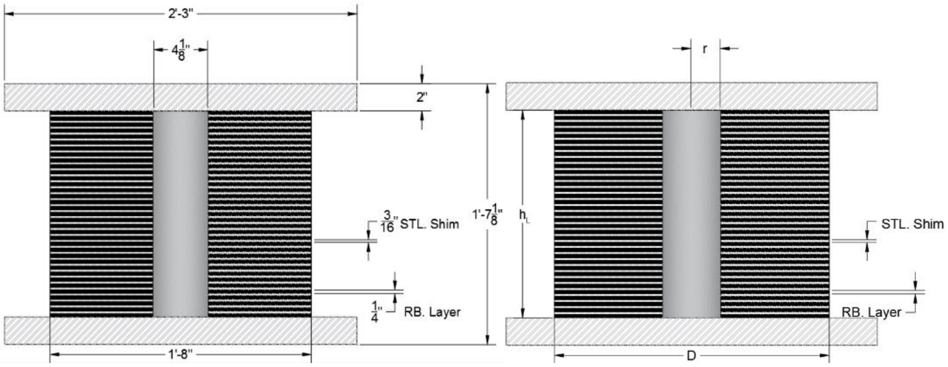

Figure 3-2 Interior isolator dimensions for OCBF building.

In this analysis, the upper and lower bound property modification factors are only considered for the characteristic strength of the bearing. Since only the lead core heating is being analyzed and compared to the upper and lower bounds, the initial and post-elastic stiffness are unaltered. The yield strength of the bearings were chosen to be σ_L =10 MPa which is typical for LRBs. The upper bound for the characteristic strength of the lead core was set to be σ_u=1.35*σ_L= 13.5 MPa (Constantinou et al. 2007). As shown in Table 3-1, three cases are analyzed, the upper bound, the nominal value (with the inclusion of heating of lead core), and lower bound case. The nominal case, for the *LeadRubberX* model, commences at the upper bound value and accounts for lead strength degradation during simulations to observe if exceedance of the bounds will occur. The upper and lower bounds do not consider the heating effects and have a fixed characteristic strength. The nominal (heating) case, in order to reduce below the lower bound characteristic strength, has to overcome the conservative value of 75% reduction of the upper bound value. In ASCE 7-16, the default lower bound value is 80% of the nominal and therefore the 75% reduction factor is conservative.

Table 3-1 Properties of upper and lower bound analyzed cases.

	Upper Bound	Nominal (heating)	Lower bound
$Q_D, Characteristic\ Strength\ [kip]$	654.4	654.4	484.7
$k_1, Initial\ stiffness\ [kip/in]$	1290.5	1290.5	1290.5
$k_2, Post\text{-}\ elastic\ stiffness\ [kip/in]$	59.3	59.3	59.3

Previous works (Kalpakidis and Constantinou 2009b; Özdemir and Avşar 2017) have also conducted similar nonlinear analysis for 1-D and 2-D directions, however, only considering near-fault short duration ground motions. Their conclusions were similar, concluding that the upper and lower bound were able to mainly bound the results of the *LeadRubberX* model that accounts for the strength degradation of the lead core. For this reason, the ground motions selected for this analysis includes long duration ground motions.

In order for a ground motion to achieve long duration status, the following criteria was required to be met: significant duration Ds_{5-95} of at least 45s or the significant duration Ds_{5-75} of at least 25s (Chandramohan et al. 2016). The significant duration value is calculated by using one of the components and calculating the cumulative energy of the ground motion for 5-95% or 5-75% of the motion, and measuring the amount of time for each component to achieve the cumulative energy, and selecting the longer duration (Chandramohan et al. 2016). This method was used to distinguish between short duration and long duration ground motions. The significant duration method is utilized as it is the most suitable duration metric (Chandramohan et al. 2016). This method is unaffected by scaling, does not bias spectral shape, and is uncorrelated to common IMs like PGA and Sa(1s) (Bommer et al. 2004).

A total of 20 ground motions were selected from PEER NGA-West2 (Ancheta et al. 2013). Seven ground motions were near-fault and seven were long-duration ground motions. Since the location is based in Los Angeles (LA), the fault type was required to be strike-slip fault for the 14 ground motions. The remaining six motions were reverse and reverse oblique and are analyzed separately and shown in Table 3-2 in grey highlight. To find the appropriate ground motions in the PEER database, several constraints were implemented such as: soil site class D, within 50km of rupture, and the scale factor being less than 10 which is recommended (Bommer et al. 2004). As shown in Table 3-2, the scale factor for each ground motion is less than 10 and the average is equal to 4.26. The magnitude range was 6.5-7.8 as recommended in the Department of Conservation California Geological Survey (USGS 2005).

Table 3-2 List of ground motions utilized in NLRHA (Short and Long-duration ground motions) (Highlighted gray: Reverse and Reverse oblique)

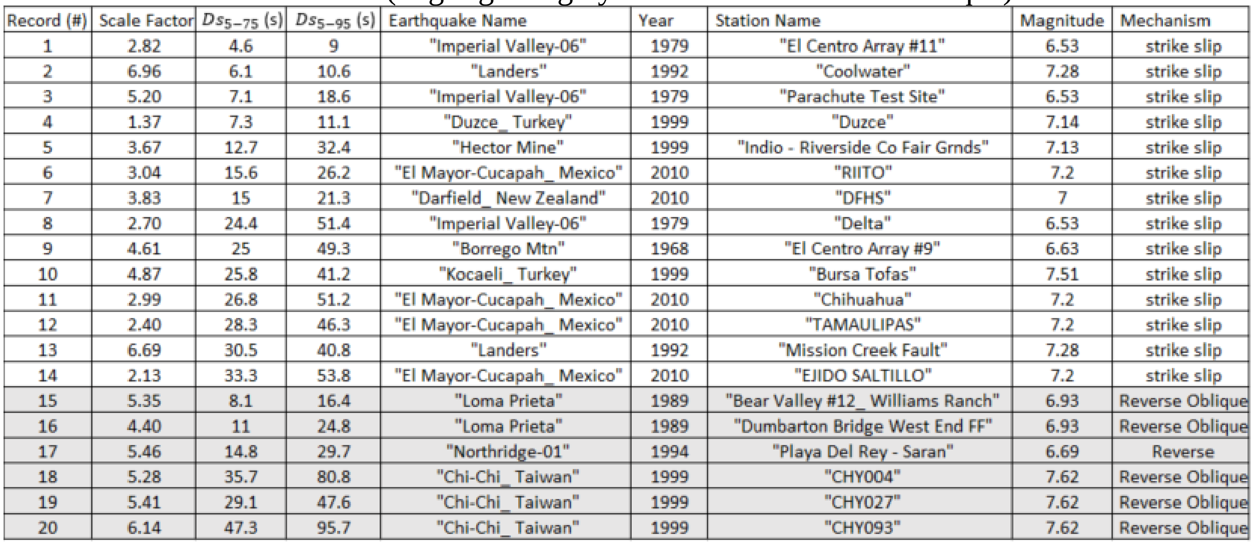

Record (#)	Scale Factor	Ds_{5-75} (s)	Ds_{5-95} (s)	Earthquake Name	Year	Station Name	Magnitude	Mechanism
1	2.82	4.6	9	"Imperial Valley-06"	1979	"El Centro Array #11"	6.53	strike slip
2	6.96	6.1	10.6	"Landers"	1992	"Coolwater"	7.28	strike slip
3	5.20	7.1	18.6	"Imperial Valley-06"	1979	"Parachute Test Site"	6.53	strike slip
4	1.37	7.3	11.1	"Duzce_ Turkey"	1999	"Duzce"	7.14	strike slip
5	3.67	12.7	32.4	"Hector Mine"	1999	"Indio - Riverside Co Fair Grnds"	7.13	strike slip
6	3.04	15.6	26.2	"El Mayor-Cucapah_ Mexico"	2010	"RIITO"	7.2	strike slip
7	3.83	15	21.3	"Darfield_ New Zealand"	2010	"DFHS"	7	strike slip
8	2.70	24.4	51.4	"Imperial Valley-06"	1979	"Delta"	6.53	strike slip
9	4.61	25	49.3	"Borrego Mtn"	1968	"El Centro Array #9"	6.63	strike slip
10	4.87	25.8	41.2	"Kocaeli_ Turkey"	1999	"Bursa Tofas"	7.51	strike slip
11	2.99	26.8	51.2	"El Mayor-Cucapah_ Mexico"	2010	"Chihuahua"	7.2	strike slip
12	2.40	28.3	46.3	"El Mayor-Cucapah_ Mexico"	2010	"TAMAULIPAS"	7.2	strike slip
13	6.69	30.5	40.8	"Landers"	1992	"Mission Creek Fault"	7.28	strike slip
14	2.13	33.3	53.8	"El Mayor-Cucapah_ Mexico"	2010	"EJIDO SALTILLO"	7.2	strike slip
15	5.35	8.1	16.4	"Loma Prieta"	1989	"Bear Valley #12_ Williams Ranch"	6.93	Reverse Oblique
16	4.40	11	24.8	"Loma Prieta"	1989	"Dumbarton Bridge West End FF"	6.93	Reverse Oblique
17	5.46	14.8	29.7	"Northridge-01"	1994	"Playa Del Rey - Saran"	6.69	Reverse
18	5.28	35.7	80.8	"Chi-Chi_ Taiwan"	1999	"CHY004"	7.62	Reverse Oblique
19	5.41	29.1	47.6	"Chi-Chi_ Taiwan"	1999	"CHY027"	7.62	Reverse Oblique
20	6.14	47.3	95.7	"Chi-Chi_ Taiwan"	1999	"CHY093"	7.62	Reverse Oblique

The amplitude scaling procedure used, consists of applying the same scale factor to each horizontal pair component as suggested in the National Earthquake Hazards Reduction Program (NEHRP 2011). As discussed in Chapter 17 of ASCE 7-16, the time period range of scaling of the horizontal ground motion have been updated since ASCE 7-10 (2010). Since the fixed base structure will not be analyzed from Erduran et al. (2011), the period range for the target hazard spectrum differs. Rather than the scaling being performed for the period range of $0.2T_M$ to $1.5T_M$, the scaling will be conducted from the period range, per section 17.4, of $0.75T_{M,upper}$ to

$1.25T_{M,lower}$ (ASCE 2017). The MCE design period is 3.1s, meaning that the scaling will be from 2.145 to 3.875s. The lower bound time period ($0.75\,T_{M,upper}$) is calculated by using the upper bound values of the isolation system and calculating the period of the structure per ASCE 7-16. Conversely, the upper bound time period ($1.25T_{M,lower}$) is calculated using the lower bound values of the isolation system. In Figure 3-3, the mean spectrum can be observed along with the individual ground motion spectrums plotted in light grey. It can be observed that for some ground motions at the short period range there are large acceleration values. This is due to the fact that scaling was done between the 2 to 4 sec range, disregarding the distribution out of this period range. From the periods between 2 to 4 seconds, the deviation from the mean spectrum can be observed to be minimized.

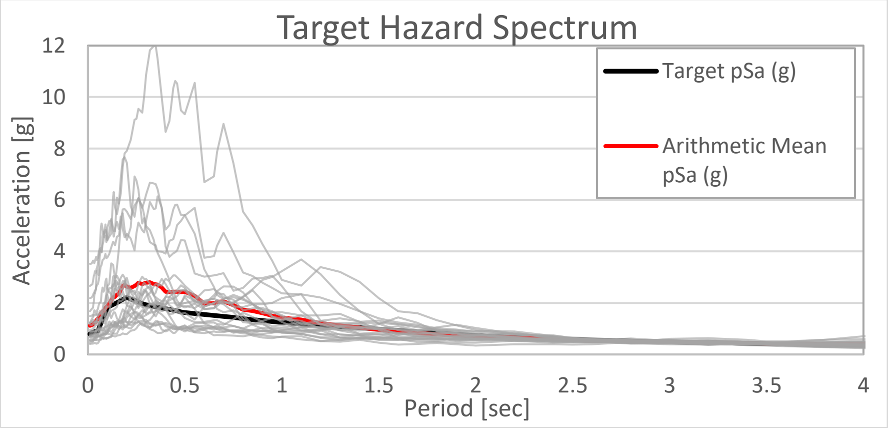

Figure 3-3 Target hazard spectrum: 2% PE in 50 years hazard level (MCE level).

3-3-2 Results

In this section, the nonlinear response history analysis (NLRHA) of the twenty ground motions is analyzed using OpenSees. In Figure 3-4, the lower bound maximum displacements are compared against the displacements obtained by the *LeadRubberX* model which includes the heating effects. The percent increase indicates the amount the displacement of the heating case exceeds the lower bound displacement. It is important to note that the maximum displacements are calculated by finding the magnitude of the x and y directions. The heating case has the same material properties initially as the upper bound, however the strength degradation due to the heating effects are considered. The first seven ground motions on the top portion of the bar graph shows the response for the short-duration ground motions, and the bottom seven show the response for the long-duration ground motions. It is also important to note that the pairs of ground motions were applied orthogonal directions east-west and north-south direction (Figure 3-4a). Then the directions were switched (Figure 3-4b). Since similar results were obtained only one configuration was utilized for further analysis.

In Figure 3-4, it can be seen that the overall displacements for short duration ground motions are greater than those of long duration ground motions. However, the percent increase of the displacements due to the heating effects compared to the lower bound is significantly higher in long-duration ground motions compared to short duration ground motions. These percent differences may be important when considering designing bearings using ELF approach. The upper and lower bound may not suffice when designing isolators or providing sufficient distance for the clearance of the isolation system.

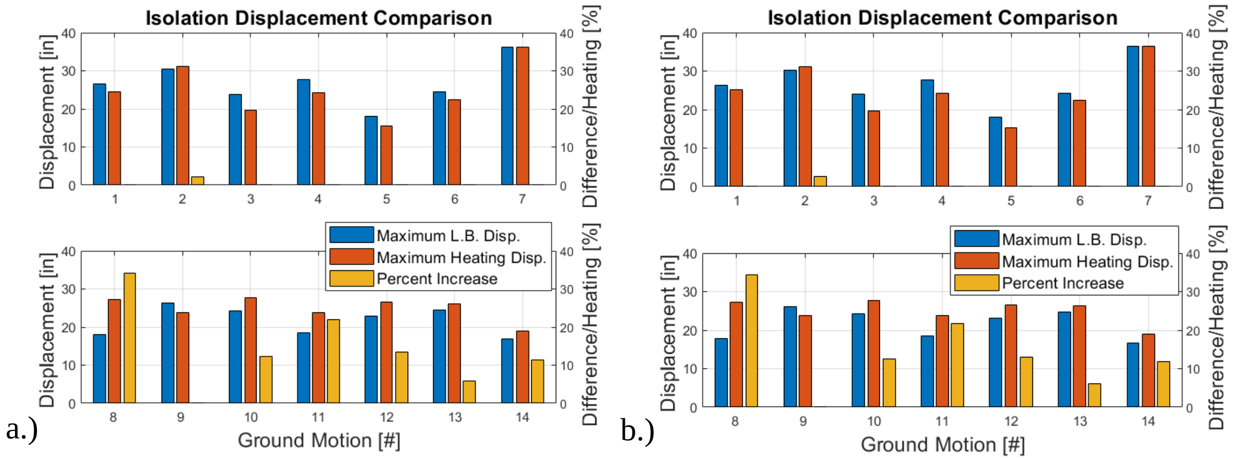

Figure 3-4 Lower-Bound comparison with Heating case: (Top: Short-duration) (Bottom: Long-Duration) a.) GM dir1 b.) GM dir2.

In Figure 3-5, the ground motion, velocity time-history, and hysteresis are shown for ground motions (GMs) 2 and 10. GM 2 is a short duration ground motion which is the only short-duration ground motion that the heating case exceeded the lower bound maximum displacement. Ground motion 2 has a large excursion invoking large displacement and velocity demands. The *LeadRubberX* model exceeds the lower bound by about 3%. As for the long duration ground motion 10, the displacement exceeded the lower bound by about 45%. The peak velocity for GM 10 is half of GM 2, however due to the accumulated temperature increase caused by the long duration ground motion, it resulted in significant strength degradation leading to larger exceedance of displacements to that of the lower bound.

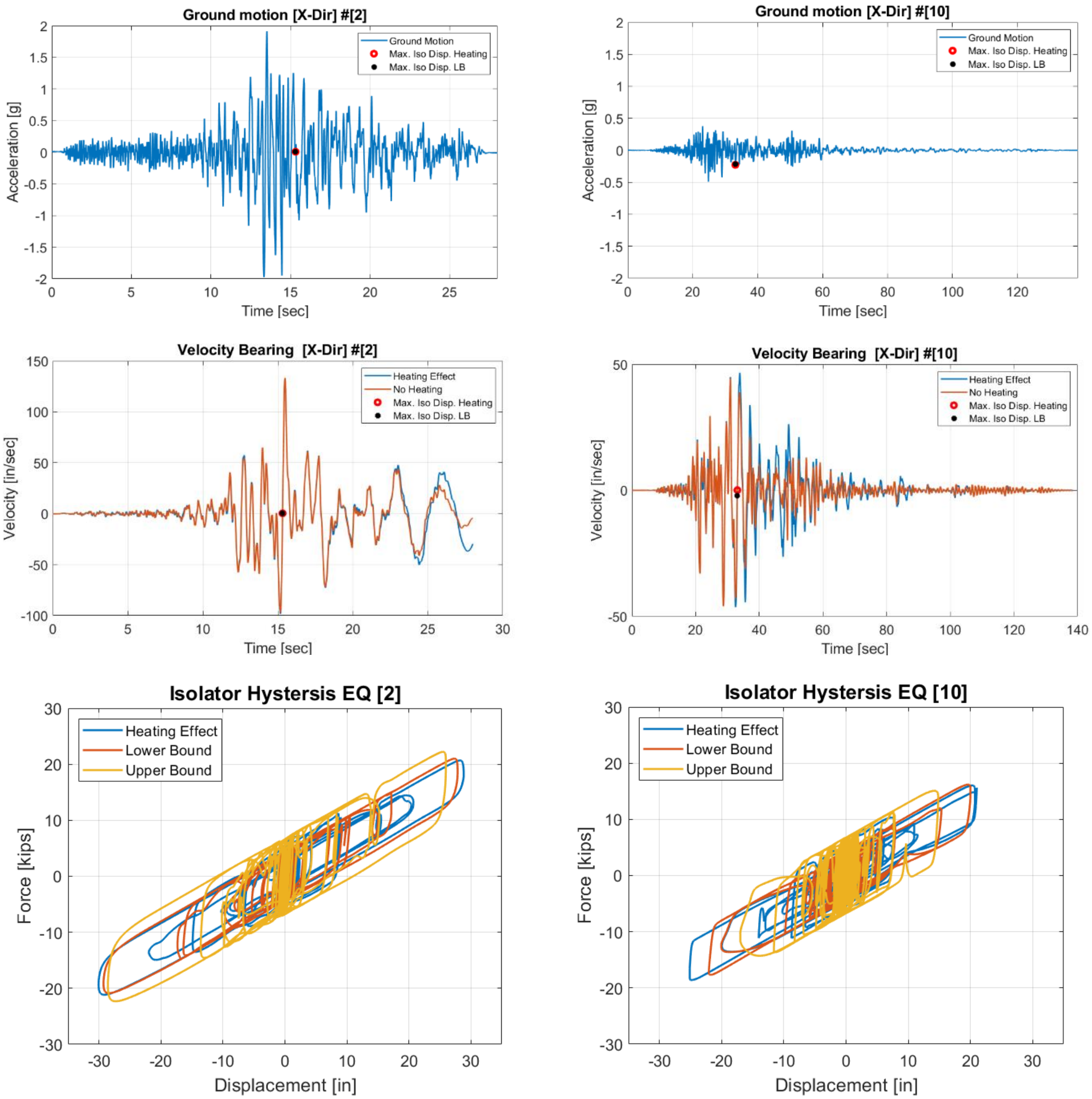

Figure 3-5 Example results GM-2 (short-duration) and GM-10 (long-duration).

In Figure 3-6, the significant duration 5-95% is compared against the percent increase in heating displacement to the lower bound maximum displacement. A clear trend can be observed, as the significant duration increases, the percent increase of the heating to the lower bound maximum displacement, increases. As mentioned before, the classification of a long-duration ground motion is determined as significant duration reaches 45 seconds or greater.

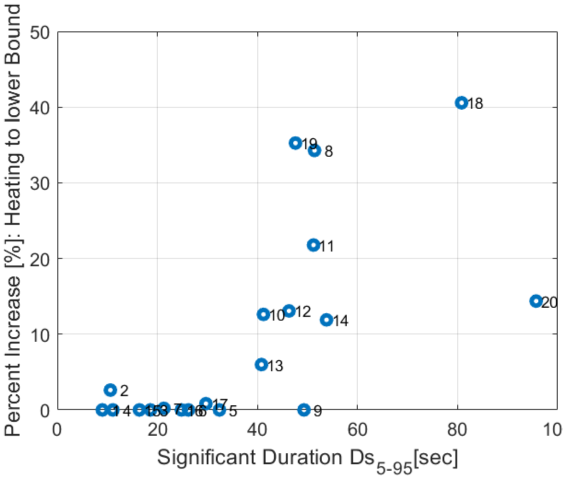

Figure 3-6 Displacement increase versus significant duration 5-95%

In Figure 3-6, it can be observed that the exceedance in displacements occurs as the significant duration reaches near the 45 second threshold. For this figure the plot is not shown for the case in which the ground motion pairs are changed orthogonally for the second direction due to the fact that the results were identical. Ground motions 15-20 were included to compare with the behavior of reverse and reverse oblique type earthquakes. It can be seen that ground motion 20 is an outlier in the analyzes, while 15-19 follow the trend. With all ground motions included the norm of residuals is a value of 0.61. With ground motions 1-14, the norm of residuals is a value of 0.39, meaning it has a stronger correlation.

3-4 Conclusion

In this chapter, the ASCE upper and lower bound methodology is compared with a nonlinear time history analysis, by using various LRB models. The *LeadRubberX* model, is able to capture the lead core strength degradation effects due to heating and is used to compare with the characteristic strength property modification factors. The factors are applied to two smooth bilinear models representing the upper and lower bounds for the *LeadRubberX* model to examine if the bounds suffice for short duration and long-duration ground motions. The short duration ground motions reached larger displacements overall for the heating and lower bound cases. However, for long duration ground motions, the percent of exceedance in the maximum displacements when comparing heating case to the lower bound case resulted in the heating case exceeding the maximum displacements by 50%. Default modification factors may not be satisfactory in bounding, especially for long duration ground motions.

It was observed that a significant correlation exists between significant duration and the increase in displacements when comparing the heating case to the lower bound case. For long-duration ground motions, a nonlinear analysis is recommended since the heating case exceeded the lower bound maximum displacements. The significant duration measure for distinguishing short from long duration ground motions has a significant impact in the heating of the lead core. Additional studies should be conducted using a wider variety of ground motions since the small sample of reverse and reverse oblique faults resulted in variable effects on lead core heating.

Chapter 3, in part, are a reprint of the material as it appears in “Response of a Seismically Isolated Structure with Lead Rubber Bearings Considering Heating Effects.” Marquez, J. F., and Mosqueda, G., *Proceedings of the 11th National Conference in Earthquake Engineering, Earthquake Engineering Research Institute (2018).* The dissertation author was the primary investigator and author of this paper.

3-5 Reference

Ancheta, T., Darragh, R., Stewart, J., Seyhan, E., Silva, W., Chiou, B., Wooddell, K., Graves, R., Kottke, A., Boore, D., Kishida, T., and Donahue, J. (2013). “PEER NGA-West2 Database, Technical Report PEER 2013/03.” (May 2013).

ASCE. (2010). *Minimum Design Loads for Buildings and Other Structures, American Society of Civil Engineers*. ASCE/SEI Standard 7, Reston, VA.

ASCE. (2017). *Minimum Design Loads and Associated Criteria for Buildings and Other Structures*. ASCE/SEI Standard 7, Reston, VA.

Bommer, J. J., Magenes, G., Hancock, J., and Penazzo, P. (2004). “The influence of strong-motion duration on the seismic response of masonry structures.” *Bulletin of Earthquake Engineering*, Springer, 2(1), 1–26.

Chandramohan, R., Baker, J. W., and Deierlein, G. G. (2016). “Quantifying the influence of ground motion duration on structural collapse capacity using spectrally equivalent records.” *Earthquake Spectra*, 32(2), 927–950.

Constantinou, M. C., Whittaker, A. S., Fenz, D. M., and Apostolakis, G. (2007). *SEISMIC ISOLATION OF BRIDGES*.

Erduran, E., Dao, N. D., and Ryan, K. L. (2011). “Comparative response assessment of minimally compliant low-rise conventional and base-isolated steel frames.” *Earthquake Engineering and Structural Dynamics*, John Wiley and Sons Ltd, 40(10), 1123–1141.

Kalpakidis, I. V., and Constantinou, M. C. (2009a). “Effects of Heating on the Behavior of Lead-Rubber Bearings. I: Theory.” *Journal of Structural Engineering*, 135(12), 1440–1449.

Kalpakidis, I. V., and Constantinou, M. C. (2009b). “Effects of Heating on the Behavior of Lead-Rubber Bearings. II: Verification of Theory.” *Journal of Structural Engineering*, 135(12), 1450–1461.

Kumar, M., Whittaker, A. S., and Constantinou, M. C. (2014). “An advanced numerical model of elastomeric seismic isolation bearings.” *Earthquake Engineering & Structural Dynamics*, 43(13), 1955–1974.

McVitty, W. J., and Constantinou, M. C. (2015). “Property modification factors for seismic isolators: Design guidance for buildings.” *MCEER Report*, 15–0005.

NEHRP. (2011). *Selecting and Scaling Earthquake Ground Motions for Performing Response-*

History Analyses.

OpenSees. (2014). “Open system for earthquake engineering (Version 2.4.4).”

Özdemir, G., and Avşar, Ö. (2017). “Use of Bounding Analyses to Estimate the Performance of a Seismically Isolated Structure.” *Anadolu University Journal of Science and Technology A - Applied Sciences and Engineering*, Anadolu Universitesi Bilim ve Teknoloji Dergisi-A: Uygulamali Bilimler ve Muhendislik, 18(1), 161–161.

Park, Y. J., Wen, Y. K., and Ang, A. H. (1986). “Random vibration of hysteretic systems under bi-directional ground motions.” *Earthquake Engineering & Structural Dynamics*.

USGS. (2005). “Department of Conservation California Geological Survey: Seismic Hazard Zone Report.”

Wen, Y. K. (1976). “Method for Random Vibration of Hysteretic Systems.” *Journal of the Engineering Mechanic Division*, 102(2), 249–263.

Chapter 4 MODELING OF LEAD RUBBER BEARINGS UNDER LARGE CYCLIC MATERIAL STRAINS

Recent models for elastomeric bearings have been introduced by Kumar et al. (2014), Ishii and Kikuchi (2019a), and Oliveto et al. (2019). These models are currently utilized for modeling LRBs and high damping rubber (HDR) bearings and are mostly based on observed experimental response. Kumar et al. (2014) introduced a model in *OpenSees* (OpenSees 2014) that accounts for strength degradation due to heating of lead core and vertical loads on LRBs. Kikuchi and Aiken (1997) introduced a detailed model that is able to capture the complex behavior of high damping rubber bearings and lead rubber bearings. The model was later refined to include the effects of large axial loads by accounting for P-Δ effects and for a nonuniform initial compression modulus and is also available in *OpenSees* (Ishii and Kikuchi, 2019; Kikuchi et al. 2010). Oliveto et al. (2019) proposed a combination of models for the calibration of high damping rubber bearings (HDRs), integrating a hyperelastic and hysteretic models in order to calibrate for many bidirectional tests up to 200% shear strain.

Only a few experimental programs of large sized bearings have been reported (e.g., CERF, 1998). Using the data from large bearing tests by Kim et al. (2017, 2019) to evaluate current models, it was identified that one model could not capture the dominant nonlinear behaviors observed in testing of large size bearings to near ultimate strains. Such models are necessary to simulate the seismic response of base isolated structures through a wide range of shaking including Beyond Design Basis Earthquakes (BDBE). The objectives of this study are to characterize the nonlinearities observed in LRBs and propose a model that captures this behavior from small to large strains. Experimental results presented in the next section demonstrate the complexities of the LRBs behavior through a wide range of strains. A parallel model is proposed to capture these observed behaviors including i) strength degradation in the lead due to heating (Kalpakidis and Constantinou 2009b), ii) hardening of the elastomer at large strains (Grant et al., 2004) and iii) Mullins and scragging effects that can be expected to manifest within the lifetime of the bearings when considering BDBE or Maximum Considered Earthquake (MCE) shaking (Dall'Asta and Ragni, 2008). The influence of these modeling parameters on predicting the behavior of isolated structures is examined to arrive at a practical model for accurate numerical simulations. The current model is developed for one-dimensional (1D) simulations focusing on material behavior under large amplitude cyclic strains and does not account for axial load effects, limitations that will be addressed in future versions of the model.

4-1 Experimental Bearing Behavior

The complex nonlinear behavior exhibited by LRBs is examined through experimental data of large scale LRB tests conducted at the University of California San Diego Seismic Response Modification Device Facility (SRMD). The bearings tested were designed for a nuclear power plant applications with dimensions shown in Figure 4-1. Two identical bearings were tested under a range of cyclic shear strain amplitudes and strain rates. The test data from one of the two LRBs is used for the development and verification of the unidirectional model proposed here. Importantly, the set of parameters obtained in this analysis to characterize the LRB will require recalibration as the bearing size changes (i.e. shape factor) or axial load differs (Sheridan et al. 2012)

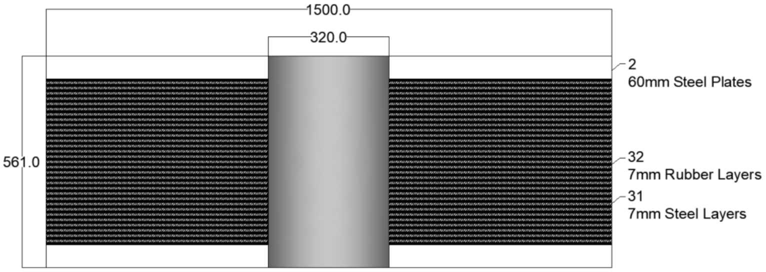

Figure 4-1 Lead rubber bearing dimensions (in mm)

The bearings were subjected to various characterization tests, with only the tests considered in this study shown in Table 4-1 for brevity. Detailed information on the full test series is provided by (Kim et al. 2019). The original test number is shown to indicate the order and sequence of tests. The tests were selected to verify bearing behavior for a wide range of strains and strain rates. The experimental tests verified that the bearing is able to withstand up to 500% shear strain in 1D and well over 400% shear strain in 2D loading patterns (Eem and Hahm 2019; Kim et. al 2017). Considering this range of strains, a model that can account for the observed nonlinearities at these high strains is investigated. A constant axial load of 22,000 kN, corresponding to an average pressure of 13MPa (considering area of rubber) was applied for all tests. This axial load is less than 20% of the undeformed bearing buckling load for which no stiffness degradation was observed. The axial behavior of the bearing and horizontal-vertical coupling effects are not examined here since the experimental data is not sufficient to provide further insight. The importance of axial load variation has been highlighted in other studies (Koh and Kelly 1988; Ryan et al. 2005; Sanchez et al. 2013; Sarebanha et al. 2019; Vemuru et al. 2016; Warn et al. 2007).

Table 4-1 Test log (Tests utilized for calibration)

Test (#)	**Strain (%)**	**Max Strain Rate (1/s)**	**Type**	**Number of cycles**
14	100	1.3	Sine	3
8	200	2.5	EQ	EQ
11	300	3.8	Sine	1
13	400	5.0	Sine	1
15	500	6.3	Sine	1

A review of the experimental data highlights complex nonlinear behaviors that deviate from a typical bilinear model with constant parameters typically used to model seismic isolators. As shown in Figure 4-2a, the lead contributes to two types of nonlinearities: initial lead hardening and strength degradation due to heating of the lead core. Initially, the lead displays a strain hardening behavior that is prevalent in the initial cycle as the strength increases. However, as the lead temperature increases from repeated cycling, strength degradation of the lead is evident. In Figure 4-2b, two sources of observed nonlinearities are caused by the rubber: hardening and unloading effects. These various nonlinearities shown in LRBs are further examined in this study to capture these effects in models and to quantify the influence these behaviors have on the seismic response of structures isolated with LRBs.

Initial hardening of the lead has been documented in past experiments on LRBs (Kalpakidis and Constatinou 2008; McVitty and Constantinou 2015; Sanchez et al. 2013; Tyler and Robinson 1984a). The cause of this has been speculated to be high speed instrument error, although this behavior has been observed at varying strain rates in previous studies. A study of a pure lead specimen tested in shear at a low strain rate also displayed this initial hardening phenomenon (Aramaki et al. 2004), confirming the source to be a lead behavior. A mathematical model is later introduced to account for this initial hardening and found to be beneficial in better estimating the bearing characteristic strength. Lead heating and associated strength degradation has been studied in detail by Kalpakidis and Constantinou (2009a). The heating of the lead as it undergoes cyclic plastic deformation, because of the lead's malleability and low melting point, results in strength degradation. Kalpakidis and Constantinou (2009a) examined the lead core of LRBs and were able to predict the temperature of the lead core and relate the temperature to the strength utilizing thermodynamic equations that were verified experimentally in cyclic tests (Kalpakidis and Constantinou 2009a). Kumar et al. (2014) introduced a state-of-the-art model *LeadRubberX* implemented in OpenSees (OpenSees 2014) that includes this lead heating formulation.

The rubber also contributes to the complex bearing behavior by exhibiting hardening and pronounced unloading effects (Figure 4-2b). Mullins' effect, also sometimes referred to as scragging, contributes to the softening behavior due to the cyclic reduction of the bulk modulus of elastomers at moderate-to-high shear strains (Mullins 1969). For seismic isolation purposes, the two main components of Mullins effect are considered: i) Stress softening due to a strain exceeding a previously maximum strain causing 'permanent' damage (often interchanged with scragging damage), and ii) Cyclic damage or softening occurring for strains lower or equal to the maximum strain ever applied (Diani et al. 2009). While scragging has been considered a subset of Mullins effect, Clark et al. (1997) construed this effect into two different phenomena: scragging is the permanent damage or "long term" damage of the rubber when it reaches peak strains, and Mullins' effect is the "short term" damage that is accumulated as the rubber is being cycled. Scragging and Mullins effect may also cause the unloading effects that results in a widening of the hysteresis following a displacement reversal. Regardless of the root of this phenomenon, these need to be accounted for when conducting analysis of critical structures (Dall'Asta and Ragni, 2008). The larger the strains the bearing undergoes the larger the hardening and reversal effects are present. Ishida et al. (1991) studied two identical natural rubber bearings, one with a lead core and one without a lead core. Static tests were conducted, and the unloading effects occurred in both, substantiating that the unloading effect is due to the rubber and is not strain rate dependent.

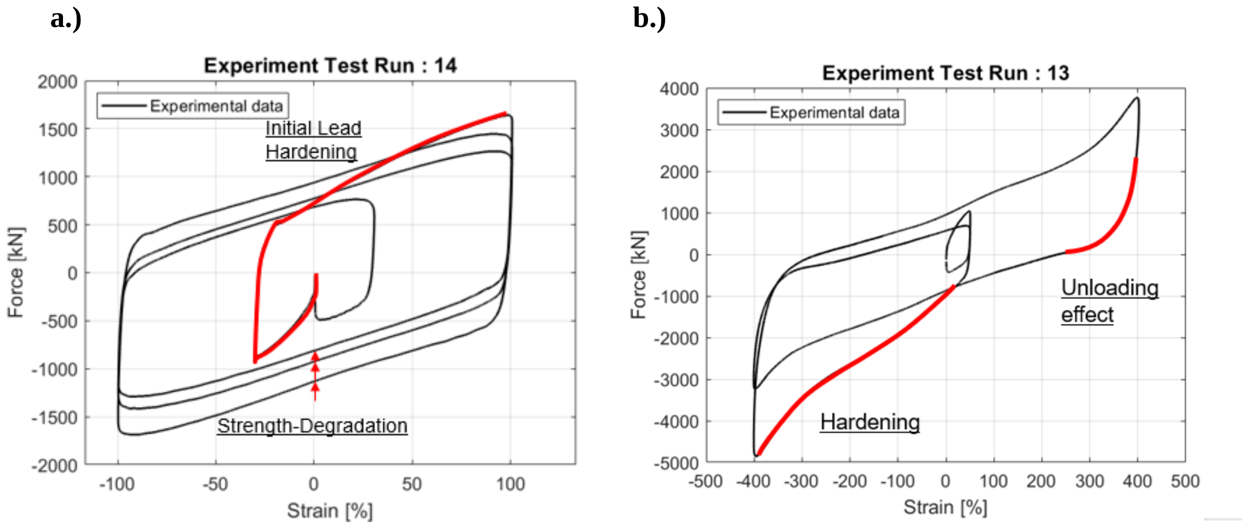

Figure 4-2 Nonlinear behavior in LRB experimental tests a.) lead: initial lead hardening and strength degradation b.) rubber: hardening and unloading effects

Table 4-2 Existing models for elastomeric bearings in *OpenSees*.

Bearing Models	Features	Limitations
LeadRubberX (Kumar et al. 2014)	**i)** Strength degradation due to lead heating, **ii)** cavitation and post-cavitation, **iii)** buckling load variation, **iv)** horizontal stiffness, **v)** vertical stiffness variation, **iv)** only requires dimensions and basic material properties.	**i)** No initial lead hardening, **ii)** no rubber strain hardening.
HDR Element (Grant et al., 2004)	**i)** Hyperelastic formulation can account for rubber hardening and Mullins and scragging effects in shear **ii)** cavitation and post-cavitation, **iii)** buckling load variation, **iv)** vertical stiffness variation.	**i)** Features are not optional in OpenSees, **ii)** isotropic damage in rubber.
KikuchiBearing Element (Kikuchi et al. 2010)	**i)** Multiple normal springs for large axial loads (P-Delta effects), **ii)** only requires dimensions and basic material properties.	**i)** No strength degradation due to lead heating, **ii)** no initial lead hardening, **iii)** no rubber hardening.

4-2 Numerical Modeling

Some of the more advanced bearing models available in *OpenSees* are listed in Table 4-2 identifying the features that the models capture. Note that various models include vertical load effects not considered in this study. Limitations of the models, particularly as related to capturing the bearing behaviors described in the previous section, are also included. To more accurately simulate LRB behavior, a parallel model for large strain LRB (LSLRB) is proposed consisting of a strength degrading plasticity model (heating of the lead core), a hyperelastic model for rubber hardening and a plastic portion for the unloading effects. A parallel model with different components was also proposed (Eem and Hahm 2019), but does not capture all salient characteristics of LRBs at various strains with one set of parameters. The components of the model are described next and build from components of existing models.

4-2-1 Hysteretic model

A hysteretic model was developed in order to capture behaviors such as lead core heating and initial lead hardening. The hysteretic model utilized and modified in this study is based on the model by Dafalias and Popov (1975) and later introduced into *OpenSees* by Grant et al. (2004) as the hysteretic portion of the *HDR element*. The formulation is as follows:

$$\boldsymbol{F}_2 = R\boldsymbol{n} - \delta\boldsymbol{\mu} \qquad (4-1)$$

$$R = (b_1 + b_2 \cdot K_{S2} \cdot \|\boldsymbol{U}\|) \qquad (4-2)$$

where,

$$\dot{\delta} = -b_3\delta\left\|\dot{\boldsymbol{U}}\right\| \qquad (4-3)$$

Since the appearance of the time derivatives in Equation 4-3 occurs on both sides of the equation it remains a rate independent model, furthermore, converting Equation 4-3 into temporal discretization results in the following equation:

$$\delta = \frac{\delta_n}{1 + b_3 \|\boldsymbol{U} - \boldsymbol{U_n}\|} \qquad (4-4)$$

The parameter δ is a scalar quantity that depends on the parameter b_3, which dictates the sharpness of the transition between one bounding surface to the other bounding surface for each reversal. The overdot denotes the derivative with respect to time and $\|\boldsymbol{U}\|$ represents the norm or magnitude of the displacement. The parameter, $\boldsymbol{U_n}$, denotes the previous time step while $\boldsymbol{U}$ denotes the current time step in Equation 4-4. The parameters δ and $\boldsymbol{\mu}$ are the magnitude and unit direction of the vector oriented from the current force point to the image force. R represents the bounding surface which is a function of the parameter b_1, the characteristic strength of the LRB, and b_2 is the hardening of the material that takes the form of a quadratic function of the displacement magnitude. K_{S2} is the scragging damage that varies from one to zero and is explained in a later section. More details on the model and parameters can be found in Grant et al. (2004).

4-2-1-1 Lead heating model

In order to capture the heating effects that occur in the lead core, the heating formulation proposed by Kalpakidis and Constantinou (2009a) was aggregated to the hysteretic model (Equation 4-2). Kalpakidis and Constantinou conducted experiments of lead specimens at different temperatures and found the ultimate strength of the lead in tension. Since LRBs are utilized for shearing, a simplified thermodynamic equation was identified in order to find the temperature of the lead plug and consequently the strength of the lead using a tension-shear strength relationship.

A thermodynamic equation consisting of material parameters of the lead and the steel shims through which heat dissipation occurs was proposed and shown below:

$$T_L(i+1) = T_L(i) + dT_L \qquad (4-5)$$

$$R(i+1) = R(i) \cdot \exp\big(-E_2 \cdot T_L(i+1)\big) \qquad (4-6)$$

The strength-temperature relationship constant, E_2, which was found experimentally to be 0.0069 (Kalpakidis and Constantinou 2009b) and dT_L, change in lead core temperature, is determined using thermodynamic equations that consist of material parameters of the LRB. In Equation 4-6, the bounding surface, $R(i+1)$, is modified by introducing strength degradation due to heating as the temperature of the lead core increases. Consequently, the plasticity model from Equation 4-1 is updated as shown in Equation 4-7:

$$\boldsymbol{F}_2 = R(T_L)\boldsymbol{n} - \delta\boldsymbol{\mu} \qquad (4-7)$$

The hysteretic force is a function of the temperature of the lead and therefore strength degradation of lead can be simulated. This formulation has been implemented in OpenSees as the *LeadRubberX* material model. It should be noted that an update to the model was recently proposed since the previous implementation only allowed an increase in lead core temperature (Kitayama and Constantinou 2021) and is included here.

4-2-1-2 Initial lead strain hardening

Initial lead hardening is exhibited in LRBs and shown in Figure 4-2a. This initial hardening has not been given much attention in modeling and is further examined here. In order to account for this phenomenon a new phenomenological model is introduced. This modeling approach is similar to the damage model for Mullins' and scragging introduced by Grant et al. (2004) with modifications. In Equation 4-8, the typical hysteretic force formulation is given.

$$\boldsymbol{F}_2 = R\boldsymbol{n} - \delta\boldsymbol{\mu} \qquad (4-8)$$

$$R = (b_1 + b_2 \cdot K_{S2} \cdot \|\boldsymbol{U}\|^2) \cdot KL \qquad (4-9)$$

where,

$$KL = 1 - c_5 \cdot e^{-c_6 \cdot DL} \qquad (4-10)$$

In Equation 4-10 it can be observed that the inverse of a typical damage parameter such as Mullins' and scragging discussed by Grant et al. (2004) is applied. The parameter *DL* increases with the accumulation of displacement increments which can be analogous to distance travelled. Parameters c_5 and c_6 are user inputs, the former varies from zero to one and the latter being any positive value. Accordingly, the model commences at a low yield point and then approaches the actual strength as *DL* increases, and consequently, *KL* increases to one (Equation 4-10). Comparisons to experimental data will be demonstrated later.

4-3 Rubber Model

4-3-1 Hyperelastic model

The second element in the parallel system is the hyperelastic model (Grant et al. 2004). This hyperelastic model is available in OpenSees (2014) as part of the *HDR element.* The elastic component uses the generalized Mooney-Rivlin strain energy function, with five elasticity constants. The model reduces to a fifth order equation with three constants $a_1, a_2,$ and a_3 as shown below:

$$\boldsymbol{F_1} = K_{S1}K_M[a_1 + a_2\|\boldsymbol{U}\|^2 + a_3\|\boldsymbol{U}\|^4]\boldsymbol{U} \qquad (4-11)$$

The elastic component is denoted by $\boldsymbol{F_1}$ and is a function of the displacement and damage parameters K_{S1} and D_M which account for scragging and Mullins' effect, respectively. More details are presented in a later section and formulations can be found in Grant et al. (2004). The hyperelastic behavior can be observed in Figure 4-4b. The hyperelastic element is utilized to provide a higher order equation to account for the rubber's behavior at low to high strains with the addition of being able to capture for Mullins' and scragging effects through damage parameters discussed in Section 4.3.3.

4-3-2 Unloading (Hysteretic) Model

In addition to the hyperelastic and the hysteretic model (i.e. including heating and lead hardening effects), an additional hysteretic model is included to capture the unloading effects. The previously mentioned hysteretic model is aggregated with carefully selected parameters, shown in Equations (4-1) and (4-2), to capture the hysteretic unloading effects as observed experimentally in Figure 4-2b. The parameter b_1 is essentially set to zero while b_2 is set to a finite number in order to have a bounding surface at higher strains. The b_3 parameter, which dictates the sharpness when unloading between one bounding surface to the opposing surface as shown in Figure 4-2b, is set to a low value in order to properly capture the unloading effects as have been observed at large strains and shown in Figure 4-4c.

4-3-3 Damage parameters

At large strains, characteristic behaviors representative of Mullins and scragging effects can be observed within the bearing and are considered here. These effects evolve with the loading history on the bearing. The equations used to account for damage effects are shown below:

$$K_{S1} = \exp\left(-c_1 D_s^3\right) \qquad (4-12)$$

$$K_{S2} = \exp\left(-c_2 D_s^3\right) \qquad (4-13)$$

$$K_M = c_3 + (1-c_3)\exp\left(-c_4 D_M^3\right) \qquad (4-14)$$

The parameters c_1-c_4 are input parameters that are calibrated with experimental data. K_{s1} and K_M are damage factors that affect the hyperelastic portion of the model. K_{S2} effects the hardening portion of the plasticity model as shown in Equation 4-2. Parameters c_1 and c_2 , are the damage parameters that account for degradation due to scragging effects and parameters c_3 and c_4 account for degradation due to Mullins effect. The evolution of the damage parameters can be seen in Figure 4-3, where D_s is the scragging damage parameter and D_M, is the damage parameter for Mullins' effect. The damage parameters evolution for Test 13 are shown and it can be observed that damage is carried over from Test 11 since scragging is the 'permanent damage'. Mullins effect, D_M, on the other hand is initially set to zero (short term damage), and the accumulation of damage increases as it is being cycled.

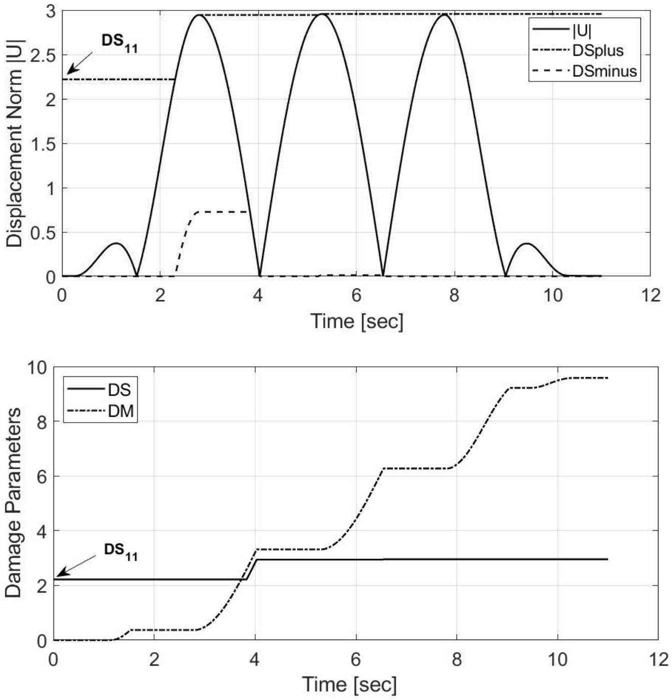

Figure 4-3 Damage parameter evolution due to displacement norm (Test 13 example).

4-4 LSLRB Model

A parallel system consisting of the three models (hysteretic model, hyperelastic model, and unloading model) is proposed and named LSLRB model (Figure 4-4). The hysteretic model accounts for the heating of the lead and the initial lead hardening, the hyperelastic model accounts for the hardening effects at large strains and damage parameters, and the unloading (hysteretic) model accounts for the unloading effects that are seen at higher strains.

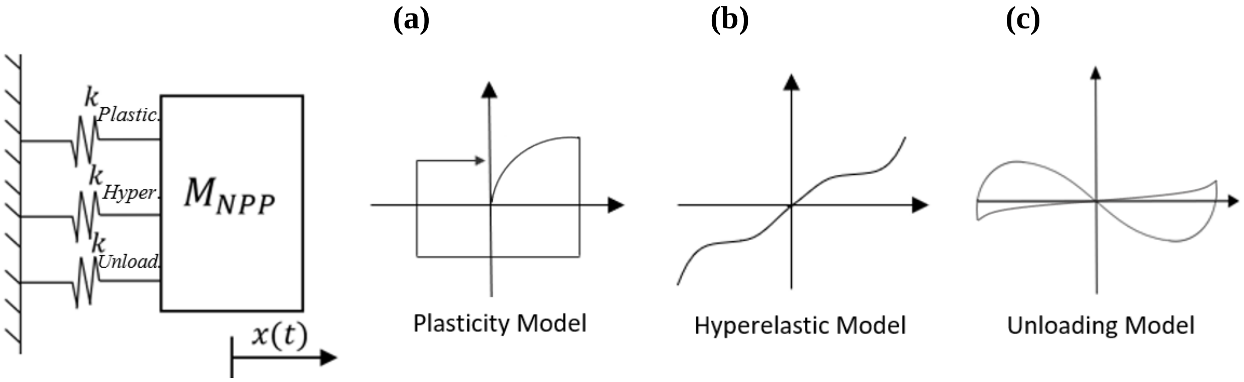

Figure 4-4 Parallel System. **(a)** Plasticity (heating and LH) model, (**b)** Hyperelastic (rubber hardening) model, **(c)** Unloading (Hysteretic) model

In calibrating the model, bounds for the parameters were set in order to ensure convergence and computational efficiency. The initial design values such as the characteristic strength of 980 kN and the post-elastic stiffness of 3,375 kN/m were set as initial values for the calibration process. With regards to the damage model, the degradation parameters $c_1 - c_4$ were set to be positive values given that negative values would produce instabilities and unrealistic effects. Also, Mullins degradation parameter c_3 is bounded between zero to one due to the damage equation for K_M (Equation 4-14). The scragging damage represents the permanent damage, therefore the scragging damage parameter D_S, was retained from the previous loading history (experimental test) resulting in residual damage as demonstrated in Figure 4-3 (Equations 4-12 and 4-13). Note that the experimental tests were conducted with rest times varying from 30 minutes to 24 hours, and therefore the 'short term' damage D_M was set to zero for each test and the scragging damage parameter D_S was retained between for the entire test sequence since this parameter captures the permanent damage. As for the initial lead hardening in the LSLRB model, the parameters for Equation 4-10 result in both c_5 and c_6 being positive values and c_5 set to varying from zero to one.

The minimization of a normalized root mean-squared error (NRMSE) was applied through a multi-objective function considering various experimental tests to account for a wide range of strains and strain rates. The downhill simplex algorithm (Lagarias et al. 1998) was used to find the one set of parameters for all tests considered that minimize the NRMSE.

$$\in = \sum_{i=1}^{no.\,tests} (w_i NRMSE_i) \qquad (4-15)$$

Per Equation 4-15, the $NRMSE_i$ for each test is calculated as the difference of the experimentally measured force and the force resulting from the model normalized by the range of the maximum and minimum forces observed experimentally. All tests in Table 4-1 are considered with equal weights, w_i , when minimizing the multi-objective function. The NRMSE results are also shown and contributions of the model components for test 13 and 15 can be seen in Figure 4-6. The minimization multi-objective error function resulted in the calibration of the parameters shown in Table 4-3.

Table 4-3 LSLRB model calibration of parameters

MODEL	**Parameter Bounds**	**Calibrated Parameters**
Plasticity **(w Lead Heating) model parameters**	$930 \le b_1 \le 1150\ (\boldsymbol{kN})$	1081
	$0 \le b_2 \le 0\ (\boldsymbol{kN/m^2})$	0.00
	$0 \le b_3 \le 500\ (\boldsymbol{m^{-1}})$	288
	$0 \le c_5 \le 1$	0.59
	$0 \le c_6 \le \infty\ (\boldsymbol{m^{-1}})$	8.86
Hyperelastic model parameters	$2950 \le a_1 \le 3800\ (\boldsymbol{kN/m})$	3036
	$-10000 \le a_2 \le 0(\boldsymbol{kN/m^3})$	-3613
	$0 \le a_3 \le 10000\ (\boldsymbol{kN/m^5})$	3635
	$0 \le c_1 \le 100\ (\boldsymbol{m^{-3}})$	0.02
	$0 \le c_3 \le 1$	0.77
	$0 \le c_4 \le 100\ (\boldsymbol{m^{-3}})$	11.30
Unloading (Hysteretic) model parameters	$0 \le b_1 \le 40\ (\boldsymbol{kN})$	8.90
	$0 \le b_2 \le 5000\ (\boldsymbol{kN/m^2})$	2094
	$0 \le b_3 \le 100\ (\boldsymbol{m^{-1}})$	7.35
	$0 \le c_2 \le 100\ (\boldsymbol{m^{-3}})$	0.57

In order to evaluate the LSLRB model and its parameters, a comparison is made with two other widely utilized models for LRBs, a smooth Bouc-Wen bilinear model with constant parameters implemented in OpenSees as the *LeadRubberX* model (without lead heating) hereinafter referred to as a bilinear model, and the *LeadRubberX* model (with lead heating). The calibration for these models were conducted by initially setting the initial values to the preliminary design values including a characteristic strength of 980 kN and post-elastic stiffness of 3,375 kN/m. In contrast to the LSLRB model calibration, the multiobjective NRMSE function for the bilinear model and *LeadRubberX* model consisted of only experimental tests 14 and 11. Tests 14 and 11 correspond to shear strains of 100% and 300% and the weights applied are 0.75 and 0.25, The larger weight is applied to test 14 data with three loading cycles as the characteristic strength is typically obtained as the average over three cycles. Consideration of other test data led to larger discrepancies in the calibrated models as they attempted to capture rubber strain hardening.

4-5 Comparison of LRB models

The calibrated models are compared to the experimental data in Figure 4-5 at 100% and 300% shear strain. Key observations at 100% shear strain are: (i) the bilinear model resulted in the lowest characteristic strength of 867 kN which is the average over the range of cycles, (ii) the *LeadRubberX* characteristic strength is 943 kN then degrades as it cycles, (iii) the LSLRB model results in a strength of 1081 kN with initial hardening followed by degradation due to heating. For all cases, when attempting to calibrate for the final cycle (as the bearing is returning to zero displacement), a clear overestimation of the lead strength is observed. This is likely due to the heating of the lead and the lower strain rates allowing for further reduction in the strength of the lead. For shear strains of 300%, it can be seen that the LSLRB model is able to capture the initial lead hardening and the rubber hardening as well as the pronounced unloading effects resulting in the lowest NRMSE of 2.98% (Figure 4-5f). For 300% shear strain, the bilinear and *LeadRubberX* model are not able to capture the hysteresis from cycle to cycle and at best interpolate between cycles. These figures indicate that for shear strains up to 300%, the proposed model can provide a more accurate representation of LRB behavior.

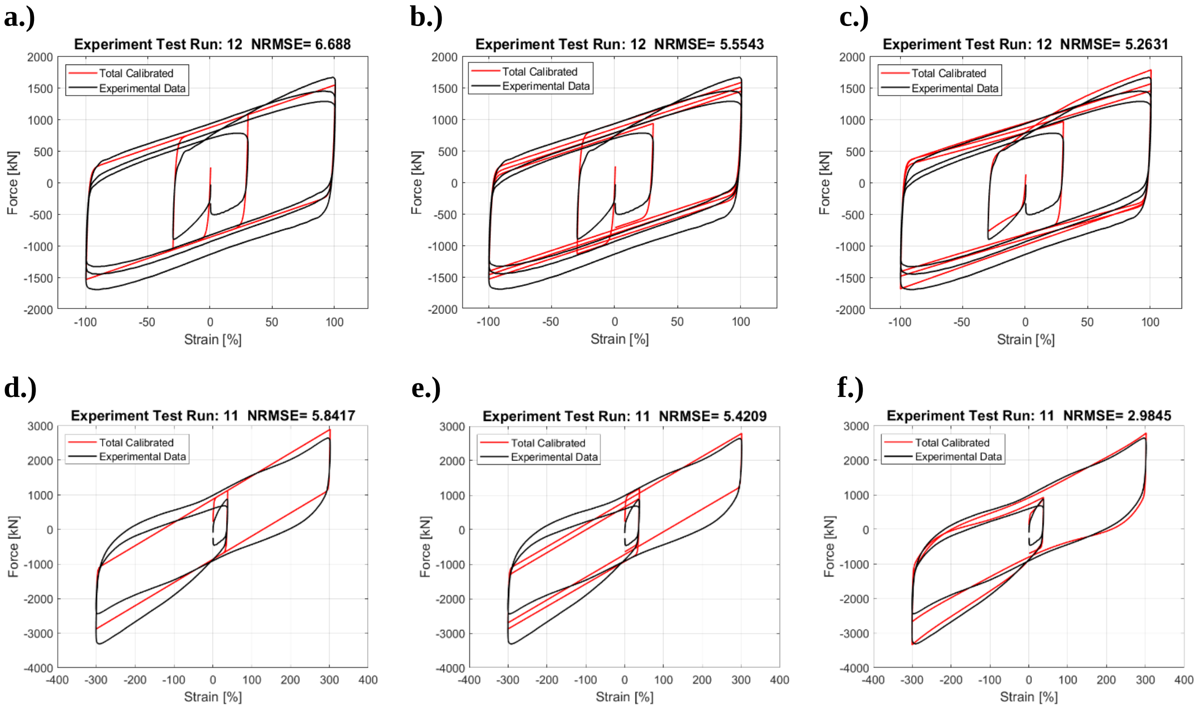

Figure 4-5 Model calibration comparisons to experimental data at various shear strains **a.)** Bilinear (100%) **b.)** *LeadRubberX* (100%) **c.)** LSLRB (100%) **d.)** Bilinear (300%) **e.)** *LeadRubberX* (300%) **f.)** LSLRB (300%)

For the design of seismically isolated structures with LRB, 300% shear strain is near the upper limit considered for maximum allowable design displacement. However, testing of these bearings showed that they can sustain much larger shear strain and this behavior is further examined. A study of a seismically isolated nuclear power plant using an earlier version of this model indicated that the displacement CS could be set around 385% shear strain (An et al. 2020). In Figure 4-6, the total calibrated LSLRB model and the component contributions are shown for test run 13 (400% shear strain). In Figure 4-6a, the hyperelastic model is able to capture the first cycle hardening followed by the associated damage observed in the experimental data. The HDR (unloading) model captures the unloading effects that are observed at these high strain cycles. The LSLRB model with the combination of the lead hardening and lead heating tracks the variation in strength starting with initial lead hardening followed by heat induced strength degradation (Figure 4-6).

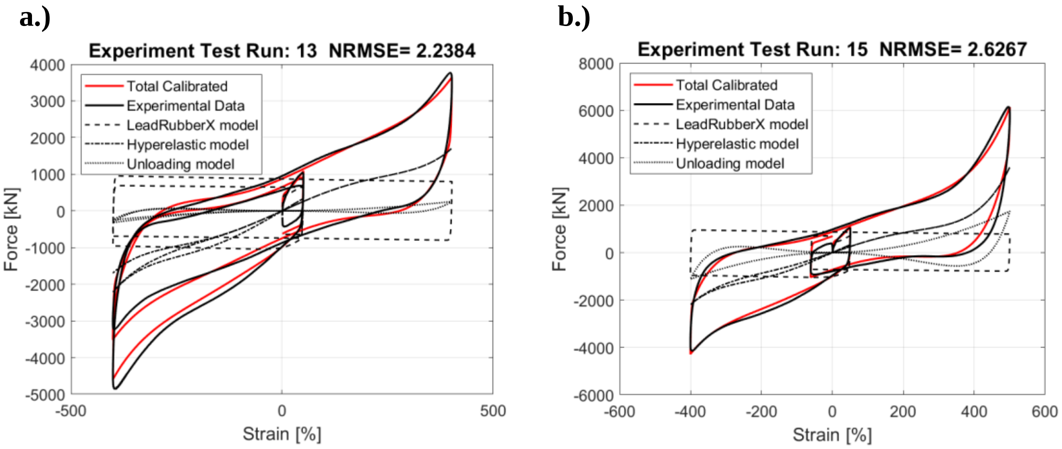

Figure 4-6 Comparison of LSLRB to test data for a.) Test 13 (400% shear strain) b.) Test 15 (500% Shear Strain)

In Table 4-4, the NRMSE are shown for one set of parameters for each of the three models over a wide range of strains. The LSLRB model results in the least error with the NRMSE ranging from 2.24% to 5.38%. The larger NRMSE are observed for low strain tests compared to large strain tests due to the normalization over the range of forces in the NRMSE formulation. For the other models, the calibration utilized tests ranging from 100% to 300% shear strain with higher calibration weight for test 14. The high strain tests are not included in the calibration because the simplified model does not capture any hardening and therefore would result in larger strength values and larger errors in the lower amplitude tests. Overall, the LSLRB model provides better fit for all strain levels. The bilinear model resulted in the highest NRMSE for experiments at 100-300% shear strain as expected for its inability to capture the strength degradation. The *LeadRubberX* model, on the other hand, is able to capture the strength degradation for the low strain tests hence reduced error. The bilinear model has lower errors compared to the heating at larger strains because the lack of strength degradation in the model more closely follow the unloading effect compared to the *LeadRubberX* model.

Table 4-4 NRMSE of various models against unidirectional experimental tests.

Test (#)	**Strain (%)**	**Type**	**NRMSE (%) Bilinear**	**NRMSE (%) *LeadRubberX***	**NRMSE (%) LSLRB**
14	100	sinusoidal	6.69	5.55	5.26
8	200	EQ	9.35	5.76	5.38
11	300	sinusoidal	5.84	5.42	2.98
13	400	sinusoidal	6.08	6.11	2.24
15	500	sinusoidal	6.78	6.96	2.63

4-6 Earthquake Response Analysis

A single degree-of-freedom (SDOF) analysis was conducted to observe the response of the different models under simulated earthquake loading. In the nonlinear response history analysis (NLRHA), maximum displacement and potential impact velocities to moat wall are examined for a given CS. This analysis is conducted in order to examine differences in response prediction when using the three different models: Bilinear, *LeadRubberX* (heating) model and LSLRB model. In the SDOF system, no actual moat wall is considered but the velocity is captured at a given displacement that could be representative of a moat wall CS. The three models only consider the hysteretic damping of the isolation system model utilized without any additional damping. The CS values are considered to evaluate the effects the LSLRB model may have on potential impact velocity compared to other models. Using the models with parameters from previous section, a SDOF system was analyzed under a set of 40 different ground motions (20 ground motion pairs). The ground motions were scaled following the U.S. Nuclear Regulatory Commission Guidelines (USNRC 2014). These ground motions were generated in a previous study as dispersion-appropriate, single-damping spectral-matched for the USNRC target response spectra scaled to a design basis earthquake (DBE) with 0.5g peak ground acceleration (PGA) having a return period of 10,000 years (Schellenberg et al. 2014) . The ground motions were then scaled by a factor of two in order to consider beyond design basis earthquake (BDBE) corresponding to a return period of 100,000 years.

Using the bearing model calibrated from the cyclic test data, a study was conducted to observe the response and variations between the different models considered. The ground motion and displacement time histories are examined for (GM 7: 2002 Denali, Alaska earthquake (Taps pump station #09) scaled to BDBE (Figure 4-7). One key observation is the two pulses induced during the beginning of the ground motion causing two high displacement demand cycles, first in the positive direction and then in the negative direction. At about 5 seconds, when approaching the negative peak, the models seem to deviate likely due to hardening and unloading effects in the LSLRB model (Figure 4-8). The slope of the LSLRB model seems to reduce as a result of a decrease in velocity compared to the other models. After 5 seconds, the LSLRB model continues in a different trajectory especially at peak displacements.

Figure 4-8 shows the hysteretic response of the three models for the same earthquake. The lower displacements for the LSLRB are likely due to the hardening and the unloading effects (Figure 4-8). In addition, the initial lead hardening allows for a higher characteristic strength calibration and therefore more energy dissipation especially for pulse type records with the initial large amplitude cycles prior to significant lead heating.

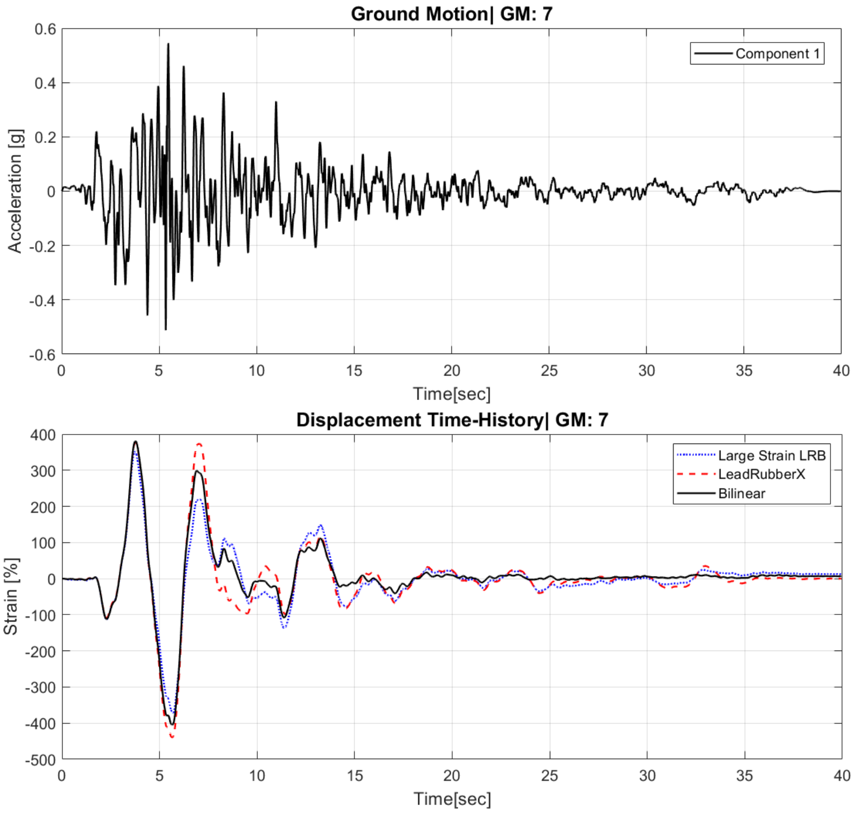

Figure 4-7 BDBE ground motion and displacement time-histories for GM7: 2002 Denali.

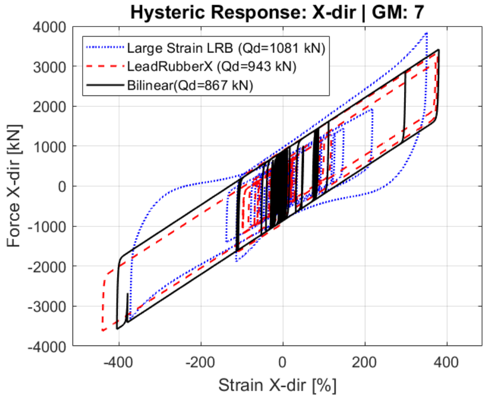

Figure 4-8 Isolator response to single ground motion (GM7: Denali, Alaska (Taps pump station #09))

4-6-1 Maximum Displacement Comparison

In order to gain broader insight into the effects that the LRB models have on the overall system response, the resulting maximum displacements are shown in Figure 4-9 for the three different bearing models: LSLRB model, *LeadRubberX* (heating) model and bilinear model. Following USNRC guidelines for the design of seismically isolated nuclear power plants, the CS or the moat wall distance should be placed at greater than or equal to 90th percentile displacement for BDBE analysis. This ensures that impact to the moat wall is highly unlikely and that if impact does occur the velocity at impact is minimal. A reduction in the CS can be substantiated by analysis considering impact. A lognormal distribution and logarithmic standard deviation were assumed in order to calculate the required displacements (Kumar et al. 2015) to compare the predicted values for the three models.

The response results at the DBE level are first shown in Figure 4-9. In this case, the 99th percentile displacement response is utilized for structural design of the superstructure and to ensure no failure at these displacements. Since this is a single degree of freedom (SDOF), only the isolator displacements are calculated and no superstructure limit states are considered. The LSLRB model resulted in a slightly lower 99th percentile displacement compared to the other two models. This may be due to the initial lead hardening that allowed for a higher characteristic strength. It is important to note that the bilinear model 99th percentile displacement is beyond the range of all predicted displacements due to the assumed lognormal distribution.

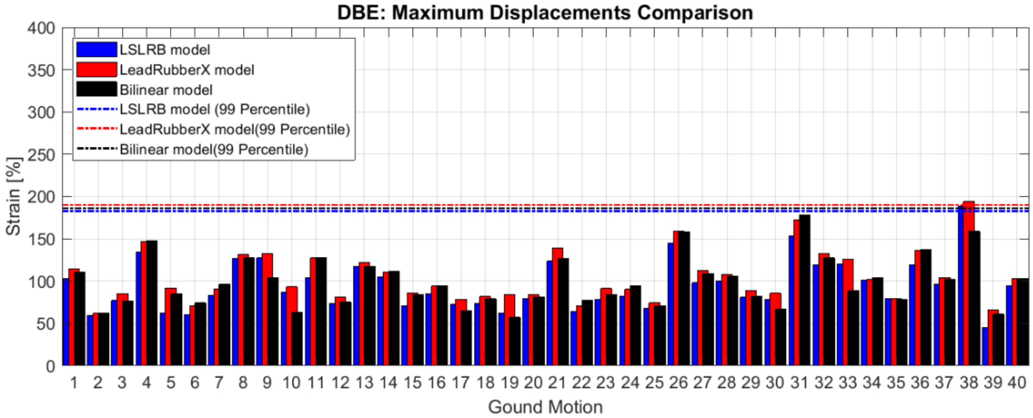

Figure 4-9 DBE GMs: Maximum displacement comparison for each model.

Maximum displacement results for BDBE analysis are shown in Figure 4-10, with the maximum 90 percentile displacements of 485%, 667%, and 452% shear strain for the LSLRB, *LeadRubberX*, and the Bilinear model, respectively. The *LeadRubberX* model's average displacement overestimates the LSLRB model by approximately 38% when considering all records (Figure 4-10). The maximum displacements for ground motions 9, 10, 18, and 19 can be considered statistical outliers, particularly for the *LeadRubbberX* model. Ground motion pairs GMs ([19 39] and [18 38]) can be classified as long duration ground motions since the significant duration, Ds_{5-75} (i.e. the time interval over which 5% to 75% of the integral of the ground acceleration squared is accumulated), is above 25 seconds (Chandramohan et al. 2016). It has been demonstrated in Chapter 3 of this dissertation, that long duration ground motions can result in larger displacements for the *LeadRubberX* model due to significant heating in comparison to a bilinear model. The experimental test program did not include long duration cyclic motions to further verify the models under these conditions, however comparing the statistical analysis without these long duration ground motions may be insightful. When excluding long duration ground motions pairs (i.e. [18 28, 19 38]), the maximum 90 percentile displacements result in 473%, 634%, and 454% for the LSLRB, *LeadRubberX*, and the Bilinear model, respectively. Significant reductions in the maximum 90 percentile displacements can be observed for both models considering heating and more pronounced for the LeadRubberX model that does not account for rubber hardening. These ground motions provide important insight that should be further investigated. First, consideration of heating effects is critical for predicting bearing displacements for long duration ground motions. Second, when comparing displacements for the three models, the LSLRB model tends to compensate for the lead heating with the engagement of rubber hardening at large strains, resulting in significantly lower displacements than the

LeadRubberX model and larger displacements compared to the bilinear model. For BDBE level shaking it is essential to capture the different nonlinearities observed in experimental data. The bilinear model is able to interpolate the heating and hardening effects of the LSLRB and resulted in similar 90th percentile displacements as shown in the Figure 4-10. However, the record-to-record variability is high when comparing LSLRB and the bilinear model.

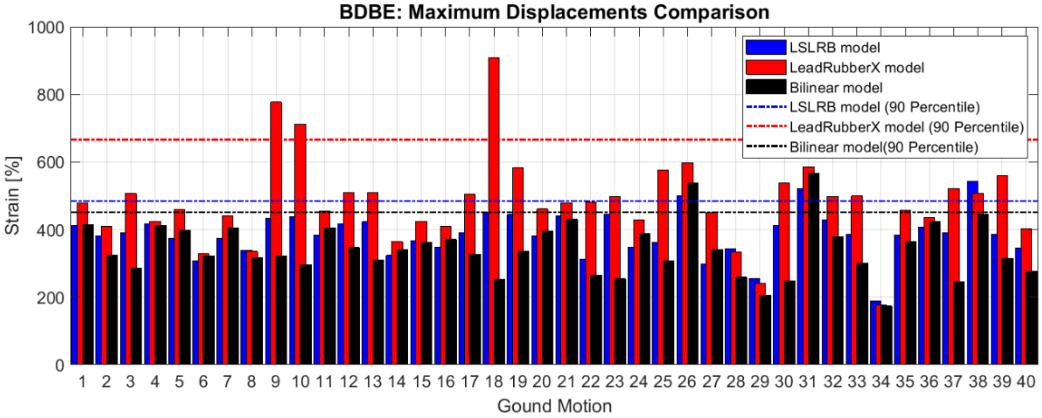

Figure 4-10 BDBE GMs: Maximum displacement comparison for each model.

4-6-2 Considerations for Moat Wall Impact Velocity

The potential impact velocity at a given distance is evaluated since it has been demonstrated that severitiy of impact is highly dependent on this parameter (Masroor and Mosqueda 2013). Results for impact velocity are examined for the SDOF system with the three different models. An actual moat wall was not implemented, rather, a wall clearance was assumed at different displacements, then the relative velocity between the ground and superstructure was calculated at that distance. The purpose of this analysis was to observe any effects the different models would have on the impact velocity or the severity of impact by considering the moat wall at different distances for CS. Due to the fact that the first impact could affect the second impact from rebound effects, only the first impact velocity was analyzed. Impact is not expected for DBE level GMs therefore only BDBE are presented.

The average impact velocities along with the standard deviations indicated at each CS in increments of 25% shear strain are provided in Figure 4-11. The LSLRB model and the Bilinear model tend to have reduced average and standard deviation at large strains (>350%). The *LeadRubberX* model gives larger impact velocities for the LRB especially at high strains, while the bilinear model tends to underestimate the impact velocities within the 'medium to high' strains (i.e. 275-375%). The *LeadRubberX* model has the highest impact velocities for all CS cases, except for CS 250% shear strain. More importantly, the LSLRB model obtained similar average impact velocities compared to the *LeadRubberX* model and bilinear model at lower strains (i.e. 200-250% shear strain), for which all three models have very similar in characteristics and begin to deviate at larger strains.

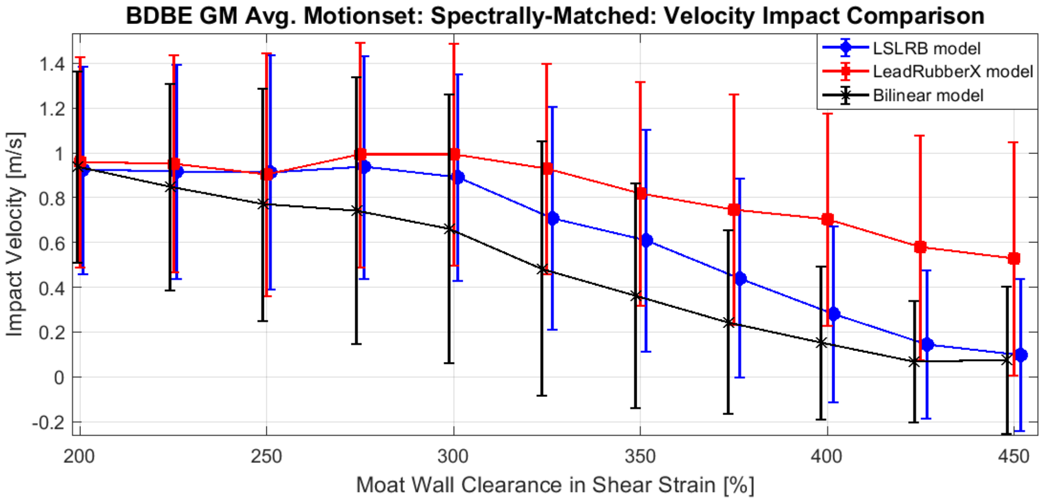

Figure 4-11 Comparison of BDBE Impact Velocity vs Moat Wall Clearance for different models.

At 275% shear strain, the LSLRB model begins to diverge from the *LeadRubberX* model and approaches the bilinear model velocity predictions as the hardening and unloading effects of the LSLRB model engage at these large strains. Hardening at large strains is beneficial for reducing displacements and lowering the impact velocities. A similar stiffening effect is demonstrated by triple friction pendulum bearings at large displacements (Fenz and Constantinou 2008). Future studies are needed to observe the effects the LSLRB model may have on the superstructure.

The variation of impact velocities for the three different bearing models subjected to the 2002 Denali record is shown in Figure 4-12. The displacement time history in Figure 4-7 demonstrated the near-fault pulse response for this motion. For this particular motion, significant reductions in impact velocities is observed for LSLRB model at shear strains above 300%. When comparing the models, the trends shown here are different from Figure 4-11. The simulated impacts for CS of 200-325% shear strain for the three models occurred at the first cycle in the positive direction within seconds of the ground motion prior to significant lead core heating. The reduction in impact velocity of the LSLRB model is likely due to the calibration of the higher characteristic strength. For CS of 325% and 350%, all three models impact in the positive direction. In addition to the LSLRB model's higher characteristic strength, the rubber hardening effects further reduce impact velocities. The larger the strain the more pronounced the hardening and unloading effects are, which result in larger reductions in impact velocity for cases greater than 325% shear strain where the hardening is engaged in the LSLRB model. For example, at 325% shear strain the impact velocities for the three models were 0.86, 1.21, and 1.29 m/s, for the LSLRB, *LeadRubberX*, and bilinear model, respectively. This significant decrease in velocity of the LSLRB model is noteworthy and confirms the benefits of capturing the large strain behavior of the rubber. Furthermore, at 375% shear strain and higher, no impact was observed for the LSLRB model.

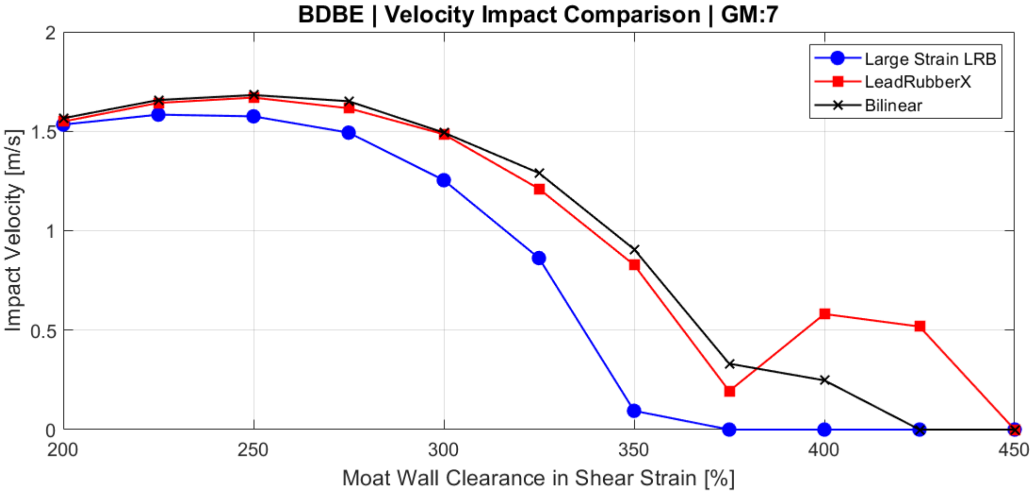

Figure 4-12 Impact Velocity vs Moat Wall Clearance (GM 7: Denali, Alaska, Taps Pump Station #09)

To further investigate the record-to-record variability of the three models, the impact velocities at a CS of 350% shear strain are shown in Figure 4-13. The resulting mean and standard deviation for each model (including no impacts) are *LeadRubberX* (0.837,0.514), Bilinear (0.392,0.513), and the LSLRB (0.580,0.498). The models demonstrate large variations in velocity at 350% shear strain, with the bilinear model providing the lowest average velocity by not accounting for strength degradation and use of this model should be carefully considered.

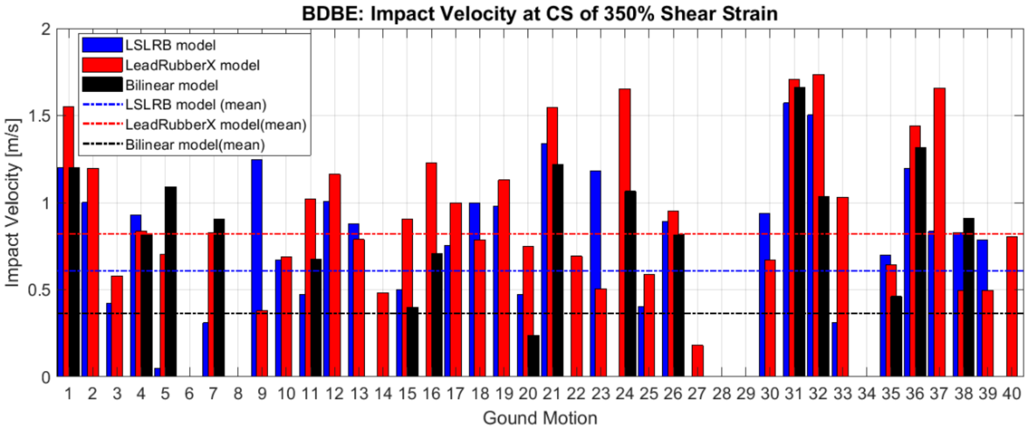

Figure 4-13 Record-to-record variability for impact velocities at CS 350% shear strain

4-7 Conclusion

Models for elastomeric bearings are reviewed then utilized in parallel in order to capture key characteristic behaviors that are observed experimentally in LRB. The parallel system named LSLRB model, can capture experimentally observed behaviors such as lead strength degradation, initial lead hardening, rubber hardening, and unloading effects. The model is a combination of the *LeadRubberX* model, hyperelastic (hardening) model, and the unloading model. The model utilizes one set of parameters to capture the various nonlinear behaviors at various strain levels only considering a constant axial load, therefore the size of the bearing and variance in the axial load will require recalibration of the LSLRB model. The LSLRB model calibrated to measured bearing behavior was utilized in analysis of a SDOF nonlinear time history analysis to examine the unloading and rubber hardening effects may have on the system response compared to a bilinear model and the recently developed *LeadRubberX* model. In this study it was found that the velocity at first impact under different clearance to stops (CS) above 250% shear strain resulted in the LSLRB model essentially bounded by the *LeadRubberX* model and the bilinear model for BDBE, however large variations in impact velocities are observed at 350% shear strain, with the bilinear model providing the lowest average velocity by not accounting for strength degradation and use of this model should be carefully considered. When comparing the maximum displacements of 90th percentile BDBE for all three models, the Bilinear model and LSLRB model resulted in similar 90th percentile maximum displacement for BDBE comparatively to the *LeadRubberX* model. For BDBE, it is important to note that the *LeadRubberX* model highly overestimates the impact velocities and peak displacements compared to the LSLRB model, while the bilinear model tends to obtain similar displacements to the LSLRB model, the impact velocities are highly underestimated. In considering these results, it is important to note the proposed LSLRB model begins to show notable difference in response prediction at shear strains greater than 250%, particularly for impact velocities. In current practice, bearing displacements are limited around this range of strain for design consideration. Extending the range of strain by verifying bearing performance through experimental testing can significantly reduce impact velocities and minimize damage to the superstructures in the case of a rare earthquake. Additional studies will be conducted to examine the effects of bearing models on the superstructure response as well as the contribution of vertical loads on bearing behavior.

Chapter 4, in part, are a reprint of the material as it appears in “Modeling of Lead Rubber Bearings Under Large Cyclic Material Strains.” Marquez, J.F., Mosqueda, G., & Kim, M.K., *ASCE Journal of Structural Engineering (2021).* The dissertation author was the primary investigator and author of this paper.

4-8 Reference

An, G., Kim, M., Jung, J.-W., Mosqueda, G., and Marquez, J. F. (2020). “Evaluation of Clearance to Stop Requirements in A Seismically Isolated Nuclear Power Plant.” *Energies,* 13(22), 6156.

Aramaki, S., Uno, K., and Noyori, K. (2004). “Study of Lead Pillar Damper for the Earthquake Resistance Reinforcement of an Established Road Bridge.” *Proc. of the 13th World Conference on Earthquake Engineering. Paper No. 364, Mira Digital Publishing,St. Louis, MO.,* Vancouver, B.C., Canada.

Chandramohan, R., Baker, J. W., and Deierlein, G. G. (2016). “Quantifying the influence of ground motion duration on structural collapse capacity using spectrally equivalent records.” *Earthquake Spectra*, 32(2), 927–950.

Civil Engineering Research Foundation. (1998). *Evaluation findings for Skellerup base isolation elastromeric bearings*. Rep. No., HITEC 98-11 40376, Washington D.C.

Clark, P. W., Aiken, I. D., and Kelly, J. M. (1997). *Experimental studies of the ultimate behavior of seismically-isolated structures. Technical Report EERC-97-l8, Earthquake Engineering Research Center*, Berkeley, CA.

Dafalias, Y. F., and Popov, E. P. (1975). “A model of nonlinearly hardening materials for complex loading.” *Acta Mechanica*, 21(3), 173–192.

Dall’Asta, A., and Ragni, L. (2008). “Nonlinear behavior of dynamic systems with high damping rubber devices.” *Engineering Structures*, Elsevier Ltd, 30(12), 3610–3618.

Diani, J., Fayolle, B., and Gilormini, P. (2009). “A review on the Mullins effect.” *European Polymer Journal*, Elsevier Ltd, 45(3), 601–612.

Eem, S., and Hahm, D. (2019). “Large strain nonlinear model of lead rubber bearings for beyond design basis earthquakes.” *Nuclear Engineering and Technology*, 51(2), 600–606.

Fenz, D. M., and Constantinou, M. C. (2008). “Spherical sliding isolation bearings with adaptive behavior: Theory.” *Earthquake Engineering & Structural Dynamics*, 37(2), 163–183.

Grant, D. N., Fenves, G. L., and Whittaker, A. S. (2004). “Bidirectional Modelling of High-Damping Rubber Bearings.” *Journal of Earthquake Engineering*, 8(1), 161–185.

Ishida, K., Shiojiri, H., Iizuka, M., Mizukoshi, K., and Takabayashi, K. (1991). “Failure Tests of Laminated Rubber Bearings.” *Proceedings of the 11th international conference on* *structural mechanics in reactor technology*, IASMiRT, Tokyo,Japan, 241–246.

Ishii, K., and Kikuchi, M. (2019). "Improved numerical analysis for ultimate behavior of elastomeric seismic isolation bearings." *Earthquake Engineering and Structural Dynamics*, 48(1), 65–77.

Kalpakidis, I., and Constatinou, M. (2008). *Effects of heating and load history on the behavior of lead-rubber bearings*. *Technical Rep.No. MCEER-08-0027,* Multidisciplinary Center for Earthquake Engineering Research, Buffalo, N.Y.

Kalpakidis, I. V., and Constantinou, M. C. (2009a). "Effects of Heating on the Behavior of Lead-Rubber Bearings. II: Verification of Theory." *Journal of Structural Engineering*, 135(12), 1450–1461.

Kalpakidis, I. V., and Constantinou, M. C. (2009b). "Effects of Heating on the Behavior of Lead-Rubber Bearings. I: Theory." *Journal of Structural Engineering*, 135(12), 1440–1449.

Kikuchi, M., and Aiken, I. D. (1997). "An analytical hysteresis model for elastomeric seismic isolation bearings." *Earthquake Engineering and Structural Dynamics*, 26(2), 215–231.

Kikuchi, M., Nakamura, T., and Aiken, I. D. (2010). "Three-dimensional analysis for square seismic isolation bearings under large shear deformations and high axial loads." *Earthquake Engineering & Structural Dynamics*, 39(13), 1513–1531.

Kim, J. H., Kim, M. K., and Choi, I.-K. (2019). "Experimental study on seismic behavior of lead-rubber bearing considering bi-directional horizontal input motions." *Engineering Structures*, 198.

Kim, J. H., Kim, M. K., and Choi, I. (2017). "Experimental Study on the Bidirectional Behavior of a Lead-Rubber Bearing." *Proceedings of the 16th World Conference on Earthquake Engineering*, 16WCEE 2017, Santiago, Chile.

Kitayama, S., and Constantinou, M. C. (2021). "Implications of strong earthquake ground motion duration on the response and testing of seismic isolation systems." *Earthquake Engineering and Structural Dynamics*.

Koh, C. G., and Kelly, J. M. (1988). "A simple mechanical model for elastomeric bearings used in base isolation." *International Journal of Mechanical Sciences*, 30(12), 933–943.

Kumar, M., Whittaker, A. S., and Constantinou, M. C. (2014). "An advanced numerical model of elastomeric seismic isolation bearings." *Earthquake Engineering & Structural Dynamics*, 43(13), 1955–1974.

Kumar, M., Whittaker, A. S., and Constantinou, M. C. (2015). *Seismic isolation of nuclear power plants using elastomeric bearings. Technical Report MCEER-15-0006.*

Lagarias, J. C., Reeds, J. A., Wright, M. H., and Wright, P. E. (1998). "Convergence properties of the Nelder-Mead simplex method in low dimensions." *SIAM Journal on Optimization*, 9(1), 112–147.

Masroor, A., and Mosqueda, G. (2013). "Impact model for simulation of base isolated buildings impacting flexible moat walls." *Earthquake Engineering and Structural Dynamics*, 42(3), 357–376.

McVitty, W. J., and Constantinou, M. C. (2015). "Property modification factors for seismic isolators: Design guidance for buildings." *MCEER Report*, 15–0005.

Mullins, L. (1969). "Softening of Rubber by Deformation." *Rubber Chemistry and Technology*, 42(1), 339–362.

Oliveto, N. D., Markou, A. A., and Athanasiou, A. (2019). "Modeling of high damping rubber bearings under bidirectional shear loading." *Soil Dynamics and Earthquake Engineering*, Elsevier Ltd, 118, 179–190.

OpenSees. (2014). "Open system for earthquake engineering (Version 2.4.4)."

Ryan, K. L., Kelly, J. M., and Chopra, A. K. (2005). "Nonlinear Model for Lead–Rubber Bearings Including Axial-Load Effects." *Journal of Engineering Mechanics*, 131(12), 1270–1278.

Sanchez, J., Masroor, A., Mosqueda, G., and Ryan, K. (2013). "Static and dynamic stability of elastomeric bearings for seismic protection of structures." *Journal of Structural Engineering (United States)*, 139(7), 1149–1159.

Sarebanha, A., H. Schellenberg, R., J. Schoettler, M., Mosqueda, G., and A. Mahin, S. (2019). "Real-Time Hybrid Simulation of Seismically Isolated Structures with Full-Scale Bearings and Large Computational Models." *Computer Modeling in Engineering & Sciences*, 120(3), 693–717.

Schellenberg, A., Baker, J., Mahin, S., and Sitar, N. (2014). *Investigation of Seismic Isolation Technology Applied to the APR 1400 Nuclear Power Plant-Volume 2: Selection of Ground Motions. Technical Report to KEPCO Engineering and Construction, Pacific Engineering Research Center, University of California, Berkeley, CA.*

Sheridan, P. M., James, F. O., and Miller, T. S. (2012). "Design of Components." *Engineering with Rubber*, A. N. Gent, ed., Carl Hanser Verlag GmbH & Co. KG, München, 259–

293.

Tyler, R. G., and Robinson, W. H. (1984). “High-Strain Tests on Lead-Rubber Bearings for Earthquake Loadings.” *Earthquake Engineering*, 17(2), 90–105.

U.S. Nuclear Regulatory Commission. (2014). “Design Response Spectra for Seismic Design of Nuclear Power Plants.” *Regulatory Guide No. 1.60, Revision 2*.

Vemuru, V. S. M., Nagarajaiah, S., and Mosqueda, G. (2016). “Coupled horizontal-vertical stability of bearings under dynamic loading.” *Earthquake Engineering and Structural Dynamics*, 45(6), 913–934.

Warn, G. P., Whittaker, A. S., and Constantinou, M. C. (2007). “Vertical Stiffness of Elastomeric and Lead–Rubber Seismic Isolation Bearings.” *Journal of Structural Engineering*, 133(9), 1227–1236.

Chapter 5 SUPERSTRUCTURE RESPONSE WITH LSLRB MODEL

5-1 Introduction

The seismic response of a full-scale Nuclear Power Plant (NPP) model is examined with the implementation of the large strain lead rubber bearing (LSLRB) model proposed in Chapter 4. NPPs are critical infrastructures designed to stringent safety criteria for seismic design and require analysis under Beyond Design Basis Earthquake (BDBE) shaking (ASCE 2017a) to verify their response for low-frequency high-risk event. Bearings are required to be tested to verify they can achieve the maximum displacements obtained from the BDBE analysis under the expected axial load.

Previous experimental studies on moat wall impact have found that velocity of impact is a key parameter for the impact force and the amplification of structure response (Fukui et al. 2020; Masroor and Mosqueda 2012). Estimation of the impact velocity is thus critical for analysis considering moat wall impact. ASCE 4 (2017) requires explicit analysis of the isolated structure system for impact loading if the provided clearance is less than the required clearance to stop (CS) with little guidance provided for procedures to model or mitigate the effects of impact.

Modeling of the seismic isolation system plays a key role in simulating the seismic response of NPPs subjected to ground shaking, including prediction of maximum isolation system displacements and velocity in case of exceeding the CS. The United States Nuclear Regulatory Commission (USNRC 2014) provides requirements for the modeling of the seismic isolation system, requiring that the model shall accurately capture the expected horizontal force-deformation relationship at the amplitude from zero to the CS. Therefore, accurately modeling the various nonlinear behaviors at low to high levels of strain are critical as described in Chapter 4. The parallel LSLRB model proposed from Chapter 4 is compared with other widely used LRB models. The LSLRB model consists of the *LeadRubberX* model (Kalpakidis and Constantinou 2009b; Kumar et al. 2014) and components of the HDR model (Grant et al. 2004). The LSLRB model is able to capture initial lead core hardening and the lead core strength degradation due to heating, in addition to, rubber hardening and softening effects at large strains. The benefits of using the LSLRB model is demonstrated in terms of estimating isolator displacements and capturing the impact velocity as the isolation system exceeds the CS as well as the consequences of impact on the superstructure.

5-2 Model of Nuclear Power Plant

NPPs are considered critical infrastructures designed to stringent safety criteria for daily operation as well as for the consideration of different hazards including seismic loading. For the seismic analysis of NPPs, simplified stick models to detailed finite elements models have been developed to examine the response of these structure under different loading conditions. For these studies examining the effect of impact, the Archetype Nuclear Test (ANT) model based on the APR 1400 NPP was used for the superstructure (Schellenberg et al. 2016). As shown in Figure 5-1, the superstructure is considered as a stick model while the base mat and isolation system are modeled in detail to capture the response of the seismic isolation system and base mat impact to a moat wall. The base mat has overall plan dimensions of 103.6 m x 102.4 m with a thickness of 5 m and modeled using SSPbrick element in OpenSees to capture the local response of the base mat and the seismic isolation system during impact. The three bearing models considered are: the Bouc-Wen model (Bouc 1971; Wen 1976), the *LeadRubberX* model (Kumar et al. 2014) and the LSLRB model. A moat wall model is added as a macro element that considers impact behavior, the dynamic response of the retaining wall, and backfill soil (Sarebanha et al. 2018b).

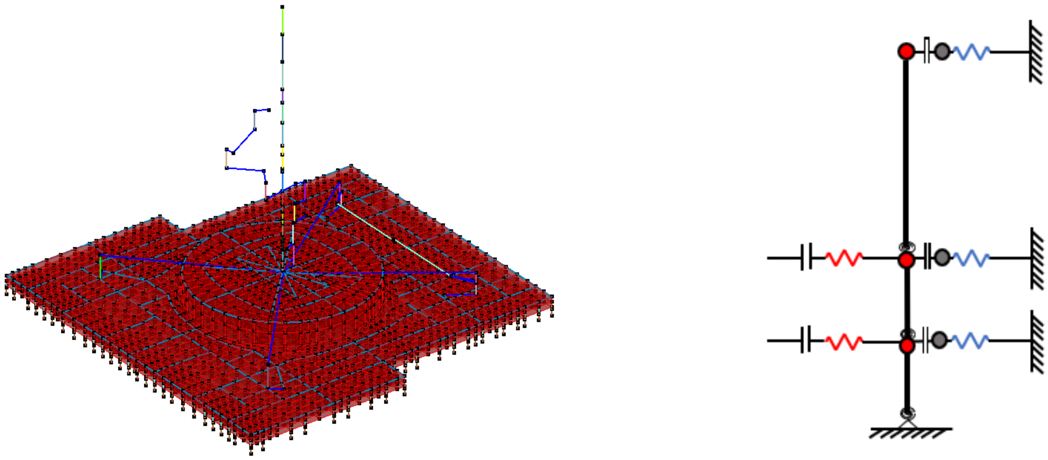

(a) (b)

Figure 5-1 a) ANT model in OpenSees, b) Moat wall macro element to represent surrounding moat wall (Sarebanha et al. 2018b)

The concrete retaining wall portion of the moat wall system (Figure 5-1b) was modeled with elastic beam elements and nonlinear rotational springs to capture the response of plastic hinges along the height of the wall. Backfill soil was also considered in the modeling of the moat wall using the hyperbolic force displacement model developed by Duncan and Mokwa (2001) and Shamsabadi et al. (2007). In order to correctly obtain the maximum stiffness and ultimate force of the backfill soil, extrapolation of data from experimental work by Wilson (2009) was utilized. The Hertz model was utilized (Goldsmith and Frasier 1961) for the modeling of the impact interface during structural impact. The *ImpactMaterial* based on an approximation to the Hertz damped model proposed by DesRoches and Muthukumar (2002) was used in order to implement in OpenSees. More recent findings, have shown that the impact material utilized for analysis does not affect the overall global response of the system (Hughes and Mosqueda 2020).

5-3 Effects of Bearings Models on NPP response

In this section, the effects of bearing model selection on the seismic response of the NPP are examined to understand the potential mitigation efforts in reducing maximum displacements and impact velocities. Different bearing models were implemented in the APR 1400 ANT model to conduct simulations, namely the smooth bilinear Bouc-Wen, the *LeadRubberX* and the LSLRB model (See Chapter 4 for bearing model parameters and calibration). The studies here are conducted for one horizontal component of excitation due to the one-dimensional (1D) limitation of the LSLRB model. A nonlinear response history analysis (NLRHA) is conducted utilizing a set of 20 ground motions at BDBE having a return period of 100,000 years (Schellenberg et al. 2014). The maximum displacements, number of total impacts, and impact velocities at selected CS values are compared. Various CS values are examined in order to observe any potential benefits in the nonlinear behaviors captured in the LSLRB model when allowed to reach different levels of strain. The CS is considered in terms of bearing shear strain considered in the range of 325-375% to better relate to the expected amount of rubber hardening. A previous study conducted using a similar model and bearings and seismic hazard proposed a CS in the same range as the values considered here (An et al. 2020).

5-3-1 Selection of Bearing Models

The NLRHA of the NPP with the LSLRB, the Bouc-Wen and *LeadRubberX* model are conducted to compare the differences between each model. The displacement time history is shown for all models for the Denali, Alaska (Taps pump station #09) ground motion 7 record (GM7) (Figure 5-2). As observed in Chapter 4, the ground motion tends to have two pulses initially in the positive and then in the negative direction having a near-fault type characteristic. The LSLRB model obtained lower displacements compared to the Bouc-Wen and *LeadRubberX* model, demonstrating the effectiveness of the model in reducing displacements for these types of ground motions.

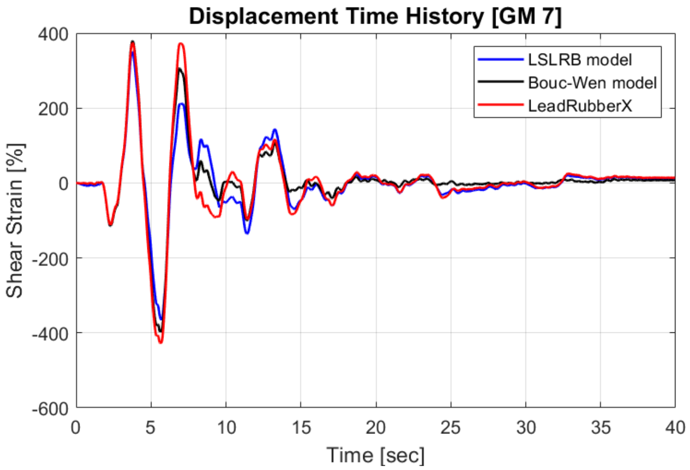

Figure 5-2 Isolator model displacement time-history comparison for single ground motion (GM7: Denali, Alaska (Taps pump station #09)

The hysteresis for each model is compared in Figure 5-3. The LSLRB model tends to reduce the displacements compared to the other models. One factor for this reduction is likely due to the LSLRB model more accurately capturing the characteristic strength. Additionally, the

LSLRB model is able to capture the hardening and softening effects producing widening of the hysteresis and therefore dissipating more energy. The widening of the hysteresis, due to the nonlinear effects, tend to reduce the displacement at the negative shear strains compared to the Bouc-Wen and *LeadRubberX* model. Furthermore, the Bouc-Wen and *LeadRubberX* model undergo larger displacements in the negative direction compared to the positive direction, while the LSLRB model tends to obtain the same displacement magnitude as in the positive direction. When comparing the third cycle displacements in the positive direction among the three models (Figure 5-2), the LSLRB model shows further reductions in displacements due to the aforementioned behaviors.

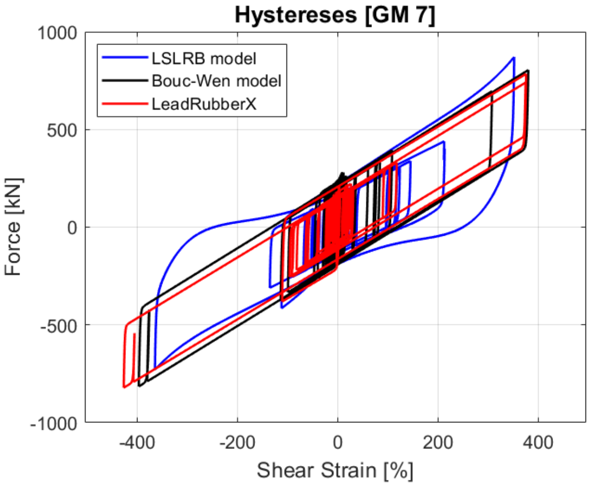

Figure 5-3 Isolator response to single ground motion (GM7: Denali, Alaska (Taps pump station #09)

In order to clearly observe the variation of the maximum displacements for the three LRB models, the moat wall was not considered in the following analysis. The resulting peak displacements are shown in Figure 5-4. The USNRC guidelines (Kammerer et al. 2019) specify that the moat wall should be placed at the 90th percentile displacement assuming a lognormal distribution of peak displacements resulting from the considered set of ground motions at BDBE. The NLRHA indicate that the CS should be placed at 406%, 430%, and 610% bearing shear strain for the Bouc-Wen, LSLRB, and *LeadRubberX* model, respectively. The *LeadRubberX* model results in the largest CS estimates due to the strength degradation of the model causing reduced energy dissipation resulting in a 42% percent increase in maximum displacements when compared to the LSLRB model. The Bouc-Wen model resulted in the lowest displacements of the three models however the LSLRB model, at some instances, further reduced displacements compared to the Bouc-Wen model (i.e. GMs 1,5,6,7,11,14,16,20). This demonstrates that the LSLRB model is capable of mitigating the effects of the lead core heating by compensating with the rubber hardening effects. Importantly, the model selection could have a significant effect on peak displacement estimates and potentially placing the CS at larger distances than required. For example, considering the *LeadRubberX* model will highly overestimate the moat wall placement when compared to the LSLRB model, requiring a redesign of the isolation system due to the excessive displacement demands.

Although the Bouc-Wen and LSLRB model attained similar 90th percentile displacements, apparent record-to-record variability is observed between the two models. The maximum displacements for ground motions 9, 10, 18, and 19 can be considered statistical outliers. For ground motions 9 and 10, since the ground motions were synthetically created, these particular ground motions contained pulse-like demand towards the end of the record and are considered non-realistic as mentioned in Schellenberg et al. (2014). As for ground motions 18 and 19, they can be classified as long duration ground motions since the significant duration, Ds_{5-75} (i.e. the time interval over which 5% to 75% of the integral of the ground acceleration squared is accumulated), is above 25 seconds (Chandramohan et al. 2016). Particularly for the *LeadRubberX* model, the largest displacements corresponded to longer duration shaking and subsequently more strength degradation resulting in larger displacements when compared to a bilinear model (more in Chapter 4). The experimental test program did not include long duration cyclic motions to further verify the models under these conditions, however comparing the statistical analysis without these long duration ground motions may be insightful. When excluding long duration ground motions 18 and 19, the maximum 90th percentile displacements result in 406%, 420%, and 581% for the Bilinear, LSLRB, and the *LeadRubberX* model, respectively. Significant reductions in the 90th percentile displacements can be observed for both the LSLRB and *LeadRubberX* model when compared to including all ground motions. Importantly, although both models consider heating, more significant reductions are observed for the *LeadRubberX* model in which rubber hardening is not included. These ground motions provide important insight that should be further investigated. First, consideration of the lead core heating effects is crucial for predicting bearing displacements for long duration ground motions. Secondly, when comparing the maximum displacements for the three models, the LSLRB model tends to compensate for the lead core heating when rubber hardening and softening effects are accounted for at large strains. When considering BDBE level shaking, it is essential to model the various nonlinear behaviors observed in experimental data.

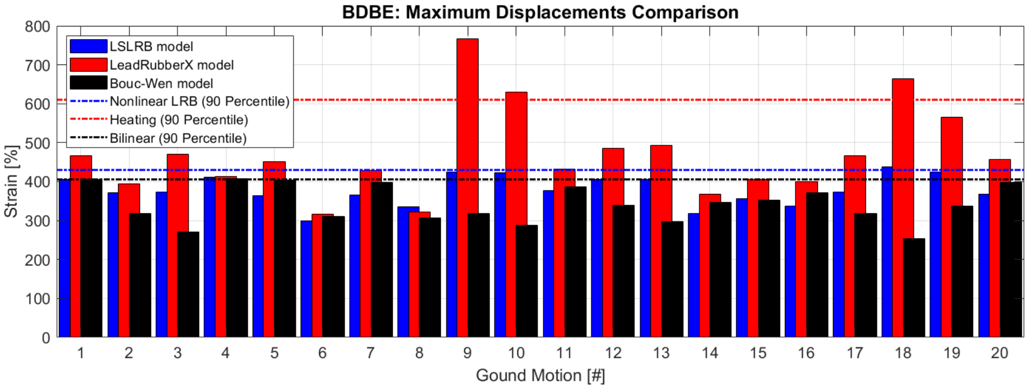

Figure 5-4 Maximum displacements for LRB models

5-3-2 Response of the Superstructure

The average pseudo response spectra along the height of the reactor containment building (RCB) of the NPP are computed for the BDBE ground motions without a moat wall to focus on the effects of the three bearing models on the superstructure response (Figure 5-5). There are two distinct peaks at frequencies 0.3hz and 3.5hz, representing the isolation system fundamental frequency and the fundamental frequency of the Reactor Containment Building (RCB), respectively. A notable result here is that the hardening effects of the LSLRB model do not amplify the spectral accelerations at dominant peak of 3.5hz as may be expected for a hardening system. On the contrary, it tends to dampen the higher frequencies 8 hz and higher for all heights of the structure.

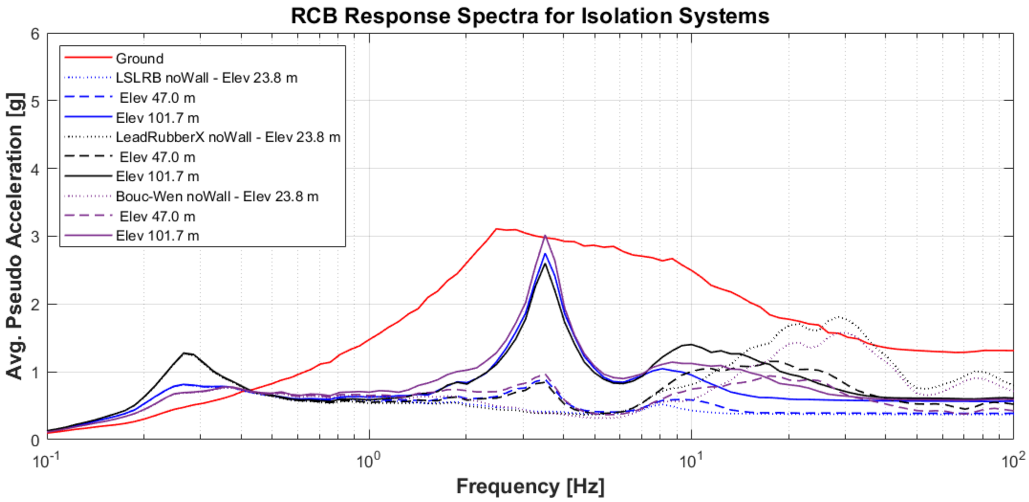

Figure 5-5 Average floor response spectra of RCB for 20 GMs with no moat wall.

The average pseudo response spectra for all three LRB models with a moat wall at three various clearances to stops (CS) 325, 350, and 375% shear strain are shown in Figure 5-6. Similarly, the two distinct peaks at frequencies of 0.3hz and 3.5hz are present with the second peak increasing in amplitude for all CS compared to the no moat wall case, likely due to impact amplification.

However, for the LSLRB model, there is a significant reduction in the average pseudo acceleration from 5.2g to 3.3g by increasing the clearance to stop from 325% to 375% shear strain. The other two models show negligible reductions in average pseudo accelerations with a decrease from 5.6g to 5g for *LeadRubberX* model and a decrease from 4.3 to 3.3g for the Bouc-Wen model. These results indicate that extending the CS or potentially engaging the hardening earlier may be beneficial for lowering impact velocities and consequently reducing accelerations in content within the superstructure.

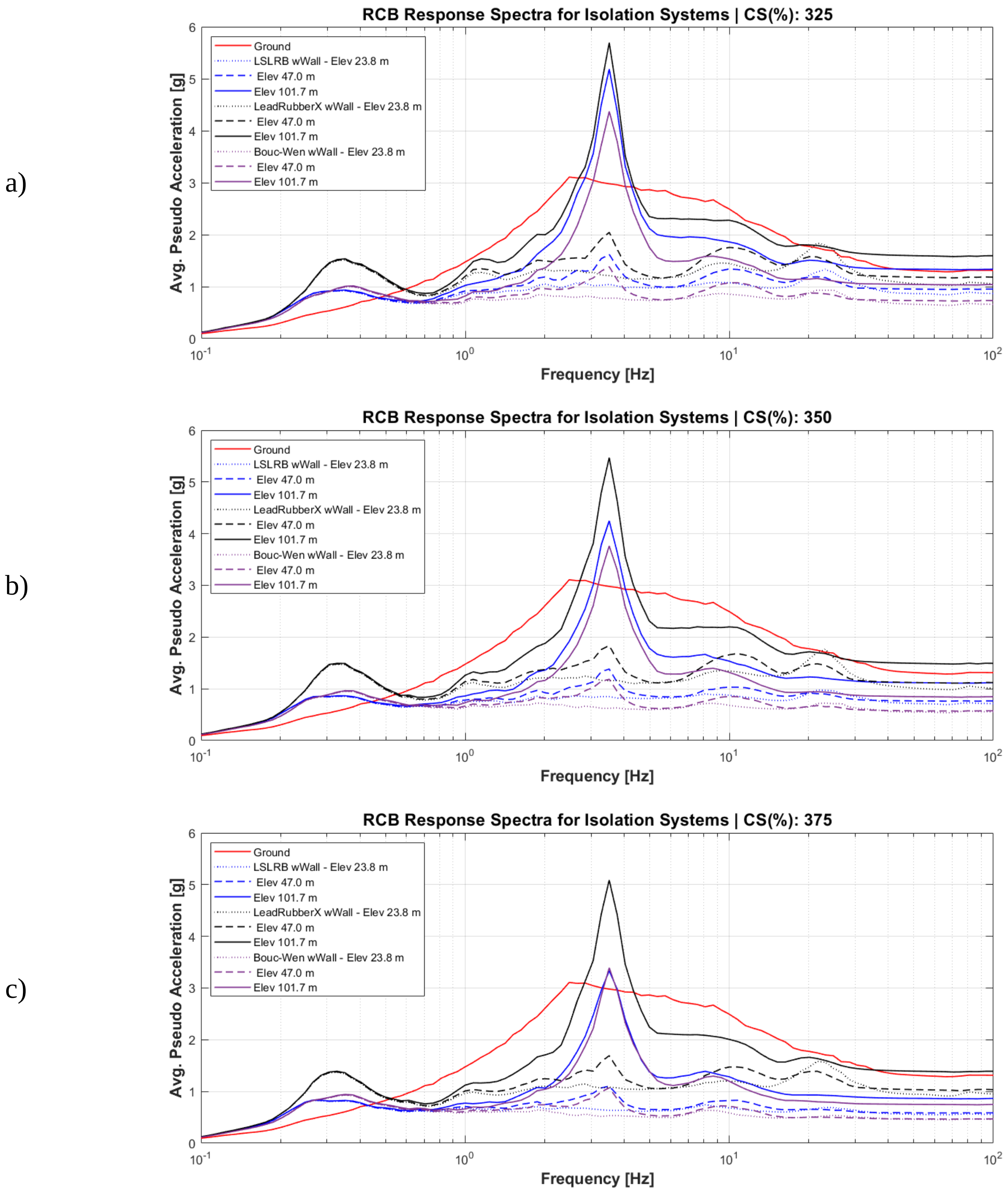

Figure 5-6 Average floor response spectra of RCB for 20 GMs with moat wall clearance set at: a) 325% shear strain, b) 350% shear strain, and c) 375% shear strain

5-3-3 Moat wall impact

Considering the NPP model with moat walls placed at three different distances of 325%, 350%, and 375% shear strain, the total number of impacts, including any subsequent impacts to the opposing sides are shown in Figure 5-7. The three LRB models are subjected to BDBE ground motions and the total number of impacts for various CS are considered. As expected, the *LeadRubberX* model resulted in the most impacts for all clearance to stop values with some ground motions causing multiple impacts. For clearance to stop of 325% and 350% shear strain, the LSLRB model had more impacts compared to the Bouc-Wen model, indicating that the hardening effects of the LSLRB model were not fully engaged at these shear strain levels. For CS of 375% shear strain, the LSLRB model and the Bouc-Wen model resulted in 15 and 8 impacts, respectively, demonstrating that the hardening and softening effects of the LSLRB model counteract the lead degradation and therefore reduce the number of impacts to levels near the Bouc-Wen model.

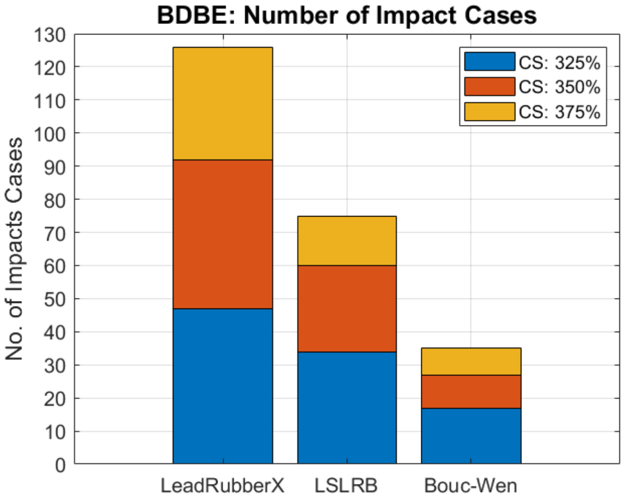

Figure 5-7 Total number of impact cases for 20 BDBE GMs at various CS

Bearing model selection also influences the velocity at impact for a given CS, which determines the severity of impact. In Figure 5-8, the average impact velocity for a CS at specified shear strains are compared for the first, second and third impacts where applicable. The LSLRB model is essentially bounded by the other models. However, the LSLRB model obtained similar average impact velocities compared to the Bouc-Wen model at 375% shear strain or greater for all three impacts. The average impact velocities for the LSLRB model, for all three impacts, begin converging to the Bouc-Wen model starting near 350% shear strain. This suggests that the contributions of the hardening and softening effects, causing the widening of the hysteresis, counteract the strength degradation from heating effects that otherwise would result in higher impact velocities. The LSRB model requires large strains (~325%) in order to develop sufficient rubber hardening as observed in the hysteresis from Figure 5-3. For the 3rd impact, the Bouc-Wen model only attains impact for the 375% shear strain case which may be due to the moat wall placement dependence for 325-375% shear strain as will be explained in the next section.

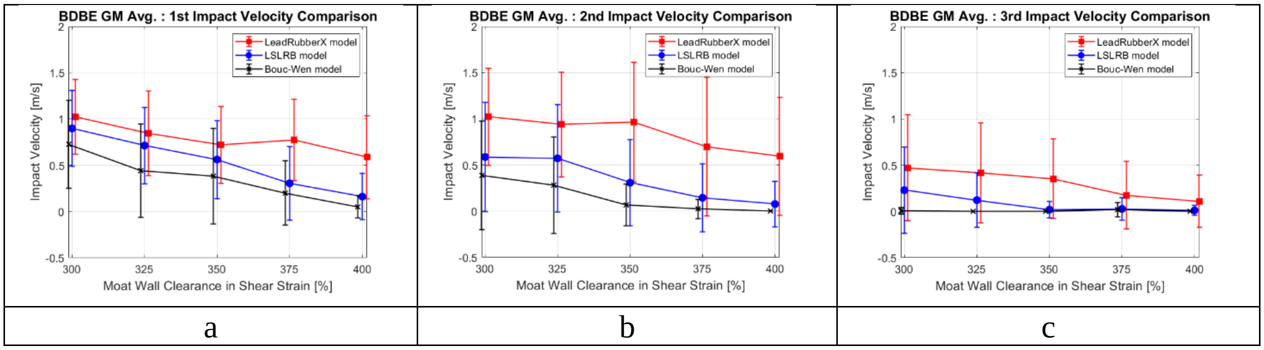

a	b	c

Figure 5-8 *Avg. Impact Velocity for 20 GMs vs Moat wall clearance:* ***(a)*** *1st impact,* ***(b)*** *2nd impact,* ***(c)*** *3rd impact*

5-3-4 Moat wall rebound effects

In order to understand the anomaly of Figure 5-8c of the Bouc-Wen model displaying a nonzero third impact for CS of 375% shear strain, ground motion 7 is examined (Figure 5-9). For CS of 350% shear strain, the first impact changed the trajectory of the displacement when compared to the no moat wall case. The displacement time history for the no moat wall case and the case with CS of 375% shear strain, are essentially identical. The first impact from CS of 350% shear strain, delayed the time in which the second impact occurred when compared to the 375% shear strain case (from 5 seconds to 5.3 seconds). This delay for 375% shear strain case, causes the third impact (at 5.6 seconds) due to the inflection in demand causing impact against the same wall. The inflection in demand can be seen in the no moat wall case occurring at 5.6 seconds.

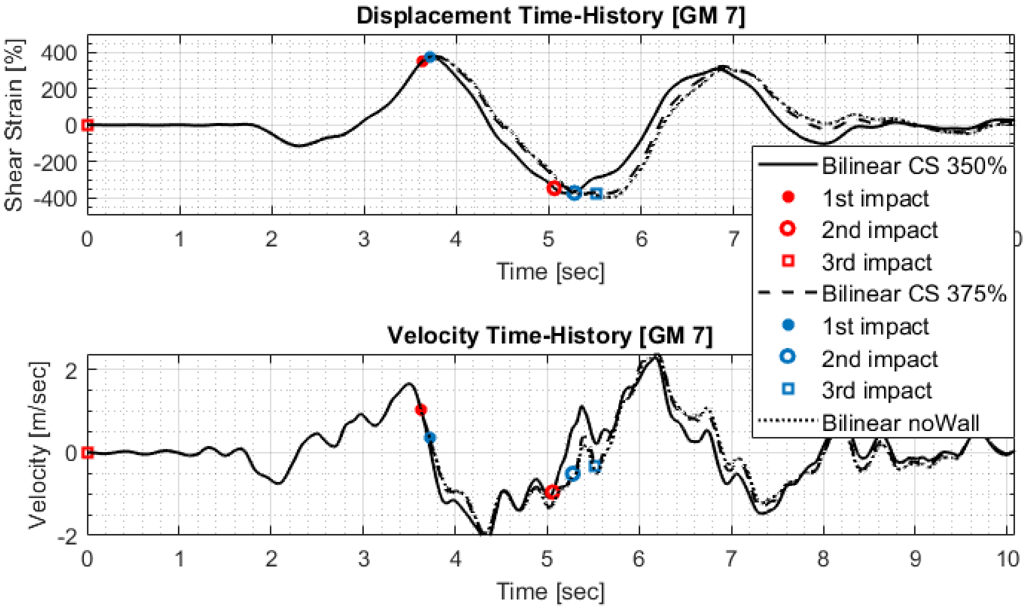

Figure 5-9 Shear strain and velocity time histories for GM 7.

Similar to the bilinear model, the LSLRB model exhibited rebound effects at a CS of 375% shear strain causing a more intense 3rd impacts compared to 350% shear strain CS (Figure 5-8c). These ground motions are 10 and 18, which as mentioned before, correspond to unrealistic characteristic ground motion and a long duration ground motion, respectively, but essentially result in similar behavior for the occurrence.

5-3-5 Impact penetration

ASCE 4-16 requires analysis of impact to the moat wall and design for impact loading if the CS is below the design displacement. The impact velocity for analysis may be calculated either by simulations for BDBE ground motions or by assuming harmonic response of the isolated superstructure to the 95 percentile BDBE displacement at the calculated frequency for the isolation system (ASCE 2017a). Sarebanha et al. (2021) proposed a simplified method to estimate the amount of deformation of the moat wall based on the impact velocity and strength of the moat wall. The model and analysis conducted by Sarebanha et al. (2021) will be revisited here to enhance the modeling efforts by including soil springs and a coefficient of restitution at impact.

The height and thickness of the moat wall considered is 20 m by 1.52 m. The height of the bottom, middle and top soil springs are placed at 3.96, 5.48, and 20 meters, respectively. Plastic analysis for the moat wall was conducted considering two failure scenarios shown in Figure 5-10. In Sarebanha (2018), a section of the moat wall was examined, and a pushover was conducted in SAP2000 to obtain the plastic moment given a unit width of the moat wall.

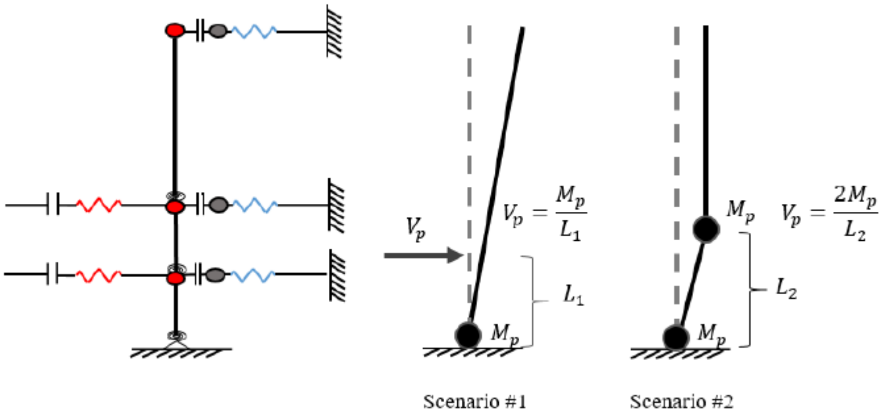

Figure 5-10 Shear strength of the moat wall using plastic design (Sarebanha 2018)

Considering the moat wall as was proposed in a preliminary design for the NPP, the value of L_1 is 3.96 meters and L_2 is 5.48 meters, with the minimum shear capacity resulting from Scenario 1 of $7.09x10^5$ kN for the entire wall with a length of 98.75 meters. For Scenario 2, the shear capacity resulted in $10.3x10^5$ kN, thus Scenario 1 is the governing failure mechanism. Considering Scenario 1, the moat wall deformation prediction model was obtained by using conservation of energy by equivalating the energy of the moat wall simplified elasto-plastic model with the kinetic energy of the NPP as demonstrated in the following equations:

$$E_{kinetic} = E_{strain} \tag{5 − 1}$$

$$E_{kinetic} = \frac{1}{2} m_{NI} v_{imp}^2 \tag{5 − 2}$$

$$E_{strain} = \int F_{moat} \cdot dx \tag{5 − 3}$$

where the mass of the NPP, m_{Ni}, amounts to $4.82x10^8 kg$ and v_{imp} is the relative velocity at impact. For Equation 5-3, an elastoplastic model is assumed and the corresponding energy of the moat wall is calculated by obtaining the area under the curve (Figure 5-11). The simplified elasto plastic model are based on the following equations:

$$F_{moat,max} = V_p = 7.09x10^5\ kN \tag{5 − 4}$$

$$\delta_y = \theta_y x L_1 = 0.012x3.96m = 0.0475\ m \tag{5 − 5}$$

where the maximum force of this equivalent system is assumed to be the shear strength of the wall and the yield displacement δ_y was calculated from yielding rotation of the moat wall section to form a plastic hinge from scenario 1.

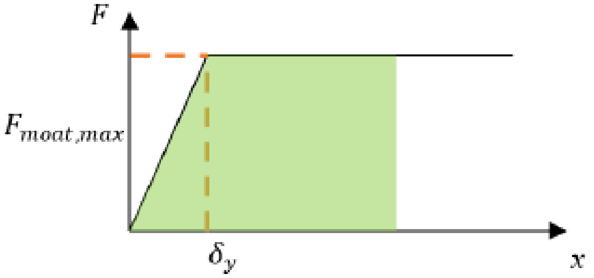

Figure 5-11 Shear strength of the moat wall using plastic design [from: (Sarebanha 2018)]

The previously proposed impact model is revisited to consider the effect of soil contribution. When observing the impact simulations at BDBE under dynamic conditions and evaluating the maximum moat wall deformations, the mechanism of failure is governed by a combination of Scenarios 1 and 2 (Figure 5-12). The effect of the soil springs in better predicting the actual failure mode of the wall is examined.

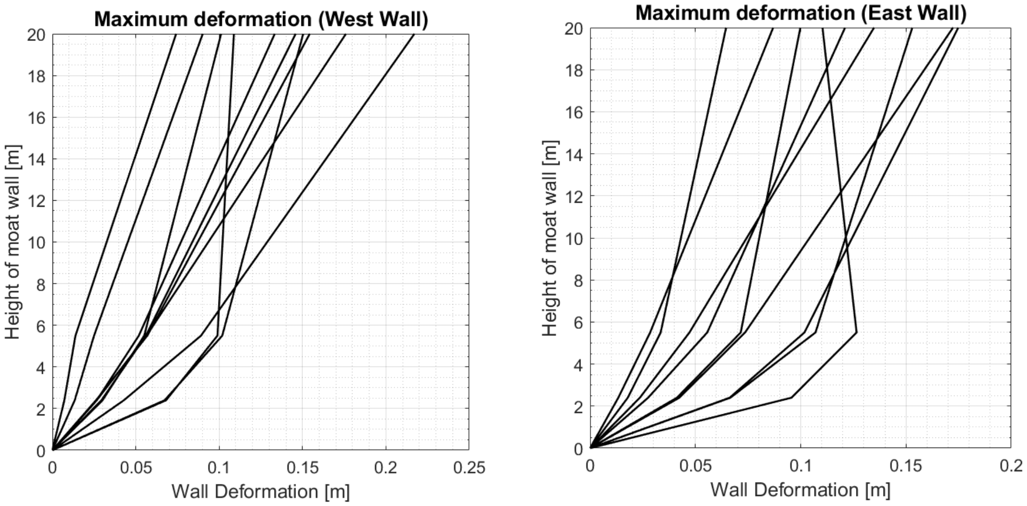

Figure 5-12 Maximum moat wall deformation for first impacts at CS of 300% shear strain.

Furthermore, when examining the impact force and moat wall deformation time history at the record level, more implications of the importance of the inclusion of the soil are deduced. The impact for ground motion 7 is shown for the east wall impact at 3.6-3.75 seconds (Figure 5-12). The moat wall experiences a larger impact force compared to the soil springs, however larger displacements are induced at the middle and top soil springs therefore preventing for full linear failure (or scenario 1). The reason Scenario 1 does not fully occur is because of the backfill soil springs absorb significant energy, especially at the middle and top springs where higher deformations are observed at 5.4m and 20m (Figure 5-10). Therefore, the inclusion of the backfill soil will be considered when applying conservation of energy as discussed in the next section.

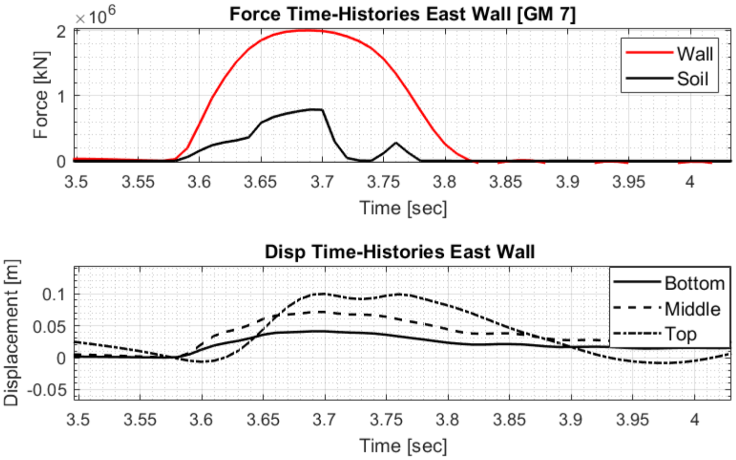

Figure 5-13 Force and moat wall displacement time histories at bottom, middle, and top soil springs at impact for GM7.

5-3-5-1 Moat wall deformation prediction

A simplified approach is considered to predict the moat wall deformation considering the soil springs and their inclusion in the conservation of energy equations from Sarebanha (2018). Applying the equations of conservation of energy, the mass of the NPP, m_{Ni}, amounts to $4.82x10^8 kg$ and v_{imp} is the relative velocity at impact. Since a combination of both failure mechanisms occurred, both scenarios are considered for analysis. The kinetic energy, $E_{kinetic}$ at the short time of impact is transferred to strain and hysteretic energy, E_{strain}, from the moat wall and soil springs that vary in deformation due to the various heights of 3.96 m, 5.48 m, and 20 m, thus changing depending on the scenario being examined. Each of the stiffness, k_{soil}^{i}, of the soil springs along the height of the moat wall are set to be 492.40kN/cm/m of wall for all three springs as described in Sarebanha (2018). The strain energy is extended as follows:

$$E_{kinetic} = E_{strain} \qquad (5-6)$$

$$E_{kinetic} = \frac{1}{2} m_{NI} v_{imp}^{2} \qquad (5-7)$$

$$E_{strain} = \int F_{moat} \cdot dx + \frac{1}{2}\sum k_{soil}^{i}\,\Delta_i^2 \qquad (5-8)$$

where Δ_i dictates the amount of deformation at the soil springs. For the moat wall, the strain energy of the moat wall can simply be calculated as the area under the curve as shown (Figure 5-11) and described in Equations (5-4)-(5-5). Additionally, the soil spring strain energy is calculated using Equation 5-8, where the soil deformation varies depending on the scenario considered.

Scenario 1:

$$\Delta_i = h_i \cdot \theta \qquad (5-9)$$

The corresponding heights of the soil springs are denoted by h_i. Given a moat wall rotation θ, the deformation for the soil spring Δ_i is linear due to the assumed failure of scenario 1. As for scenario 2, the following deformation of soil springs and shear capacity are described as follows:

Scenario 2:

$$F_{moat,max} = V_p = 1.03x10^6\ kN \qquad (5-10)$$

$$\delta_y = \theta_y x L_2 = 0.012x5.4m = 0.0648\ m \qquad (5-11)$$

$$\Delta_1 = L_1 \cdot \theta\ , \qquad \Delta_2 = L_2 \cdot \theta\ , \qquad \Delta_3 = L_2 \cdot \theta \qquad (5-12)$$

Considering scenario 2 (Figure 5-10), the equivalent maximum shear force is larger than scenario 1 due to the plastic analysis described earlier. However, due to the failure mechanism assumed (Equation 5-12), lower displacements for Δ_3 will account for less energy (Equation 5-8) for this failure mechanism compared to scenario 1. Therefore, both scenarios need to be considered.

The predicted values obtained from the plastic analysis are compared with the measured impact velocities and deformations obtained from the nonlinear time history analysis (Figure 5-14). For the case considering soil springs, as the larger deformations are considered, the quadratic terms on both sides begin to develop linear relationship between deformation and impact velocity (Equation 5-8). As for the cases considering no soil springs, the quadratic term of Equation

(5-2) results in a continuous quadratic relationship. Since the initial impact as well as the restitution region of impact should be considered based on Jankowski (2005), it has been found that the restitution coefficient varies from 0.5 to 0.75 for concrete structures (Anagnostopoulos 1988). In Figure 5-14, the impact deformation is compared to the numerical simulations for BDBE ground motions for all three models only considering first impact. The reason subsequent impacts were ignored for this prediction is due to the plastic analysis considers the full capacity of the wall prior to any damage. The impact deformation is highly overestimated when considering a value of one for the coefficient of restitution or only considering the moat wall for both scenarios described in Figure 5-10. The numerical simulation data is shown for all three bearing models to include all available data, which show the velocity-deformation relationship is similar to that predicted by the energy approach. When the soil is included along with a restitution value of 0.5 for scenario 1, this resulted in a nonconservative prediction of the numerical simulations. As for scenario 2 with a coefficient of restitution of 0.5, a good agreement is observed with the numerical simulations. Since coefficient of restitution for concrete varies from 0.5 to 0.75, a coefficient of restitution of 0.5 seems reasonable. However, a coefficient of restitution of 0.7 provides a conservative design recommendation for estimating moat wall deformation. Therefore, it can provide designers the ability to account for the additional displacements the isolation systems may have to account for given an impact velocity. The proposed value for the coefficient of restitution for prediction of moat wall deformation should be a value of 0.7 in order to be reasonably conservative.

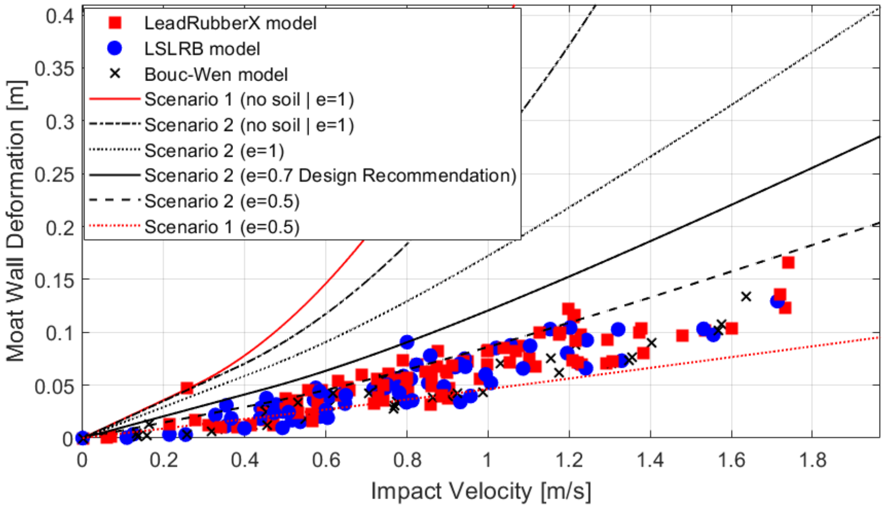

Figure 5-14 Impact velocity versus deformation for GMs compared to predicted.

5-4 Summary and Conclusions

Moat wall impact, which has the potential to amplify floor accelerations and interstory drifts in base-isolated building structures, is a relatively understudied phenomenon. Current approaches to mitigate the pounding effect is to extend the CS to achieve a low probability of exceedance by an earthquake-induced displacement at the isolation plane. For most structures, there are practical and cost constraints that limit the displacement capacity of the isolation system. In the case of nuclear power plants (NPPs), though risk precautions are taken to minimize the occurrence of impact, the avoidance of such phenomena cannot be guaranteed. As such, the consequences of impact need to be more thoroughly studied using advanced modeling tools as proposed here. A simplified macro element developed based on experimental observations and high-fidelity finite element models with a realistic model of a large NPP is revisited.

Prediction of isolation displacements and velocities are critical to assess safety of isolation systems and potential effects of impact to moat walls. Bearing models were compared including the LSLRB model, proposed in Chapter 4, that captures nonlinear behavior observed in experimental data from testing of full-scale bearings. The use of improved models can be beneficial in better predicting the maximum displacements of the isolators and the potential for impact. Consideration of strain hardening in the rubber can be beneficial to reduce the effects of impact, especially when increasing CS to allow the bearing to achieve large strains to levels verified through experimental testing. When comparing the maximum displacements of the *LeadRubberX* model against the proposed LSLRB model, the *LeadRubberX* model highly overestimates the displacements by nearly 50%. The impact velocities for the LSLRB model were significantly lower than the *LeadRubberX* model for all impact velocities. The Bouc-Wen model resulted in the lowest impact velocities due to the fact that no lead core heating was accounted for.

The impact penetration relationship proposed by Sarebanha (2018) was revisited and extended by accounting for soil springs and the coefficient of restitution of 0.7 was found to achieve a good agreement with numerical simulations and obtain a conservative prediction for the moat wall deformation. However, this was conducted with one configuration and one set of material parameters, more configurations should be investigated to further verify this model. Importantly, it was observed that the impact deformation did not differ when comparing the various LRB models. Furthermore, the LSLRB model proved to effectively reduce the average response spectra by nearly half, when extending the wall from 325% shear strain to 375% shear strain.

Chapter 5, consists of only investigations conducted by the author of this dissertation, from material in “Considerations for modeling of base isolated nuclear power plants subjected to beyond design basis shaking.” Sarebanha, A., Marquez, J., Hughes, P., & Mosqueda, G., *Nuclear Engineering and Design (2021).* The dissertation author was the co-investigator and co-author of this paper.

5-5 References

An, G., Kim, M., Jung, J.-W., Mosqueda, G., and Marquez, J. F. (2020). “Evaluation of Clearance to Stop Requirements in A Seismically Isolated Nuclear Power Plant.” *Energies*, 13(22), 6156.

Anagnostopoulos, S. A. (1988). “Pounding of buildings in series during earthquakes.” *Earthquake Engineering & Structural Dynamics*, 16(3), 443–456.

ASCE. (2017). “Seismic analysis of safety-related nuclear structures, ASCE/SEI Standard 4.” American Society of Civil Engineers, Reston, VA.

Bouc, R. (1971). “A mathematical model for hysteresis.” *Acta Acustica united with Acustica*, 24(1), 16–25.

Chandramohan, R., Baker, J. W., and Deierlein, G. G. (2016). “Quantifying the influence of ground motion duration on structural collapse capacity using spectrally equivalent records.” *Earthquake Spectra*, 32(2), 927–950.

DesRoches, R., and Muthukumar, S. (2002). “Effect of Pounding and Restrainers on Seismic Response of Multiple-Frame Bridges.” *Journal of Structural Engineering*, 128(7), 860–869.

Duncan, J. M., and Mokwa, R. L. (2001). “Passive Earth Pressures: Theories and Tests.” *Journal of Geotechnical and Geoenvironmental Engineering*, 127(3), 248–257.

Fukui, H., Fujitani, H., Mukai, Y., Ito, M., and Mosqueda, G. (2020). “Response Evaluation and Analysis Using Impulse of Base-isolated Buildings during a Collision with Retaining Wall.” *Architectural Institute of Japan, Japan Architectural Review*, 66B(3).

Goldsmith, W., and Frasier, J. T. (1961). “Impact: The Theory and Physical Behavior of Colliding Solids.” *Journal of Applied Mechanics*, 28(4), 639–639.

Grant, D. N., Fenves, G. L., and Whittaker, A. S. (2004). “Bidirectional Modelling of High-Damping Rubber Bearings.” *Journal of Earthquake Engineering*, 8(1), 161–185.

Hughes, P. J., and Mosqueda, G. (2020). “Evaluation of uniaxial contact models for moat wall pounding simulations.” *Earthquake Engineering & Structural Dynamics*, John Wiley & Sons, Ltd, 49(12), 1197–1215.

Jankowski, R. (2005). “Non-linear viscoelastic modelling of earthquake-induced structural pounding.” *Earthquake Engineering and Structural Dynamics*, John Wiley and Sons Ltd, 34(6), 595–611.

Kalpakidis, I. V., and Constantinou, M. C. (2009). “Effects of Heating on the Behavior of Lead-Rubber Bearings. I: Theory.” *Journal of Structural Engineering*, 135(12), 1440–1449.

Kammerer, A. M., Whittaker, A. S., and Constantinou, M. C. (2019). *Technical Considerations for Seismic Isolation of Nuclear Facilities (NUREG/CR-7253)*. United States Nuclear Regulatory Commission, Office of Nuclear Regulatory Research, Washington DC.

Kumar, M., Whittaker, A. S., and Constantinou, M. C. (2014). “An advanced numerical model of elastomeric seismic isolation bearings.” *Earthquake Engineering & Structural Dynamics*, 43(13), 1955–1974.

Masroor, A., and Mosqueda, G. (2012). “Experimental simulation of base-isolated buildings pounding against moat wall and effects on superstructure response.” *Earthquake Engineering & Structural Dynamics*, 41(14), 2093–2109.

Sarebanha, A. (2018). “Experimental and Numerical Simulation of Seismically Isolated Critical Facilities under Extreme Seismic Loading.” University of California, San Diego.

Sarebanha, A., Marquez, J., Hughes, P., and Mosqueda, G. (2021). “Considerations for modeling of base isolated nuclear power plants subjected to beyond design basis shaking.” *Nuclear Engineering and Design*, Elsevier Ltd, 379, 111236.

Sarebanha, A., Mosqueda, G., Kim, M. K., and Kim, J. H. (2018). “Seismic response of base isolated nuclear power plants considering impact to moat walls.” *Nuclear Engineering and Design*, 328, 58–72.

Schellenberg, A., Baker, J., Mahin, S., and Sitar, N. (2014). *Investigation of Seismic Isolation Technology Applied to the APR 1400 Nuclear Power Plant-Volume 2: Selection of Ground Motions. Technical Report to KEPCO Engineering and Construction, Pacific Engineering Research Center, University of California, Berkeley, CA.*

Schellenberg, A. H., Sarebanha, A., Schoettler, M. J., Shao, B., Mosqueda, G., and Mahin, S. A. (2016). *Hybrid Simulation of Seismic Isolation Systems applied to an Archetype Nuclear Test (ANT) Power Plant under Design Level Excitation*. PEER.

Shamsabadi, A., Rollins, K. M., and Kapuskar, M. (2007). “Nonlinear Soil–Abutment–Bridge Structure Interaction for Seismic Performance-Based Design.” *Journal of Geotechnical and Geoenvironmental Engineering*, 133(6), 707–720.

U.S. Nuclear Regulatory Commission. (2014). “Design Response Spectra for Seismic Design of Nuclear Power Plants.” *Regulatory Guide No. 1.60, Revision 2*.

Wen, Y. K. (1976). “Method for Random Vibration of Hysteretic Systems.” *Journal of the*

Engineering Mechanic Division, 102(2), 249–263.

Wilson, P. R. (2009). “Large scale passive force-displacement and dynamic earth pressure experiments and simulations.” *PhD Dissertation*, University of California, San Diego, San Diego, CA.

Chapter 6 LSLRB MODEL FOR 2-D SYSTEM AT LARGE STRAINS

6-1 Introduction

Current bearing models (Grant et al. 2004; Kikuchi et al. 2010; Kumar et al. 2014; Ragni et al. 2018) are capable of capturing particular nonlinear behaviors exhibited by elastomeric bearings but have a shortcoming of capturing all observed behavior, especially for large strain 2-D experimental data. In Chapter 4, a parallel model named Large Strain Lead Rubber Bearing (LSLRB) was developed consisting of a combination and modification of the aforementioned models. The LSLRB model can capture nonlinear behaviors such as initial lead hardening, lead heating, rubber hardening, and rubber softening ‘unloading’ effects. The model was verified with experimental data of a large LRB subjected to varying strain levels and appropriately captured the LRB behaviors with only one set of parameters over a wide range of strains. The LSLRB model was limited to one dimensional (1D) excitation due to the rubber softening ‘unloading’ effects that were modeled utilizing a hysteretic model causing issues for 2D excitation.

To extend the LSLRB model for 2D excitation, further examination of the commonalities between HDR and natural rubber (main component of LRBs) were necessary for appropriately capturing the various behaviors observed in LRBs. Tubaldi et al. (2017) developed an anisotropic model capable of capturing anisotropic damage behavior. Ragni et al. (2018) demonstrated that HDR bearings are, in fact, anisotropic by conducting shear tests on high damping rubber specimens. Subsequently developing an anisotropic damage model that was able to capture many of the rubber nonlinear behaviors observed experimentally. The material makeup is similar between HDR and natural rubber with the former having the addition of carbon black. This model was deemed a possible candidate for modeling LRBs at high strains since many of the characteristics of HDR are observed in natural rubber, simply, at higher strains (Harwood et al. 1965). Furthermore, Harwood and Payne (1966a) noticed that a similar softening effect occurs when both HDR and natural rubber are stretched to the same stress levels. The examination of these experiments demonstrates that natural rubber and HDR mechanically behave similar, only at different strain levels. Accordingly, to capture the various behaviors observed in 2D experimental data, adoption of the anisotropic model was deemed important for capturing the various effects observed at large strains. The anisotropic model provided the necessary update of the previous LSLRB model from Chapter 4 of this dissertation.

For design purposes, it is typically sufficient to model an LRB by utilizing the simple bilinear model for isolated structures. However, recent studies considering higher levels of demand due to low-frequency high-risk assessment on critical structures require accurate bearing modeling and require the space to achieve such displacement demands (i.e. surrounding moat). Moat walls may be placed to prevent high strains that may lead to failure of isolation systems. An et al. (2020) utilized an earlier version of the LSLRB model and followed the United States Nuclear Regulatory

Commission (USNRC 2014) guidelines to determine that the moat wall should be set at about 385% shear strain for the same bearings considered here. To verify these levels of strain were feasible, experimental shearing of several LRBs with varying axials loads were sheared to failure resulting in all failures occurring consistently above 400% shear strain. Importantly, these levels of demand are achievable, however require appropriate modeling of LRBs to large strains to accurately capture the necessary moat wall placement and to potentially reduce the velocity at impact to moat walls. Since, recent investigations have observed that impact to moat walls may amplify the superstructure response causing damage to critical contents (Fukui et al. 2020; Masroor and Mosqueda 2012). Modeling of these nonlinear effects are conducted in this study, in addition to, comparing the proposed model against traditional models used in practice to evaluate significant discrepancies in maximum displacements and impact velocities.

6-2 Experimental Bearing Behavior

The experimental data utilized to characterize the behavior of LRB under bidirectional motion is from the same experimental program introduced in Chapter 4, with detailed information found in Eem and Hahm (2019). Large scale LRB experimental tests were conducted at the University of California San Diego Seismic Response Modification Device (SRMD) Facility. The testing data from two identical LRBs are examined for both unidirectional and bidirectional verification of the model proposed here. The bearings were subjected to various characterization tests, with only the tests considered in this study shown in Table 6-1. The test data utilized to capture the LRB behaviors are identical to the data used from Chapter 4 with the addition of 2D experimental data. The LRB was subjected to a constant axial load of 22,000 kN for all tests, corresponding to an average pressure of 13MPa (considering area of rubber). Although the behavior of the bearing depends on the axial load and the bearing size (i.e. shape factor) these effects are not considered here (Sheridan 2012). The axial load corresponds to less than 20% of the undeformed bearing buckling load for which no stiffness degradation was observed. Insufficient varying vertical load tests prevented further insight of the horizontal-vertical coupling effects. Other studies have investigated the importance of axial load variation (Koh and Kelly 1988; Ryan et al. 2005; Sanchez et al. 2013; Sarebanha et al. 2019; Vemuru et al. 2016; Warn et al. 2007).

Table 6-1 Test log utilized for model verification in 1D and 2D

SPECIMEN 1 Test (#)	**Strain (%)**	**Max Strain Rate (1/s)**	**Type**	**Number of cycles**	**DOF**
3	100	1.3	Sine	10	1D
4	100	3.1	Sine	3	1D
11	300	3.8	Sine	1	1D
13	400	5.0	Sine	1	1D
14	100	1.3	Sine	3	1D
15	500	6.3	Sine	1	1D
SPECIMEN 2 Test (#)					
9	200	0.21	EQ	N/A	2D
11	300	3.8	Sine	1	2D
13	400	5.0	Sine	1	2D
15	500	6.3	Sine	1	2D

The two test specimens underwent similar 1-D sinusoidal tests for Test Runs 1-9. For Test Runs 11 and 13, specimen 2 was subjected to a 2-D sinusoidal characterization tests while specimen 1 was subjected to 1-D sinusoidal characterization tests (Figure 6-1a). The noteworthy experimental data is Test Run 13 from specimen 2 exhibiting similar nonlinear behaviors in the longitudinal direction as in the unidirectional Test Run 13 from specimen 1 (Figure 6-1b). It is important to note that the hystereses are equivalent with similar nonlinear behaviors discussed in Chapter 4 such as initial lead hardening, lead heating, rubber hardening, and softening “unloading” effects considered to be from Mullins and scragging effects (causing the widening of the hysteresis). It is important to note the loading in the lateral direction (Figure 6-1c) is not at large strains and the longitudinal direction demonstrates to be essentially unaffected and behaves similar to 1-D testing (Figure 6-1). Consequently, a similar approach to the previous LSLRB model along with modifications of the formulation were necessary to capture such behaviors.

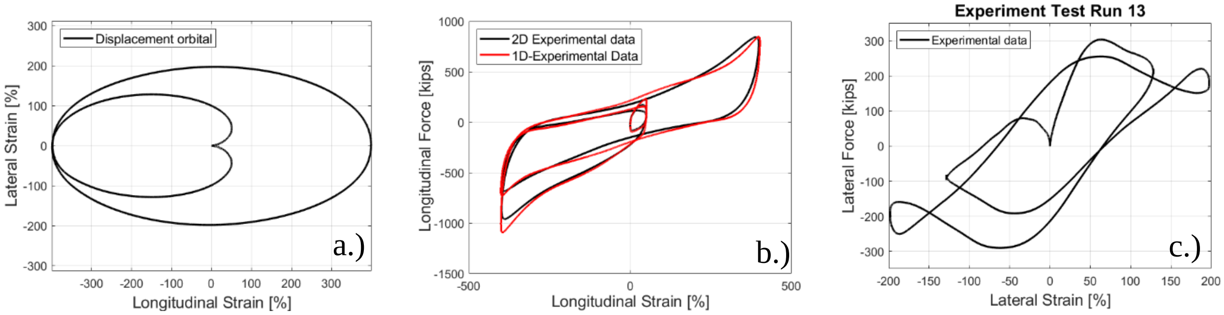

Figure 6-1 Test 13 1-D versus 2-D a.) Displacement orbital for 2-D test b.) Longitudinal hysteresis comparison for 1-D and 2-D tests c.) Lateral hysteresis for 2D test

6-3 Numerical Modeling

In order to accurately model the nonlinear behavior exhibited by LRBs at large strains, the sources of these behaviors should be well understood. As previously mentioned, the natural rubber in the LRB behaves similar to HDR when undertaken to similar levels of shear stress. Since the material makeup is the same with the difference being the addition of carbon black in HDR material, similar behaviors between natural rubber and HDR are expected, only at higher strains for natural rubber. Therefore, models developed for HDR bearings will be used and modified to appropriately capture behaviors found experimentally in LRB. The novel LSLRB (Large Strain Lead Rubber Bearing) model consists of a hyperelastic model with Mullins and scragging effects that includes anisotropic damage effects, along with a hysteretic model based on Dafalias and Popov (1975) that is modified to include lead core heating and initial lead hardening. Here it will be extended to 2-D behavior.

6-3-1 Hyperelastic Model

In order to better capture the contribution of rubber to the overall behavior of LRB, a hyperelastic model similar to Grant et al. (2004a) is introduced. The formulation is modified by introducing the idea of representative directions (Freund and Ihlemann 2010) in order to capture 2D experimental data.

6-3-1-1 Representative directions with Mullins effect

In order to model the deformation induced anisotropy inherent in Mullins effect, the idea of representative directions or the one-dimensional representation of 2D and 3D material behaviors is utilized. The basis of this model is that a homogenization of 1D material unit vectors capture the corresponding damage induced within that particular direction. For a particular displacement within the 2D plane space where the bearing may be displaced, the displacement can then be projected onto these representative directions that can accumulate damage. Let the unit vector $\boldsymbol{n}^{\boldsymbol{\theta}}$ represent the direction corresponding to the angle of θ, and the projection on this particular direction from a given shear displacement of $\boldsymbol{U}$ produces the following:

$$\varepsilon^{\theta} = \boldsymbol{U} \cdot \boldsymbol{n}^{\boldsymbol{\theta}} \tag{6 - 1}$$

For each direction, this represents the corresponding 1D deformation measure ε^{θ} with its associated corresponding force, f^{θ}. The internal variables for the damage dissipative phenomena can be accumulated by each representative direction since they may differ from direction to direction. These can be collected once the evolutions laws are established, the following integral can collect the accumulation of damage:

$$f_m(U; \boldsymbol{v}) = \frac{1}{\pi} \int_0^{\pi} f\left(\varepsilon^{\theta}, \boldsymbol{v}^{\theta}\right) \boldsymbol{n}^{\boldsymbol{\theta}} d\theta \tag{6 - 2}$$

Since the directions are homogenous and there is typically a finite number of directions the damage can therefore be approximated by a summation of each individual direction. Since each representative direction accounts for both positive and negative direction, the summation can be done from zero to π instead of 2π. The transient response along with the material law are represented by the following equations:

$$f_m^{\theta} = \alpha_e\left(1 - q_e^{\theta +}\right) f_e^{\theta} \quad for \quad \varepsilon^{\theta} > 0 \tag{6-3}$$

$$f_m^{\theta} = \alpha_e\left(1 - q_e^{\theta -}\right) f_e^{\theta} \quad for \quad \varepsilon^{\theta} < 0 \tag{6-4}$$

where f_e^{θ} is the typical hyperelastic model:

$$f_e^{\theta} = \left[a_1 + a_2\left\|\varepsilon^{\theta}\right\|^2 + K_{S1} a_3 \left\|\varepsilon^{\theta}\right\|^4\right] \varepsilon^{\theta} \tag{6-5}$$

The hyperelastic model consists of the a_1, a_2, and a_3 as material parameters and K_{S1} denotes scragging damage or permanent damage in the rubber (further examined in the next section). The damage parameters q_e^+ and q_e^- tend to limit values depending on the current value of deformation experienced along the corresponding direction. The evolution laws for ε^{θ} > 0 are proposed in the following form:

$$\dot{q}_e^- = 0 \tag{6-6}$$

$$\dot{q}_e^+ = \left(\left(\frac{\varepsilon^{\theta}}{U_{mod}}\right)^{\beta} - q_e^+\right) \ if \ q_e^+ < \left(\frac{\varepsilon^{\theta}}{U_{mod}}\right)^{\beta} \tag{6-7}$$

$$\dot{q}_e^+ = 0 \ if \ q_e^+ \geq \left(\frac{\varepsilon^{\theta}}{U_{mod}}\right)^{\beta} \tag{6-8}$$

For ε^{θ}<0, similar evolution laws are used except roles for $\dot{q}_e^+$ and $\dot{q}_e^-$ are interchanged in Equations 6-6 to 6-8, and ε^{θ} is replaced with $\left|\varepsilon^{\theta}\right|$. It is important to note that the formulation is similar to the formulation presented in Tubaldi et al. (2017) and summarized in Section 2-2-5. The velocity parameter ζ_e, is not used for this calibration and is simplified (Equation 6-7) due to the fact that natural rubber is not rate dependent for the rate of loading considered here (Diani et al. 2009; Ishida et al. 1991). A sensitivity study in the next section will demonstrate issues with the use of this parameter (Section 5-5-1). The maximum value that can be reached by q_e^+ and q_e^- for strain amplitudes not exceeding $|U|$ is given by the expression $\left(\varepsilon^{\theta}/U_{mod}\right)^{\beta}$, where U_{mod} is the maximum amplitude for which the model is deemed valid.

6-3-1-2 Representative directions with scragging damage (extension of Grants model)

Since scragging damage is a subset of Mullins effect, representing damage by individual directions and modifying the evolution of the scragging damage to be similar to Mullins damage (Grant et al. 2004) was necessary to capture behaviors observed experimentally. Alongside these modifications, the idea of having the scragging damage term applied to the 5th order term a_3 in Equation 6-5, proved to be essential to obtain a proper calibration of the LRB. The rational for conducting this modification is two-fold. First, no experimental scragging ‘permanent’ damage was observed for the post-elastic stiffness, a_1 (Equation 6-5). Second, the majority of the hardening and softening effects occur at larger strains for natural rubber when compared to high damping rubber (Harwood et al. 1965). Therefore, the scragging damage was applied to the higher order term, a_3. For example, in Figure 6-2 the hysteresis is shown for Test Run 3 and Test Run 14 for comparison. Importantly, the LRB prior to Test Run 3 underwent shear strains of up to 100%, whereas prior to Test Run 14 the bearing had undergone up to 400% shear strain. Interestingly, the scragging damage for the LRB showed no difference for the post elastic stiffness, demonstrating that scragging effects are negligible on the post-elastic stiffness.

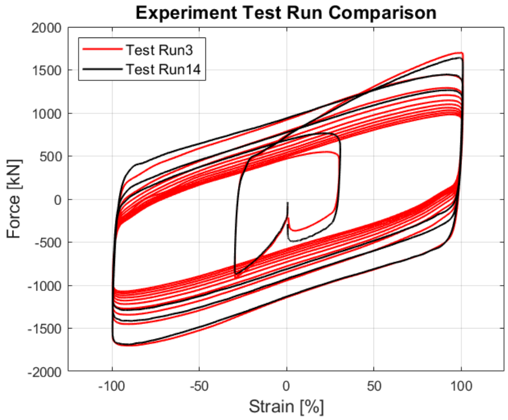

Figure 6-2 Constant post-elastic stiffness after test sequence Test Run 3 versus 14

Representing the scragging damage by individual directions similar to Mullins effect seemed intuitive. The representative directions given an arbitrary shear displacement, $\boldsymbol{U}$, is projected to each individual direction in a magnitude sense:

$$\varepsilon^{i\theta} = |\boldsymbol{U} \cdot \boldsymbol{n}^{\boldsymbol{i\theta}}| \qquad (6-9)$$

where i represents the representative direction and therefore $\varepsilon^{i\theta}$, represents the displacement projected onto that particular representative direction. The scragging evolution laws are represented by:

$$\begin{cases} if\ \varepsilon^{i\theta} \geq D_S^{i+} \\ \qquad D_S^{i+} = \varepsilon^{i\theta} \\ \qquad \dot{D}_S^{i-} = \dot{D}_S^{i+} \\ \qquad \dot{D}_S^{i} = 0 \\ if\ \varepsilon^{i\theta} < D_S^{i+}\ \ and\ \ D_S^{i-} > 0 \\ \qquad \dot{D}_S^{i+} = 0 \\ \qquad \dot{D}_S^{i-} = -\varepsilon^{i\theta} \\ \qquad \dot{D}_S^{i} = \left|\dot{D}_S^{i-}\right| \\ if\ D_S^{i-} < 0 \\ \qquad \dot{D}_S^{i-} = 0 \\ \qquad \dot{D}_S^{i+} = 0 \\ \qquad \dot{D}_S^{i} = 0 \end{cases} \qquad (6-10)$$

Grant's formulation for scragging effects captures the long-term damage that accumulates as a previous maximum displacement norm is exceeded. However, unlike Mullins effect, the damage parameter does not accrue at the reversal, instead, it accumulates when the displacement norm returns below the lower threshold (that represents the amount that the displacement norm has exceeded the previous maximum displacement). Since scragging is a subset of Mullins' effect (Diani et al. 2009), with the former being the long term damage that was construed by Clark et al. (1997), the accumulation of damage should occur at the commencement of the reversal, similar to Mullins effect (Figure 6-3). The evolution of the scragging damage follows Equation 6-10, if the represented displacement $\varepsilon^{i\theta}$ exceeds a previous maximum displacement, the amount of exceedance is stored by, D_S^{i-}, and the new maximum displacement is set by D_S^{i+}. Once the reversal occurs, the scragging damage, D_S^{i}, increases by the amount that the displacement returns, with the maximum amount dictated by the lower threshold, D_S^{i-}. In Figure 6-3, the scragging damage evolution parameter is shown for a sine wave with a previous permanent damage of value one. As the displacement exceeds the value of one, the amount of exceedance is captured by D_S^{i-} and the new maximum is set by D_S^{i+}, the damage parameter D_S^{1} increases by D_S^{-1} following the evolution from Equation 6-10.

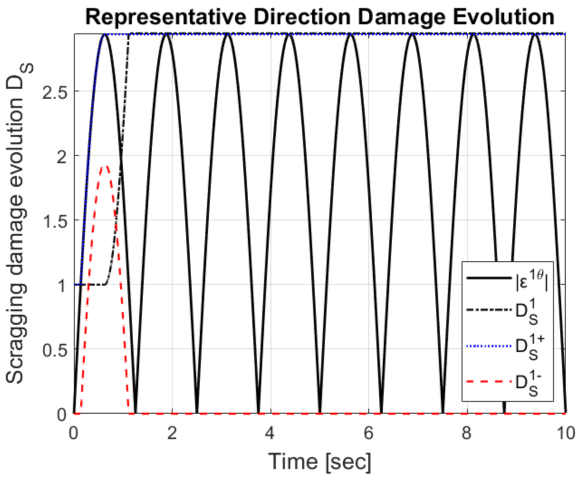

Figure 6-3 Scragging damage evolution modification

Once the scragging parameter c_1 is determined, the scragging reduction can be calculated using the following formulation:

$$K_{S1}^{i} = \exp\left(-c_1 \left(D_S^{i}\right)^3\right) \qquad (6-11)$$

where c_1 is a parameter that can be calibrated for experimentally.

6-4 Sensitivity Study LSLRB model

Modifications to the evolution laws of the anisotropic Mullins damage and the evolution of scragging damage were required to capture the nonlinear behaviors observed experimentally. These two significant modifications will therefore be examined to ensure the model is performing as expected and potentially reduce the number of parameters utilized for simplicity and practicality of the model. The following analysis will be done for 1-D sinusoidal inputs in order to better understand the effects the parameters have on the overall system.

6-4-1 Mullins damage effect

The evolution of Mullins damage, as presented in Section 2-2-5, is modified for the damage model to become rate-independent (Equation 6-7), in addition to, eliminating the corresponding velocity parameter ζ from Equation 2-46. The strain rate parameter ζ from Equation 2-46 amplifies the input strain rate, $\dot{\epsilon}^{\theta}$. Both the strain rate parameter ζ, and the strain rate $\dot{\epsilon}^{\theta}$ are extracted due to the sensitivity study conducted here. The strain rate parameter was set to 0.5, 1, and 1.5 in order scale the input strain rate levels and observe the effects on the damage evolution and excitation frequency (i.e. 2hz, 4hz, 8hz) (Figure 6-4a). In Figure 6-4b, it can be observed that as the strain rate is increased the less hardening or more damage is induced in the LSLRB model when considering Equation 6-7. Rate hardening effects are typically negligible, and even so, the effect occurs in an opposing manner, with higher strain rates inducing increasing hardening effects (Wei et al. 2020). The strain rate parameter caused many issues when undergoing a dynamic analysis invoking unrealistic hardening effects. As previously mentioned, the natural rubber found in LRBs is typically considered rate-independent further indicating that it is appropriate to extract the parameters. Recent studies imposing varying strain rates near ground motion levels 0.8hz to 4hz showed insignificant differences in the response for LRBs (Wei et al. 2020).

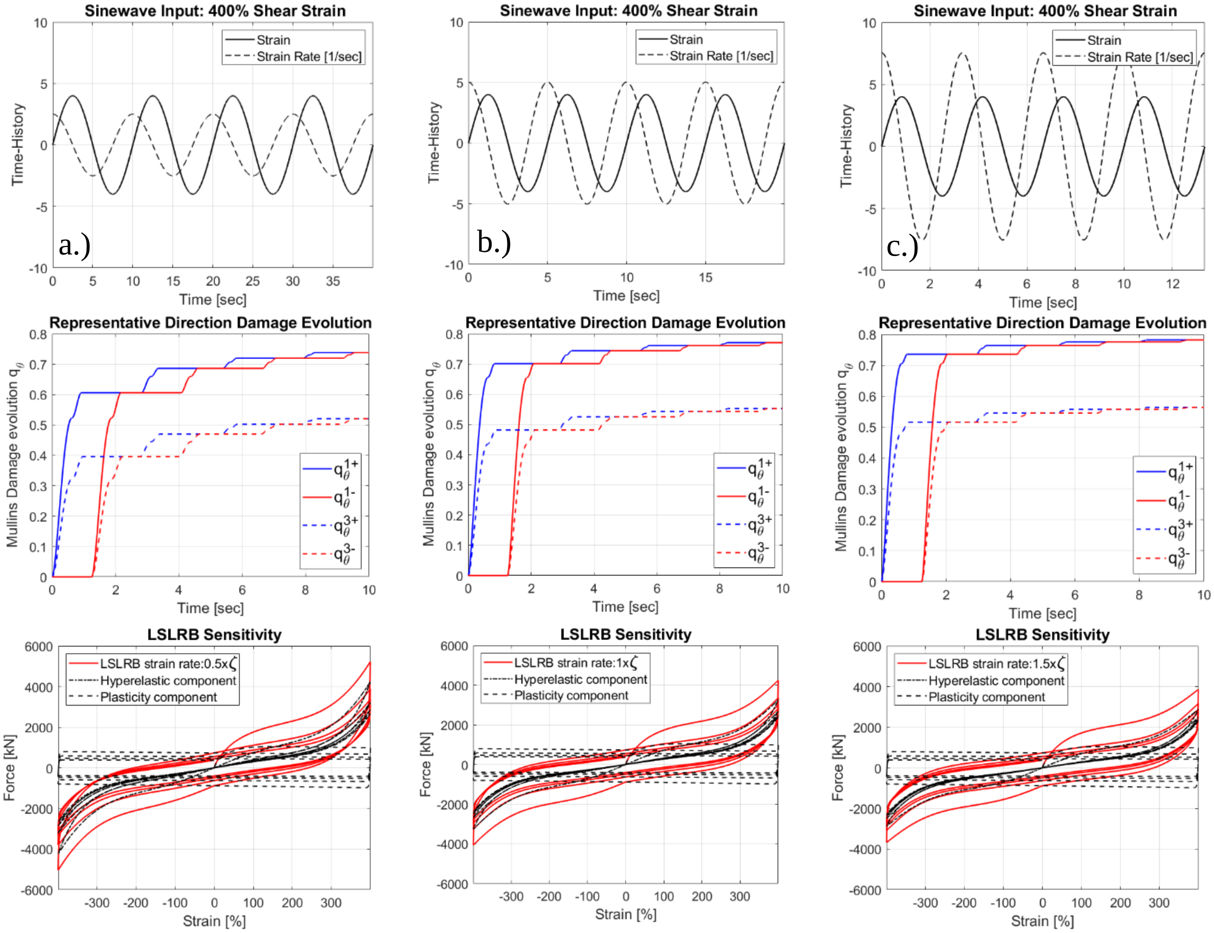

Figure 6-4 LSLRB model sensitivity at 400% shear strain at various strain rates due to parameter at: a.) 0.5, b.) 1 and c.)1.5

In order to further simplify the model, a sensitivity study was conducted on the α_e parameter from Equations 6-3 and 6-4, to demonstrate the effects it has on the damage evolution and hysteresis (Figure 6-5), and its potential for extraction. In the formulation described by Ragni et al. (2018) and Tubaldi et al. (2017), not many details were given for this parameter and the reason for its utilization. For the given calibrated parameter, the α_e parameter is multiplied by a factor of 0.5, 1.0, and 1.5 as shown in Figure 6-5. The parameter tends to be an amplification of the hyperelastic model, the higher the factor the larger the restoring force as expected due to the formulation (Equations 6-3 and 6-4). A value of one is imposed instead of the α_e parameter to simplify the model for practical use and to obtain continuity with the scragging reduction factor, K_{S1}^{i} (Equation 6-11).

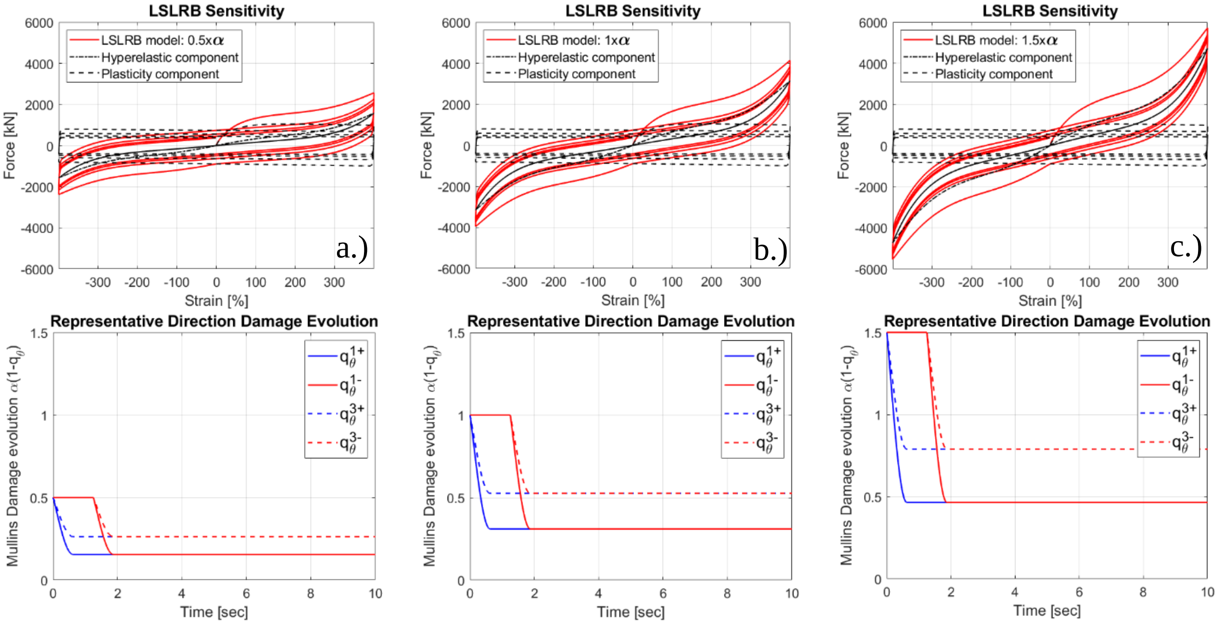

Figure 6-5 LSLRB model sensitivity parameter factored by: a.) 0.5 b.) 1.0 and c.) 1.5.

6-4-2 Scragging damage effect

The contribution of the scragging damage was deemed important for higher strains, as previously mentioned, since the sequence of the tests demonstrated no permanent damage for the post-elastic stiffness. In Figure 6-6, the sensitivity of the parameter c_1 is plotted at 0.5, 1.0, and 1.5 of the calibrated parameter. For all cases, the previous maximum damage was set at one. As the displacement exceeded the value of one and began to have a reversal, the scragging damage D_S^1 increases by the amount of exceedance of one until reaching the maximum displacement. This damage accumulates as the reversal occurs by the equivalent amount as the increase of damage from the previous maximum damage, following the evolution laws from Equation 6-10. The restoring force at the negative shear strains decreases as the value of c_1 increases indicating more scragging damage.

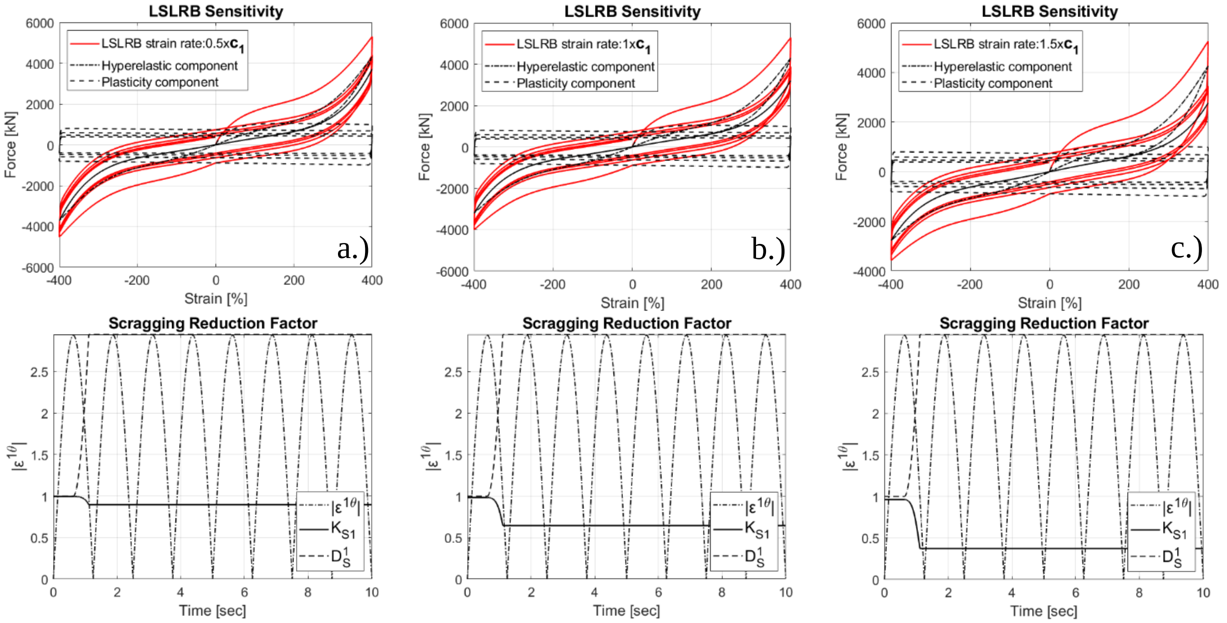

Figure 6-6 LSLRB model sensitivity parameter factored by a.) 0.5 b.) 1.0 and c.) 1.5

6-4-3 Initial lead hardening effect

As for the initial lead hardening, experimentally the characteristic strength due to the lead core has been observed to initially start at a fraction of the actual characteristic strength. Then, depending on the accumulated displacement, typically half a cycle, it begins to approach the actual characteristic strength. Considering Equation 4-10, c_5 was not considered since the value can be clearly interpreted as the initial fraction of the characteristic strength. In Figure 6-7, the parameter c_6 is multiplied by a factor of 0.5, 1.0, and 1.5 to understand the sensitivity of this parameter on the plasticity component of the LSLRB model. The larger the c_6 value, the more rapid the initial characteristic strength approaches the actual characteristic strength. As the displacement increases, the lead hardening fraction increases and begins to approach the value of one.

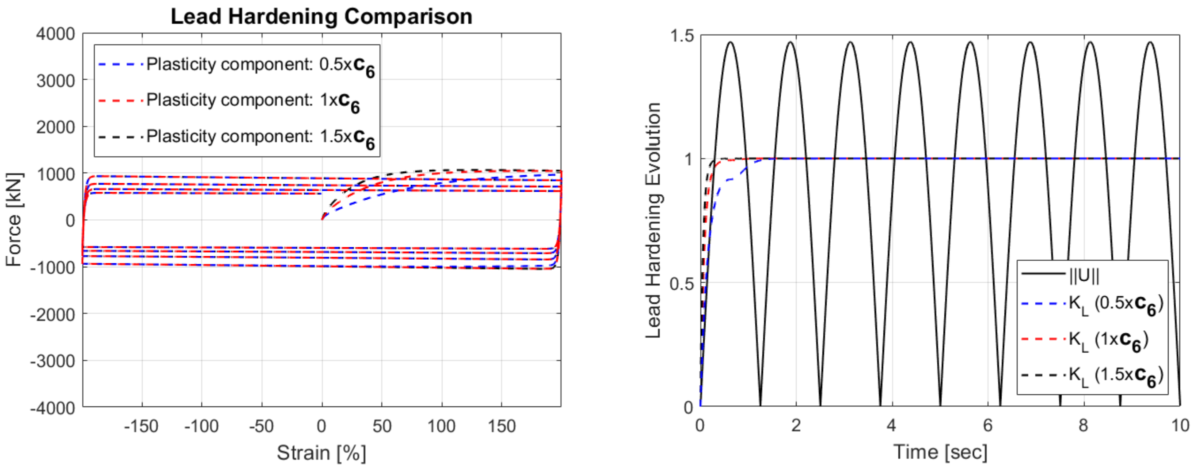

Figure 6-7 LSLRB model sensitivity parameter multiplied by 0.5,1.0, and 1.5

6-5 Bidirectional LSLRB Model

The examined model components are utilized to extend the Large Strain Lead Rubber Bearing (LSLRB) to bidirectional excitation. The model is an extension of the model introduced in Chapter 4, with the addition of the anisotropic damage effects observed in the rubber. The addition of this model improved the ability to capture the nonlinear behaviors observed not only for bidirectional experimental data in addition to 1D experimental data discussed in Chapter 4 (Table 6-1). The inclusion of 1D experimental data was to account for more data along with enforcing the behaviors discussed in Section 6-2 (Figure 6-1). The LSLRB model consists of a hysteretic model that accounts for both the initial lead hardening and the lead core heating (Kalpakidis and Constantinou 2009b), in conjunction with, a hyperelastic model that is able to account for anisotropic Mullins effects and scragging effects.

In order to capture the various behaviors observed experimentally, a calibration of the various parameters shown in Table 6-2 was performed. To ensure convergence and computational efficiency, understanding of the parameters and setting bounds were essential. In Table 6-2, the significance of each parameter is detailed along with the bounded values. It is important to note that for scragging (permanent damage), the damage parameter, D_S, is retained between test runs in order to accurately capture the rubber damage. For Mullins effect, since it represents the 'short term' damage, the damage parameter D_M was set to zero for each experimental test run.

Table 6-2 Description and calibration of parameters for the LSLRB model.

Model	Parameter	Description	Parameter Bounds	Calibrated Parameter
Hyperelastic model	a_1	Post-elastic stiffness	$2950 \leq a_1 \leq 3800\ (\frac{kN}{m})$	**3499.0**
	a_2	Nonlinear (moderate strain softening)	$-50 \leq a_2 \leq -10(\frac{kN}{m^3})$	**-4446.9**
	a_3	Nonlinear (large strain hardening)	$5.0 \leq a_3 \leq 30\ (\frac{kN}{m^3})$	**30234.1**
Rubber damage	c_1	Scragging damage	$0 \leq c_1 \leq 5\ m^{-3}$	**0.60**
	γ_{mod}	Maximum amplitude	$1 \leq \gamma_{mod} \leq 2\ m$	**1.3**
	β	Rate of damage	$0 \leq \beta \leq 5.0$	**1.1**
Hysteretic model	b_1	Characteristic strength	$1000 \leq b_1 \leq 1500\ kN$	**1119.5**
	b_2	N/A	N/A	**N/A**
	b_3	Sharpness of reversal	$0 \leq b_3 \leq 200\ \frac{1}{m}$	**292.7**
Lead hardening	c_5	Initial fraction of Characteristic strength	$0 \leq c_5 \leq 1$	**0.9**
	c_6	Rate of increase to 'true' characteristic strength	$0 \leq c_6 \leq 40\ m^{-1}$	**11.1**

In order to calibrate for one set of parameters, all experimental tests varying from low to large strains were utilized to minimize a multi-objective normalized root mean squared error (NRMSE). The downhill simplex algorithm (Lagarias et al. 1998) was performed in order to minimize the error function, represented as the following:

$$\in = \sum_{i=1}^{no.\,tests} (w_i NRMSE_i) \qquad (6-12)$$

by modifying the parameters presented in Table 6-2. The $NRMSE_i$ is calculated as the difference of the experimentally measured force and the force resulting from the model normalized by the range of the maximum and minimum forces observed experimentally. The tests considered for this calibration include both 1D and 2D experimental data shown in Table 6-1, with equal weights, w_i, summing to one.

The hysteresis for the obtained calibrated parameters (Table 6-2) can be observed in Figure 6-8. The NRMSE for all 1-D tests resulted in less than 4% error showing a good agreement with experimental data capturing the initial lead core hardening, lead core heating, hardening effects, and softening 'unloading' effects. The LSLRB model due to the initial lead hardening enabled closer convergence to the actual characteristic strength.

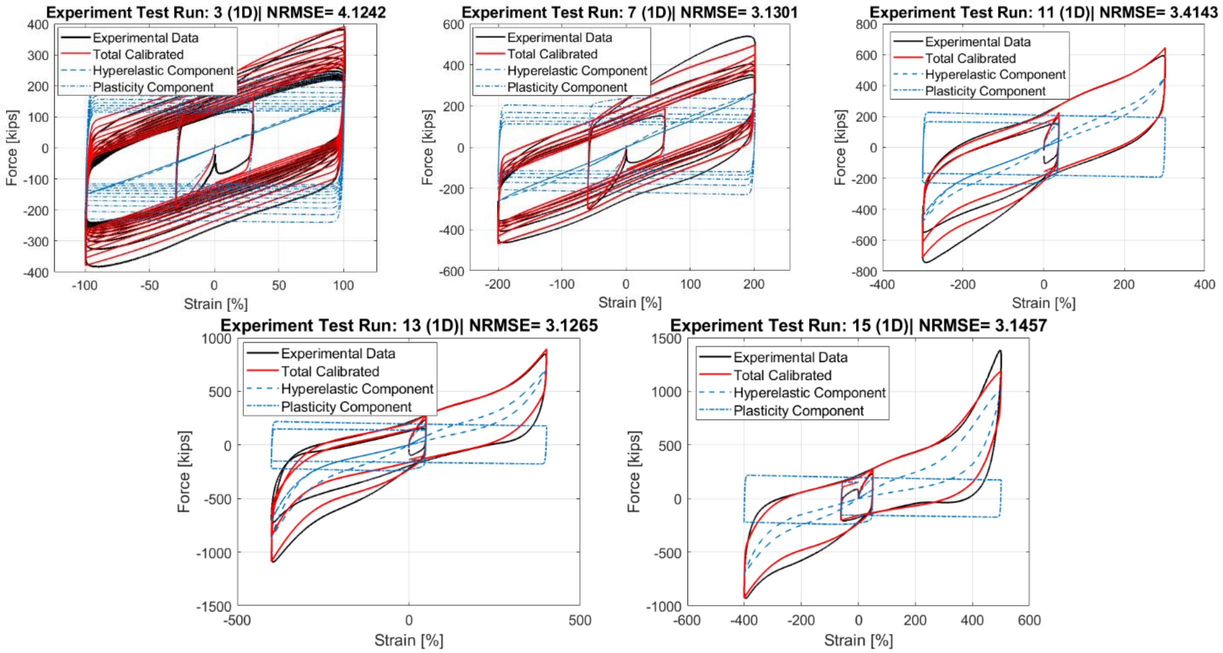
Experiment Test Run: 3 (1D)| NRMSE= 4.1242

Experiment Test Run: 7 (1D)| NRMSE= 3.1301

Experiment Test Run: 11 (1D)| NRMSE= 3.4143

Experiment Test Run: 13 (1D)| NRMSE= 3.1265

Experiment Test Run: 15 (1D)| NRMSE= 3.1457

Figure 6-8 Calibrated LSLRB model to 1-D experimental data

In Figure 6-9, the calibrated LSLRB model is compared against the 2D experimental data showing good agreement. For both Test Runs 11 and 13 for the lateral direction, the LSLRB model reaches a NRMSE of 7%. The larger NRMSE for the lateral direction is mainly due to the normalization of the maximum and minimum forces in the NRMSE formulation being small comparatively to the longitudinal direction. Additionally, the displacement orbital produced highly complex effects in the lateral direction. Considering the 2-D orbital loading (Figure 6-1a), the hysteretic model reduces in the lateral direction as the direction of the velocity is oriented in the longitudinal direction. Since the hyperelastic component is nonlinear and coupled, rather than only being composed of a constant post-elastic stiffness, the restoring force reduces as the strain magnitude decreases from large strains to moderate strains. Although the hyperelastic component of the LSLRB model attempts to produce inverse reversal effects at peak lateral strains due to the orbital (Figure 6-1), it is insignificant compared to the experimental results (Figure 6-9b-Figure 6-9d). One speculation for this phenomena is that the rubber, especially, at these larger strains develops hardening effects followed by softening effects, after which, some recovery occurs as the bearing begins to cycle once again (Harwood and Payne 1966b). Therefore, the breakdown of forces from the orbital when recovery occurs causes these inverse reversal loops to occur in the lateral direction since the response of the rubber should be considered in a magnitude sense for displacement orbitals. Other experimental observations of two bearings, an LRB and natural rubber bearing (Yamamoto et al. 2009), were conducted and both bearings demonstrated these inverse reversals indicating that the behavior can be attributed to the rubber.

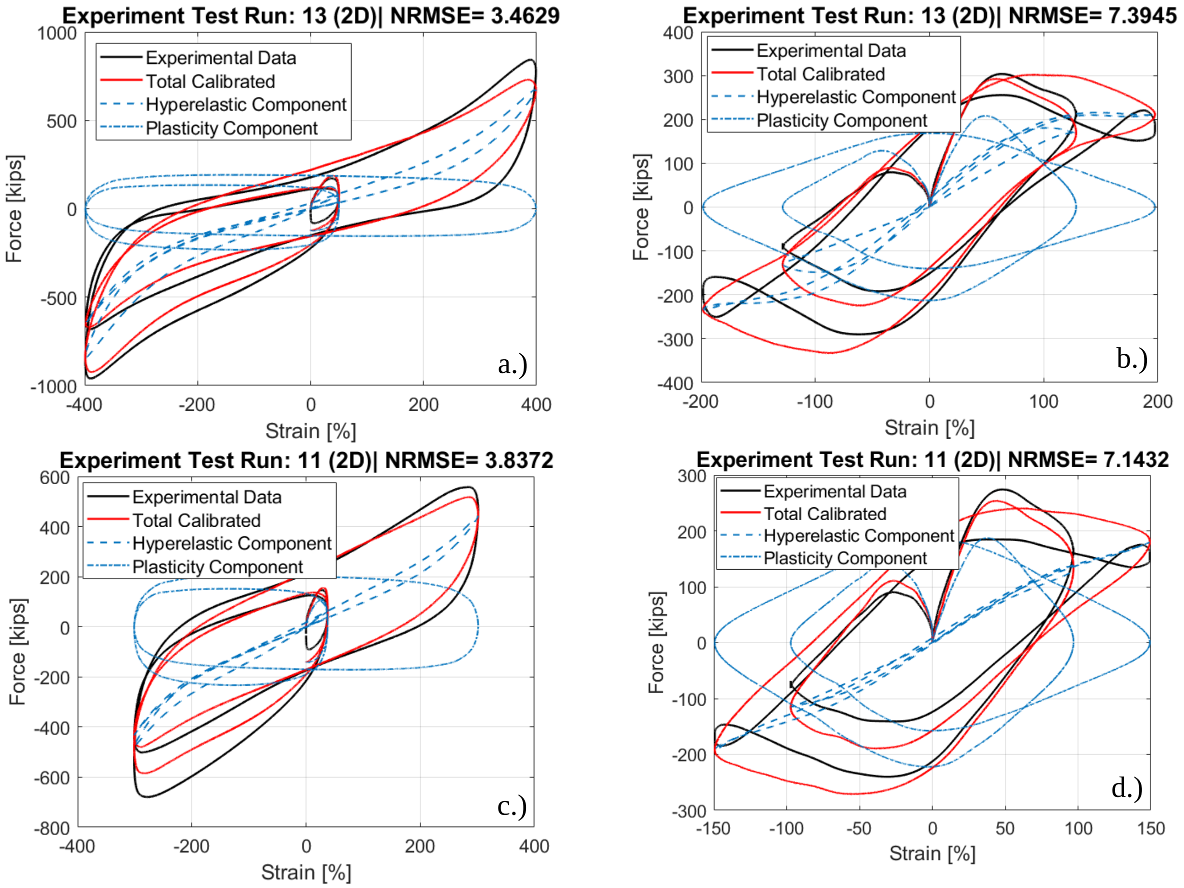

Figure 6-9 Calibrated LSLRB model to 2-D experimental data Test Run 13: a.) longitudinal b.) lateral direction, Test Run 11: c.) longitudinal d.) lateral direction

In order to evaluate the calibrated LSLRB model, a comparison is conducted with two other widely used models for LRBs. The two models used are the smooth Bouc-Wen bilinear model with constant parameters implemented in OpenSees as the *LeadRubberX* model *(without lead heating)* hereinafter referred to as a Bouc-Wen model, and the *LeadRubberX* model *(with lead heating)*. The calibration of these models is presented in Chapter 4 of this dissertation.

6-6 Earthquake Response of SDOF System

In order to evaluate the LSLRB model, a nonlinear time history analysis is conducted on a SDOF system and compared against traditional models such as the Bouc-Wen model and the *LeadRubberX* model. The 20 ground motions used for the analysis were NRC spectrally matched utilizing the USNRC (2014) guidelines, where the response spectra can be seen in Figure 6-10 (Schellenberg et al. 2014). To achieve BDBE, the ground motions are scaled by a factor of 1.67 equating to a 100,000 year return period. The reason a factor of 1.67 is due to a factor of 2 caused exceedance of the capacity of the LSLRB model creating instabilities after 500% shear strain. Regardless, the LRB would physically experience failure at these levels of strain.

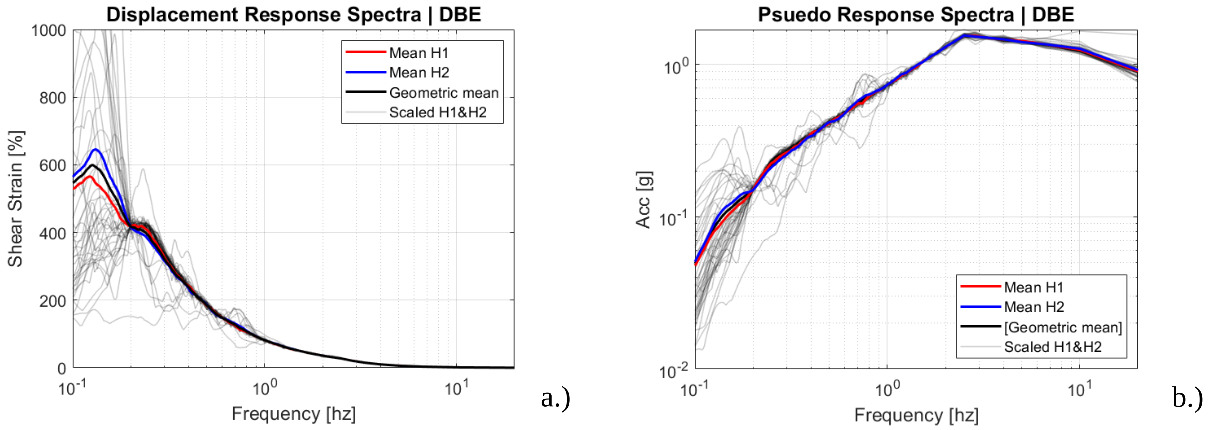

a.) b.)

Figure 6-10 NRC spectrally matched at DBE: a) Shear strain spectra b) Pseudo acceleration response spectra

The BDBE ground motion Kocaeli, Turkey, Izmit is considered to observe the difference in each model at the record level. The ground motion is considered a near fault type ground motion (Figure 6-11) causing demand both in the first quadrant and the fourth quadrant of the x and y orbital displacement plot (Figure 6-11c). These two distinct excursions are identified on the plots with numbers. The first excursion indicated by a 1, occurs in the positive x and y direction simultaneously, with a higher demand in the x-direction compared to the y-direction. The hysteresis for the y-direction at this particular excursion demonstrates an anomaly, indicated by a 1 (Figure 6-11e), that can be explained by the hyperelastic formulation in Equation 6-5. The hyperelastic component is highly dependent on the magnitude of the displacement, and at which point it is decomposed into its components. Consequently, at this first high stain point, the magnitude of displacement is large mainly in the x-direction while the displacement in the y-direction is relatively low. However, due to the large magnitude displacement the magnitude force is large and as the force magnitude is decomposed into the corresponding components, the resulting peak force in the y-direction occurs. For the second peak displacement, the shear strain demand occurs both in the negative x and y direction resulting in the hardening for both hysteresis plots (Figure 6-11e-Figure 6-11f). The hardening is more pronounced for the y-direction due to higher strain levels reached in that particular direction.

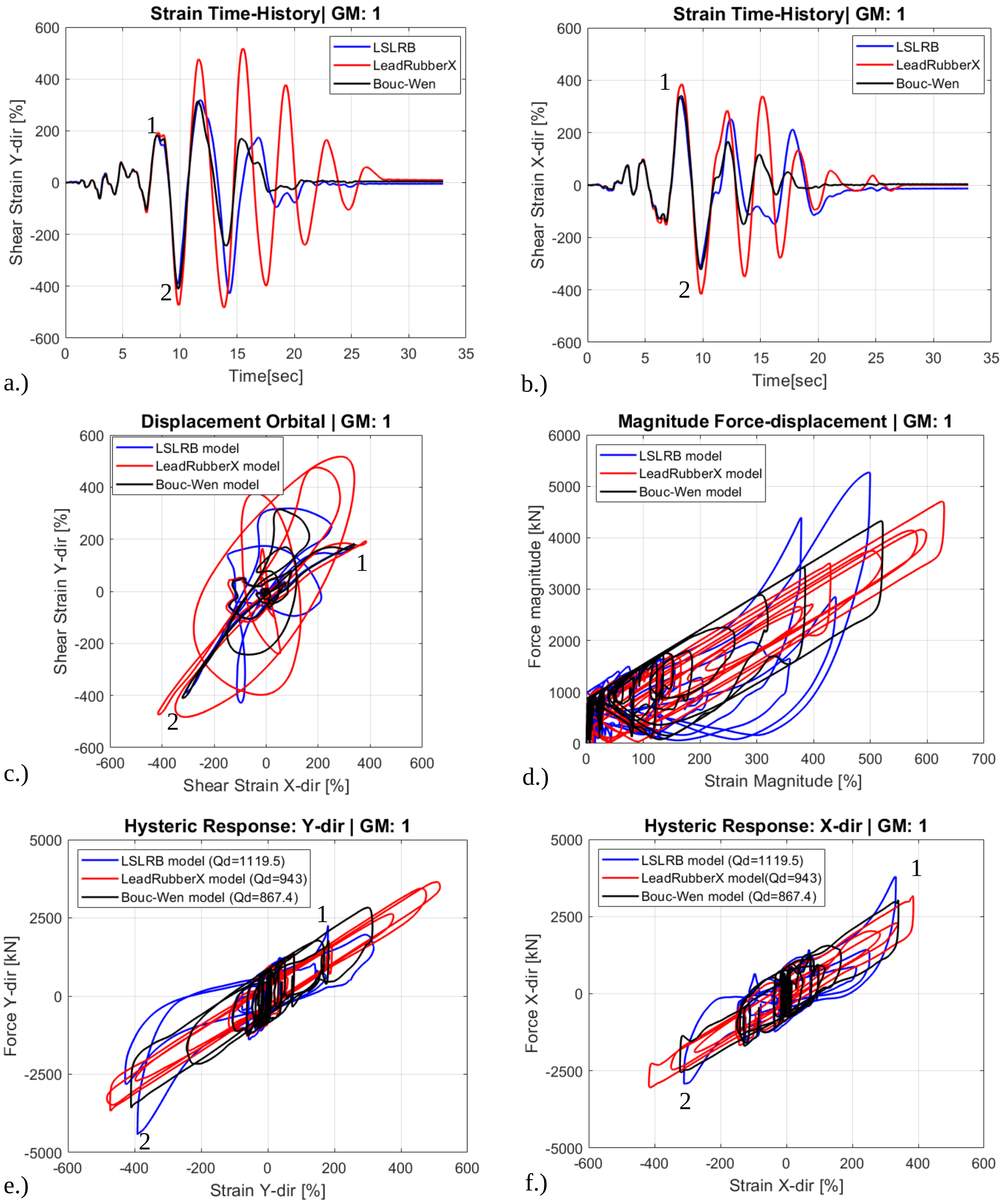

Figure 6-11 BDBE GM1 Kocaeli, Turkey, Izmit: a-b) Displacement time-histories c-d) displacement orbital and magnitude forces e-f) hystereses.

6-6-1 Maximum displacement comparison

In order to evaluate the placement of the moat wall, the 90th percentile displacements are compared for each model at BDBE level ground motions following the USNRC (2014) guidelines (DBE factored by 1.67). The maximum displacements for ground motions 9, 10, 18, and 19 can be considered statistical outliers. Since these ground motions were synthetically created, a few resulted in non-realistic characteristics that contained pulse-like demands at the end of the record Consistent with 1D findings in Chapter 3 and Section 4-6-1, the 2D long duration ground motions result in larger displacements for the *LeadRubberX* model due to heating causing a significant reduction in characteristic strength. Since ground motions 18 and 19 exceeded 500% shear strain for the LSLRB model and underwent instability (failed) then these ground motions are not considered. Considering all 18 ground motions (Figure 6-12), the 90th lognormal percentile displacements for each model were 496%, 716%, and 474% shear strain for the LSLRB model, *LeadRubberX* model, and the Bouc-Wen model, respectively. In comparison, when excluding ground motions 9 and 10, the 90th lognormal percentile displacements for each model were 489%, 687%, and 482% shear strain for the LSLRB model, *LeadRubberX* model, and the Bouc-Wen model, respectively. Importantly, the lower 90th lognormal displacements in the *LeadRubberX* model and the LSLRB model have important implications for ground motions 9 and 10. These models, for ground motions 9 and 10 with the unrealistic pulse towards the end of the record, tend to be sensitive due to the heating effects causing significantly reduced characteristic strength after which undergoing high demands inducing excessive displacements. Similar trend to 1D results from Chapter 4 and 5, provide some consistencies with previous LSLRB model and the updated LSLRB model introduced here. Importantly, considering USNRC guidelines on the moat wall placement or CS, the *LeadRubberX* model would highly overestimate the required CS.

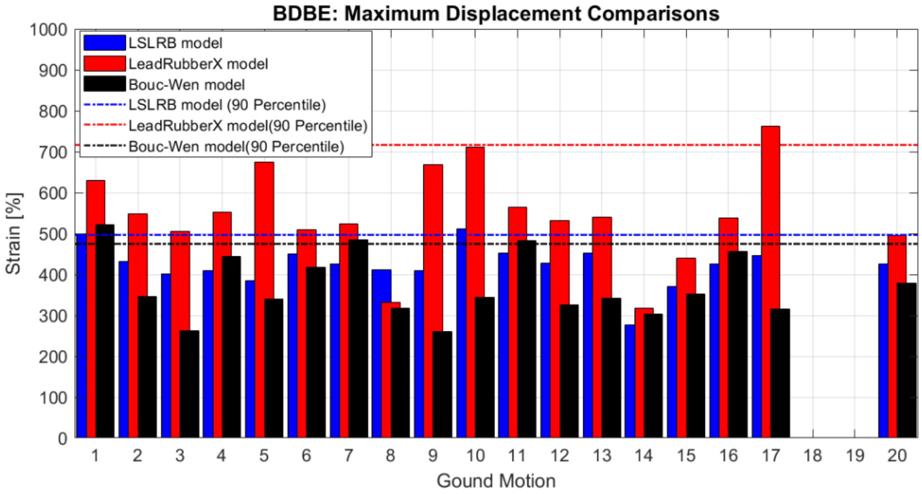

Figure 6-12 BDBE GMs: Maximum displacement comparison for each model.

Impact velocity is a key parameter that significantly amplifies the response of the superstructure and therefore it is an important parameter to accurately predict (Fukui et al. 2020; Masroor and Mosqueda 2012). In Figure 6-13, the average impact velocities for all models at BDBE for various CS are considered where the velocities are obtained in the direction that occurs first (x or y direction). The average impact velocities for lower strain levels tend to be relatively similar between the three models with the Bouc-Wen model obtaining, generally, lower average impact velocities. The LSLRB model tends to be bounded by the two models and only exceeds the impact velocities at 225% and 300% shear strain. The LSLRB model at shear strains of 325% or greater tends to reduce the impact velocities and begins to converge with the Bouc-Wen model. Consistencies with the conclusions of Chapter 4 can be inferred, since the hardening and softening effects occur in a magnitude sense, similar to 1D, extending the moat wall placement to 350-375% shear strain provides potential benefits and extends previous recommendations to 2D analysis. This analysis is useful in suggesting that the moat wall placement may potentially reduce impact velocities by extending the CS to 350-375% shear strain. Extending the moat wall to these levels of strain may be ideal to significantly reduce impact velocities or inducing hardening effects sooner may be beneficial. Comparing the standard deviations (i.e. shown as error bars), the LSLRB model achieved lower standard deviations compared to the other models at almost all levels of shear strain showing less variability.

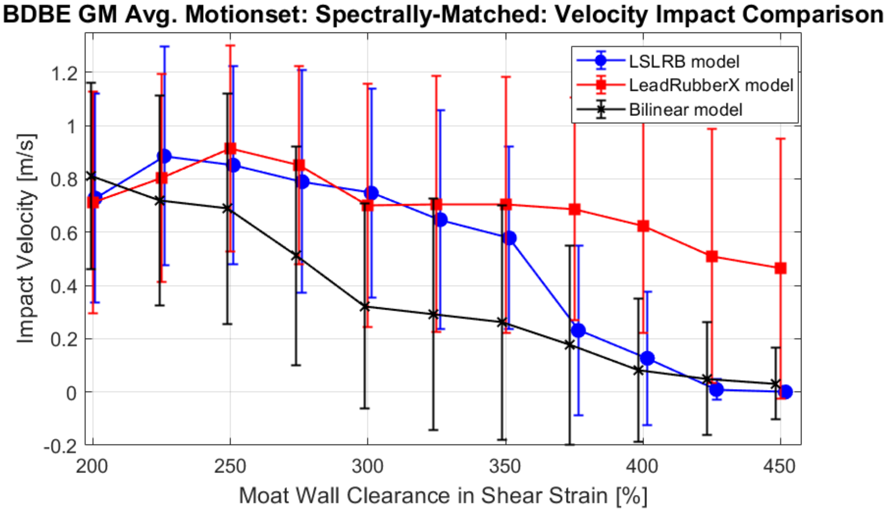

Figure 6-13 BDBE average first impact velocities at various clear to stops (CS)

When excluding ground motions 9 and 10, important deviances in the average impact velocities are observed among the models (Figure 6-14). The exclusion of these ground motions is due to the unrealistic characteristics of these motions caused by these records being synthetically created. The impact velocities follow a similar trend to Figure 6-13, however, the exclusion of these ground motion tends to reduce impact velocities at strains levels of 300% and larger. Particularly, for clearance to stop of 375% shear strain, the impact velocity for the LSLRB model were reduced below the Bouc-Wen model, reaching an average impact velocity lower than 0.2m/s.

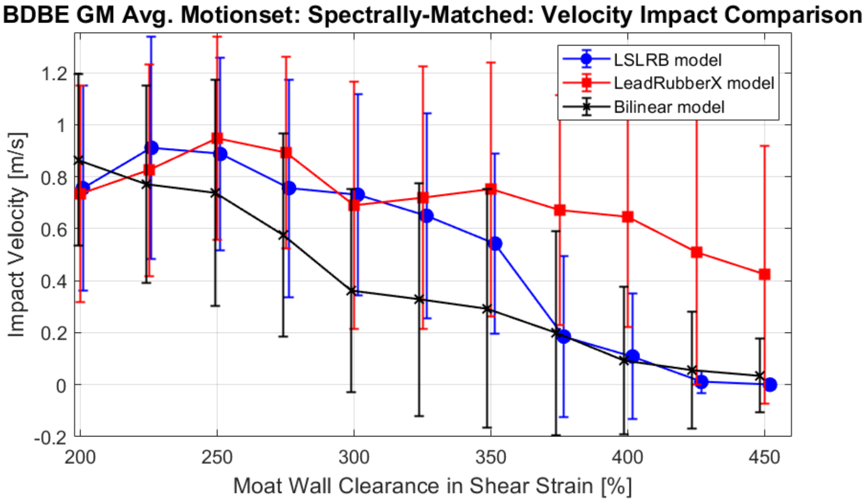

Figure 6-14 BDBE average first impact velocities at various clearance to stops (CS) excluding GMs 9 and 10

6-6-2 Effectiveness of LSLRB model at various intensity levels

To understand the potential benefits of the nonlinear effects of the LSLRB model, the NRC spectrally matched at DBE is increasingly scaled to higher levels of intensity. The calibrated LSLRB model is compared with two other models: the LSLRB model without the rubber nonlinear behaviors (no rubber hardening or softening) and only considering initial lead core hardening and heating, and the LSLRB model with only lead heating (essentially *LeadRubberX model)*. All models are given the same characteristic strength and post-elastic stiffness. This analysis is conducted to observe at which strain demands the LSLRB model engages the nonlinear behaviors that may potentially reduce displacement and impact velocities. In Figure 6-15, the previously NRC spectrally matched DBE ground motions are analyzed however scaled at 1.0, 1.25 and 1.5 in order to observe differences between the models at different intensity levels. The DBE spectra scaled at 1, 1.25 and 1.5 are considered to show the expected demand at each level and the individual ground motion spectra, given the isolation systems fundamental frequency is at ~0.3hz.

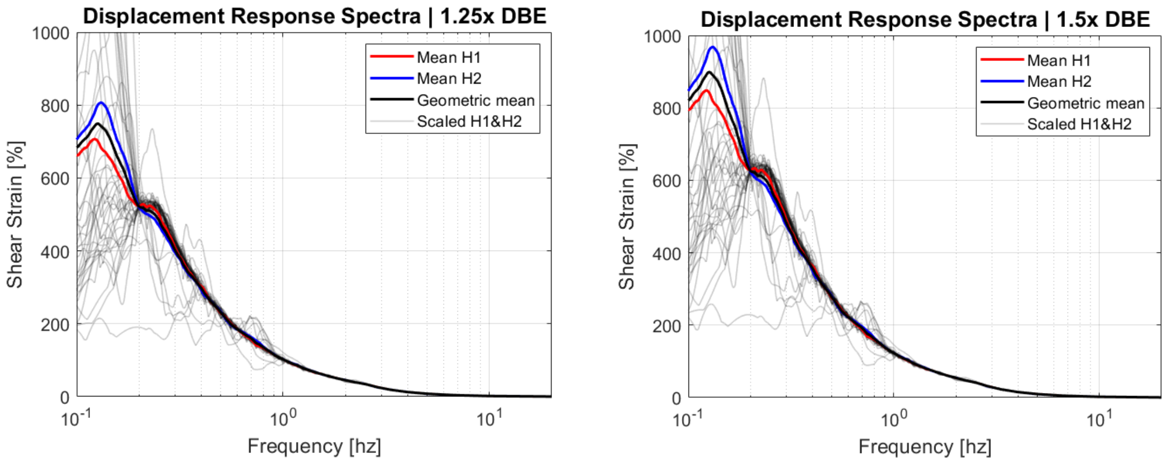

Figure 6-15 NRC spectrally matched DBE scaled at 1.25 and 1.5 scaled to shear strain given the height of rubber h_r=224 mm.

The maximum displacements for the three models are considered at various levels of intensity to observe at which intensity levels the LSLRB model begins to fully engage and provide benefits in reducing displacements (Figure 6-16). For low levels of intensity (i.e. DBE and 1.25xDBE), all the models obtain practically equal displacements (below 200% shear strain). However, for ground motions 4, 7, 8 and 11 which are considered near fault ground motions, the model without initial lead hardening nor rubber hardening obtained lower displacements. Not surprisingly, since all models have the same characteristic strength, the model without the initial lead hardening instantly obtains the actual characteristic strength (i.e. dissipating more energy) and therefore reduces maximum displacements. Meanwhile, the other models with initial lead hardening, commence at a fraction of the characteristic strength then begin to converge to its actual characteristic strength (Figure 6-7). The LSLRB model obtained similar displacements compared to the other models at these low levels of intensity demonstrating that the model is quite predictable and performs as expected. For the intensity level of 1.5, the maximum displacements deviate substantially for the LSRLB model with all nonlinear features, obtaining the lowest 90th lognormal percentile shear strain of 405%. The other models obtained 90th lognormal percentile shear strains of ~460%, demonstrating that the rubber hardening effects become significantly more important to model at these higher levels of intensity. The LSLRB model significantly reduced shear strains compared to the other models, showing that capturing the various behaviors as previously described are critical, otherwise inappropriate CS will be obtained.

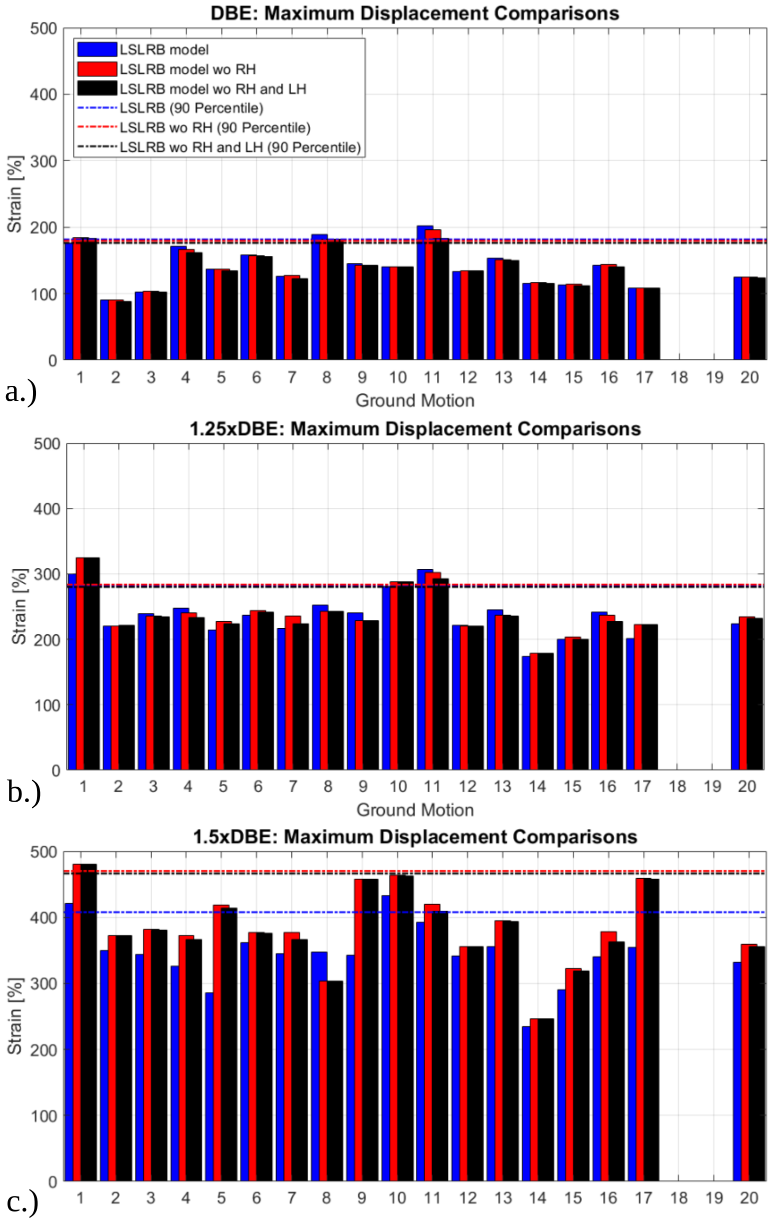

Figure 6-16 Maximum displacement for all three models at three levels of intensity a.)1xDBE b.)1.25xDBE c.)1.5xDBE for the LSLRB model, the LSLRB model without rubber hardening(RH), and the LSLRB model without rubber hardening(RH) and without lead hardening (LH)

The impact velocity for the three models at three levels of intensity are evaluated to compare at which levels of intensity the LSLRB model may reduce impact velocities (Figure 6-17). For DBE, all models achieved impact at low levels of shear strain ranging from 100-175% and obtained identical impact velocities. For a scale factor of 1.25, the impacts occurred at intermediate shear strains ranging from 200-275%. Furthermore, similar to DBE level, the impact velocities are practically equivalent which demonstrates consistency between the models and that the hardening effects are essentially not engaged for the LSLRB model. For DBE scaled at 1.5, the demands begin to increase and hardening effects for the LSLRB model begin to engage at higher levels of shear strain. For shear strain levels of 300%, the LSLRB model begins to diverge and reduce impact velocities. At shear strain levels of 350%, the LSLRB model demonstrates significant benefits in reducing the impact velocities obtaining an average impact velocity of 0.02 m/sec. Comparatively, the other models that do not include rubber hardening effects and obtained impact velocities of ~0.24 m/sec. Thus, the LSLRB model clearly demonstrates its capability in reducing impact speeds, reducing by a factor of 10 for the CS of 350% shear strain.

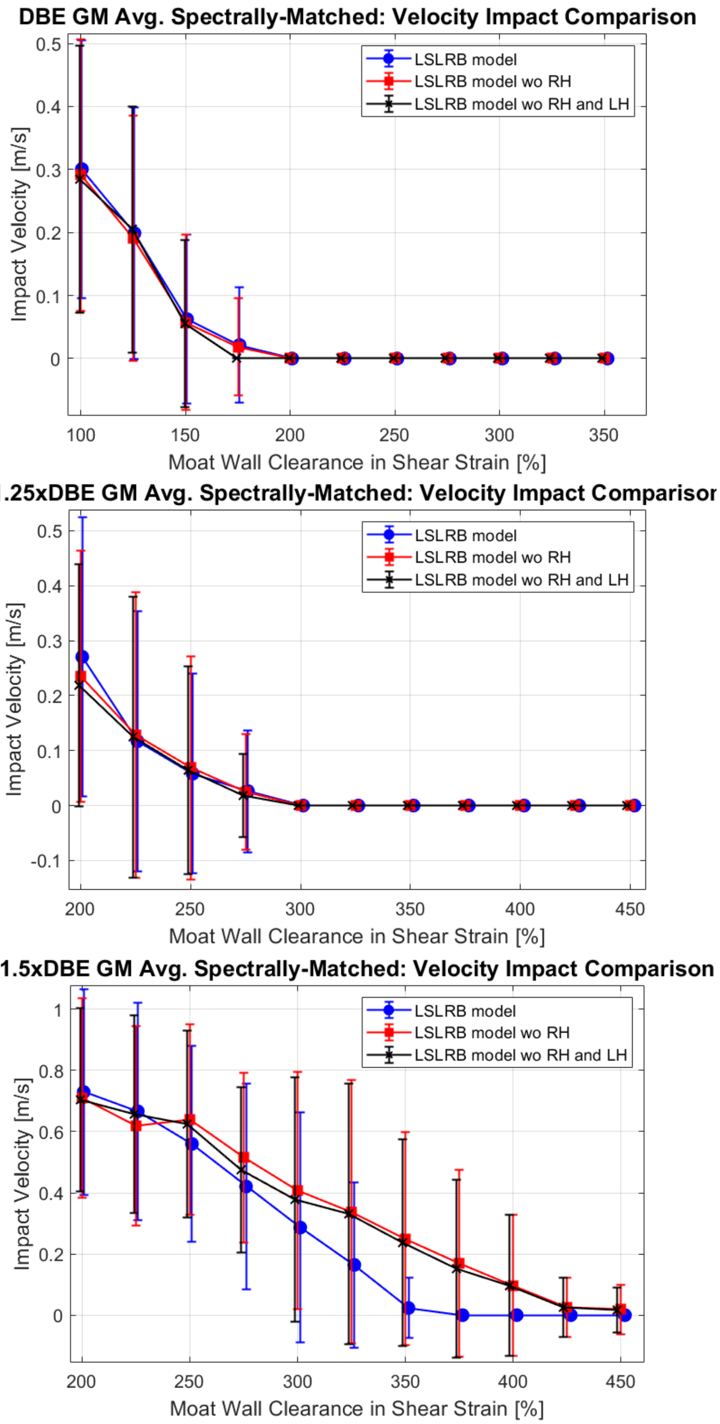

Figure 6-17 Impact velocity for three levels of intensity DBE, 1.25DBE, and 1.5DBE

6-7 Conclusion

The bidirectional large strain lead rubber bearing (LSLRB) model is proposed in this chapter and is examined in detail. The LSLRB model is able to capture the various nonlinear behaviors at varying strain levels exhibited in 1D and 2D experimental data at a given axial load with one set of parameters, however a change in size of the bearing or variance in the axial load will require recalibration of the model. The model is composed of a hyperelastic component and a hysteretic component. Commonalities between the natural rubber, found in LRBs, and the high damping rubber were drawn in order to accurately model the LSLRB model to experimental data. Previous work has shown that natural rubber and high damping rubber behave similarly only at different strain levels and that the former is, for earthquake purposes, rate independent. Thus, the previous LSLRB model was extended by using an anisotropic HDR damage model. The damage model was modified due to a sensitivity study conducted, identifying the need for strain rate independence and extracting unnecessary parameters for behaviors observed experimentally in the LRB.

A NLRHA is performed on the LSLRB model and compared with other models used in practice such as the Bouc-Wen and *LeadRubberX* model. When comparing these three models at BDBE intensity levels, the *LeadRubberX* model tends to highly overestimate the impact velocities and maximum displacements compared to the LSLRB model. The placement of the moat wall when following NRC guidelines resulted in 496%, 716% and 474%, shear strain for the LSLRB, *LeadRubberX*, and the Bouc-Wen model, respectively. Therefore, the placement of the wall would either be significantly extended beyond or obtain an inadequate clearance, compared to LSRLB model. As for the average impact velocities, the LSLRB model tends to diverge from the other models at shear strain levels of 325%, with the most significant reduction in average impact velocities occurring at 350-375% shear strain. The impact velocities for the LSLRB model began reducing at shear strain levels of 350%, implicating possible extensions of typical moat wall placements to these levels, demonstrating consistencies with 1D studies conducted in Chapter 4.

Different levels of intensity for NRC spectrally matched ground motions were conducted on the LSLRB model in order to observe when the model is deviates from the response compared to *LeadRubberX* and LSLRB model without rubber hardening. All models were set to an equivalent post-elastic stiffness and characteristic strength for comparison. For low levels of intensity (i.e. factor of 1.0 and 1.25), the LSLRB model was consistent with that of *LeadRubberX* and the LSLRB model without rubber hardening. Importantly, when comparing the highly nonlinear behavior of HDR bearings, at even low levels of strain the HDR exhibits nonlinear behaviors which can create some uncertainty and can be impractical for designers. Therefore, the consistency of LSLRB model at low to intermediate levels of shear strain compared to typical models, along with being able to capture the nonlinear effects for BDBE level ground motions may be desirable for use in practice. At higher levels of intensity (i.e. factor of 1.5) the model proved to reduce the 90th percentile maximum displacements based on USNRC guidelines. Reductions from 460% to 406% shear strain were obtained when comparing the LSLRB model without rubber hardening to the LSLRB model. The impact velocities at 300% shear strain began to significantly reduce impact velocities with the most significant reduction being at 350% shear strain reducing the impact velocities by a factor of 10 compared to the other models.

6-8 References

An, G., Kim, M., Jung, J.-W., Mosqueda, G., and Marquez, J. F. (2020). “Evaluation of Clearance to Stop Requirements in A Seismically Isolated Nuclear Power Plant.” *Energies*, 13(22), 6156.

Clark, P. W., Aiken, I. D., and Kelly, J. M. (1997). *Experimental studies of the ultimate behavior of seismically-isolated structures. Technical Report EERC-97-l8, Earthquake Engineering Research Center*, Berkeley, CA.

Dafalias, Y. F., and Popov, E. P. (1975). “A model of nonlinearly hardening materials for complex loading.” *Acta Mechanica*, 21(3), 173–192.

Diani, J., Fayolle, B., and Gilormini, P. (2009). “A review on the Mullins effect.” *European Polymer Journal*, Elsevier Ltd, 45(3), 601–612.

Eem, S., and Hahm, D. (2019). “Large strain nonlinear model of lead rubber bearings for beyond design basis earthquakes.” *Nuclear Engineering and Technology*, 51(2), 600–606.

Freund, M., and Ihlemann, J. (2010). “Generalization of one-dimensional material models for the finite element method.” *ZAMM Zeitschrift fur Angewandte Mathematik und Mechanik*.

Fukui, H., Fujitani, H., Mukai, Y., Ito, M., and Mosqueda, G. (2020). “Response Evaluation and Analysis Using Impulse of Base-isolated Buildings during a Collision with Retaining Wall.” *Architectural Institute of Japan, Japan Architectural Review*, 66B(3).

Grant, D. N., Fenves, G. L., and Whittaker, A. S. (2004). “Bidirectional Modelling of High-Damping Rubber Bearings.” *Journal of Earthquake Engineering*, 8(1), 161–185.

Harwood, J. A. C., Mullins, L., and Payne, A. R. (1965). “Stress softening in natural rubber vulcanizates. Part II. Stress softening effects in pure gum and filler loaded rubbers.” *Journal of Applied Polymer Science*, 9(9), 3011–3021.

Harwood, J. A. C., and Payne, A. R. (1966a). “Stress softening in natural rubber vulcanizates. Part III. Carbon black-filled vulcanizates.” *Journal of Applied Polymer Science*.

Harwood, J. A. C., and Payne, A. R. (1966b). “Stress softening in natural rubber vulcanizates. Part IV. Unfilled vulcanizates.” *Journal of Applied Polymer Science*, 10(8), 1203–1211.

Ishida, K., Shiojiri, H., Iizuka, M., Mizukoshi, K., and Takabayashi, K. (1991). “Failure Tests of Laminated Rubber Bearings.” *Proceedings of the 11th international conference on structural mechanics in reactor technology*, IASMiRT, Tokyo,Japan, 241–246.

Kalpakidis, I. V., and Constantinou, M. C. (2009). “Effects of Heating on the Behavior of Lead-Rubber Bearings. I: Theory.” *Journal of Structural Engineering*, 135(12), 1440–1449.

Kikuchi, M., Nakamura, T., and Aiken, I. D. (2010). “Three-dimensional analysis for square seismic isolation bearings under large shear deformations and high axial loads.” *Earthquake Engineering & Structural Dynamics*, 39(13), 1513–1531.

Koh, C. G., and Kelly, J. M. (1988). “A simple mechanical model for elastomeric bearings used in base isolation.” *International Journal of Mechanical Sciences*, 30(12), 933–943.

Kumar, M., Whittaker, A. S., and Constantinou, M. C. (2014). “An advanced numerical model of elastomeric seismic isolation bearings.” *Earthquake Engineering & Structural Dynamics*, 43(13), 1955–1974.

Lagarias, J. C., Reeds, J. A., Wright, M. H., and Wright, P. E. (1998). “Convergence properties of the Nelder-Mead simplex method in low dimensions.” *SIAM Journal on Optimization*, 9(1), 112–147.

Masroor, A., and Mosqueda, G. (2012). “Experimental simulation of base-isolated buildings pounding against moat wall and effects on superstructure response.” *Earthquake Engineering & Structural Dynamics*, 41(14), 2093–2109.

Ragni, L., Tubaldi, E., Dall’Asta, A., Ahmadi, H., and Muhr, A. (2018). “Biaxial shear behaviour of HDNR with Mullins effect and deformation-induced anisotropy.” *Engineering Structures*, 154, 78–92.

Ryan, K. L., Kelly, J. M., and Chopra, A. K. (2005). “Nonlinear Model for Lead–Rubber Bearings Including Axial-Load Effects.” *Journal of Engineering Mechanics*, 131(12), 1270–1278.

Sanchez, J., Masroor, A., Mosqueda, G., and Ryan, K. (2013). “Static and dynamic stability of elastomeric bearings for seismic protection of structures.” *Journal of Structural Engineering (United States)*, 139(7), 1149–1159.

Sarebanha, A., H. Schellenberg, R., J. Schoettler, M., Mosqueda, G., and A. Mahin, S. (2019). “Real-Time Hybrid Simulation of Seismically Isolated Structures with Full-Scale Bearings and Large Computational Models.” *Computer Modeling in Engineering & Sciences*, 120(3), 693–717.

Schellenberg, A., Baker, J., Mahin, S., and Sitar, N. (2014). *Investigation of Seismic Isolation Technology Applied to the APR 1400 Nuclear Power Plant-Volume 2: Selection of Ground Motions. Technical Report to KEPCO Engineering and Construction, Pacific Engineering Research Center, University of California, Berkeley, CA.*

Sheridan, P. M., James, F. O., and Miller, T. S. (2012). "Design of Components." *Engineering with Rubber*, A. N. Gent, ed., Carl Hanser Verlag GmbH & Co. KG, München, 259–293.

Tubaldi, E., Ragni, L., Dall'Asta, A., Ahmadi, H., and Muhr, A. (2017). "Stress softening behaviour of HDNR bearings: modelling and influence on the seismic response of isolated structures." *Earthquake Engineering & Structural Dynamics*, 46(12), 2033–2054.

U.S. Nuclear Regulatory Commission. (2014). "Design Response Spectra for Seismic Design of Nuclear Power Plants." *Regulatory Guide No. 1.60, Revision 2*.

Vemuru, V. S. M., Nagarajaiah, S., and Mosqueda, G. (2016). "Coupled horizontal-vertical stability of bearings under dynamic loading." *Earthquake Engineering and Structural Dynamics*, 45(6), 913–934.

Warn, G. P., Whittaker, A. S., and Constantinou, M. C. (2007). "Vertical Stiffness of Elastomeric and Lead–Rubber Seismic Isolation Bearings." *Journal of Structural Engineering*, 133(9), 1227–1236.

Wei, W., Yuan, Y., Igarashi, A., Zhu, H., and Luo, K. (2020). "Generalized hyper-viscoelastic modeling and experimental characterization of unfilled and carbon black filled natural rubber for civil structural applications." *Construction and Building Materials*, Elsevier Ltd, 253, 119211.

Yamamoto, M., Shigeo, M., Masahiko, H., HamaGuchi, H., Hideo, K., Takayuki, S., and Harumi, Y. (2009). "Performance tests of full size rubber bearings for isolated superhigh-rise buildings." *JSSI 15th Anniversary International Symposium on Seismic Response Controlled Buildings for sustainable Society*, Tokyo, Japan.

Chapter 7 SUPERSTRUCTURE RESPONSE WITH 2-D LSLRB MODEL

7-1 Introduction

The nonlinear bi-directional large strain lead rubber bearing (LSLRB) model examined in Chapter 6 is implemented in a full-scale nuclear power plant (NPP) model described in Chapter 5 in order to investigate various LRB models and the effects it may have on the response of the superstructure. NPPs are critical structures that are required to account for a high-risk low frequency seismic occurrence in order to verify the response of the superstructure and the isolation system. Recent research has examined that the isolator capacity should be extended beyond current design code standards (Shao et al. 2017), along with other studies that also extended the capacity of bearings and observed stiffening effects and restraints reduced the probability of collapse (Kitayama and Constantinou 2019a). When considering 2-D, the moat wall clearance is typically measured perpendicular to the base-mat and therefore due to geometric constraints, such as corners, the geometric strain developed at the corners may develop nonlinear effects even for moderate strain levels of clearances. Whether new isolated structure systems explore extending the clearance to stop (CS) to reduce the probability of collapse or unforeseen geometric strains in already existing isolated structures; the need for capable numerical models that capture the nonlinear behaviors at these large displacements are critical.

To limit the occurrence of impact to moat walls, current design standards for NPPs specify for the minimum required CS to be placed at the 90th percentile horizontal displacement for Beyond Design Basis Earthquake (BDBE) shaking (ASCE 2017a). Bearings are required to be tested to the CS displacements under the expected axial load. The United States Nuclear Regulatory Commission (USNRC 2014) requires for isolation systems to model the shear forces developed at BDBE demands. In the previous chapters, it has been demonstrated that under BDBE ground motions the LRB models undergo large strain levels. The LSLRB model obtained reduced displacements and impact velocities due to rubber hardening, higher characteristic strength calibration, and softening ‘unloading’ effects when compared to other LRB models used in practice. In Chapter 6, the LSLRB model proved to be consistent with models used in practice at low levels of intensity, with addition to, being able to capture all nonlinear behaviors at larger levels of intensity.

The velocity at impact to moat walls is the key parameter for impact forces and the amplification of the structure response, as found via experimental tests (Fukui et al. 2020; Masroor and Mosqueda 2012), therefore estimation of the impact velocity is critical for these analyses. ASCE 4 (2017) requires explicit analysis of the isolated structure system for impact loading if the provided clearance is less than the required CS, with little guidance provided for procedures to model or mitigate the effects of impact. The benefits of using the LSLRB model is demonstrated in terms of estimating isolator displacements and capturing the impact velocity as the isolation system exceeds the CS. When the CS is exceeded, an extension to Sarebanha et al. (2021) moat wall impact model, proposed in Chapter 5, is examined.

7-2 Nonlinear Time-History Response of NPP

The calibrated LSLRB model from Chapter 6 was implemented into the Archetype Nuclear Type (ANT) model, based on the APR 1400 NPP (Schellenberg et al. 2016), to evaluate various bearing models. A nonlinear response history analysis (NLRHA) of the LSLRB model is conducted to observe potential benefits of allowing hardening and softening effects to occur by extending the moat wall to higher levels of strain, in addition to, observing the effects it may have on the superstructure. The bidirectional behavior of the model is observed in these analyses to evaluate the coupled hardening effects that may be capable in mitigating base-mat rotations before impact. The NLRHA is conducted on the LSLRB model to observe any potential setbacks such as amplification of the superstructure accelerations or increases in base shear. The LSLRB model is compared against LRB models used in practice such as the Bouc-Wen smooth bilinear model and the recently proposed *LeadRubberX* model. The models were initially set to the same design parameters such as the post elastic stiffness and characteristic strength, after which calibration to experimental data were conducted (more details in Chapter 4). The ground motions used for analysis are NRC spectrally matched at DBE (Schellenberg et al. 2014) and factored by 1.67 to obtain beyond design basis earthquake (BDBE), having a return period of 100,000 years.

7-2-1 Bearing response

In order to understand the behavior of each model, the bearing response is observed in detail for one record. The response to 1999 Kocaeli, Turkey, Izmit or ground motion 1 (GM1) at

BDBE, is examined in order to compare the hysteresis and displacement trajectories for the three models (Figure 7-1). Considering that the response is bidirectional, it is important to note that the hyperelastic component of the LSLRB model is highly dependent on the displacement in a magnitude sense (see Section 6-3-2-1). Therefore, when considering hysteresis from a particular direction, the results may seem unfeasible, however after examining the response in a magnitude sense provides more interpretable results. The LSLRB model can be seen to obtain lower magnitude shear strains compared to the other models. The softening and hardening effects can be observed to take full effect for both the x and y directions. In the y-direction, the LSLRB model obtains a 50% softening effect of the hysteresis at the second cycle compared to the initial cycle. These softening effects, particularly for these strains, have been previously observed (Harwood and Payne 1966b). Importantly, initially the displacement orbitals are similar compared to the other models, however as hardening and softening occurs in the rubber, the trajectory of the LSLRB model begins to deviate from the other models.

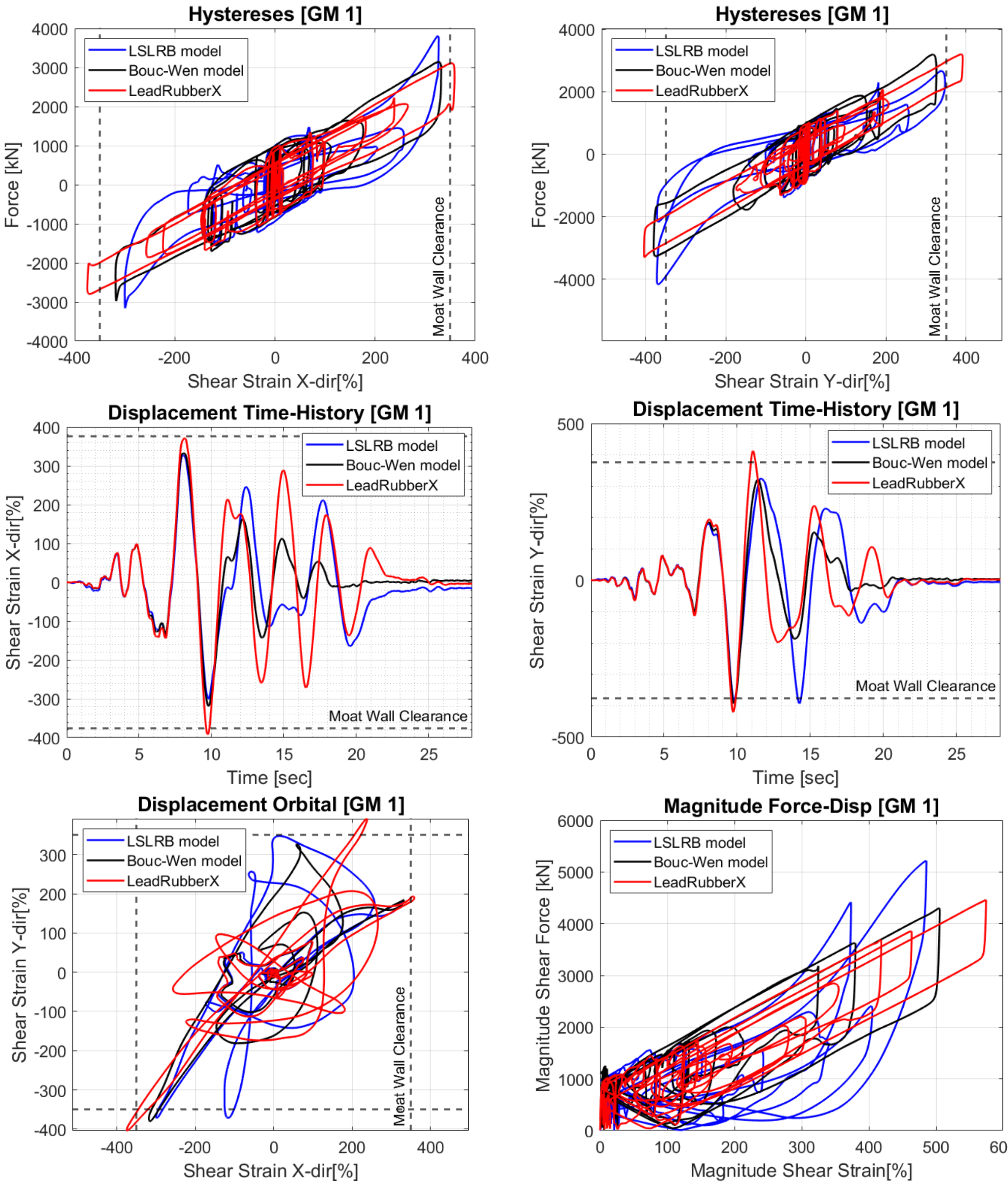

Figure 7-1 Individual record response (GM 1: 1999 İzmit earthquake)

The maximum displacements for all three models are examined for all ground motions at BDBE (Figure 7-2). Certain ground motions are unrealistic ground motions (i.e. 9, 10, 18 and 19), the ground motions are long duration and have unrealistic characteristics due to being synthetically modified (Schellenberg et al. 2014), since similar results were found in Chapter 6 when comparing with and without unrealistic ground motions, they are extracted in this analysis. In Chapter 4 and 5 of this dissertation, a similar analysis with the same ground motion set were conducted and similar conclusions are obtained here. When extending these results for 2D simulations, the models tend to obtain similar results to 1D further providing consistency among 1D and the updated 2D LSLRB model. When considering all the ground motions, the lognormal 90th percentile displacements based on Kumar et al. (2015) resulted in 647%, 461% and 399% shear strain for the *LeadRubberX*, LSLRB, and the Bouc-Wen model, respectively. When excluding the unrealistic ground motions, the lognormal 90th percentile displacements resulted in 565%, 414% and 409% for the *LeadRubberX*, LSLRB, and the Bouc-Wen model, respectively (Figure 7-2). For the *LeadRubberX* or Bouc-Wen model, the CS would either be extended far beyond required or less than required when compared to the LSLRB model.

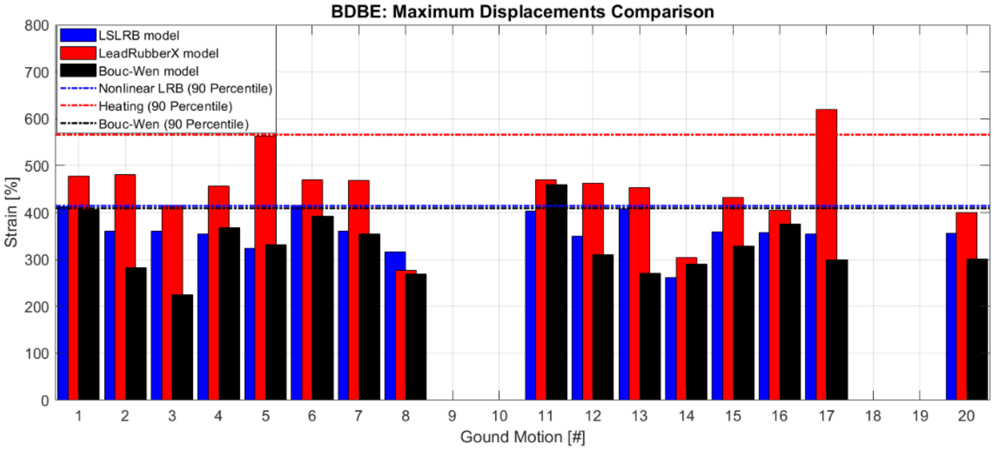

Figure 7-2 BDBE maximum displacements excluding unrealistic ground motions

7-2-2 Torsional effects

Base isolation has been known to be an effective method to reduce the influence of asymmetry (i.e. eccentricity in the center of mass, stiffness, or strength) that may exist within a structure (Lee 1980). Torsional effects may be important to consider if these effects are excessive, especially for impact, as impact tends to excite torsional effects (Sarebanha 2018). The maximum base-mat rotations are compared between the three LRB models to observe any potential benefits the hardening effects of the LSLRB model may have in reducing base-mat rotational effects. The maximum rotations for each BDBE ground motion are examined by subtracting the difference between two adjacent corner displacements of the base mat divided by the distance, thereupon the maximum rotation from each record is plotted in Figure 7-3. Note, ground motion 18 is not considered since the LSLRB model underwent an excessive rotation due to exceeding the calibrated maximum 500% shear strain and failed obtaining a restoring force of zero. When comparing the ground motions, no significant benefits can be observed, however it can be deduced that the nonlinear effects in the LSLRB model do not amplify any torsional effects compared to the other models, and in fact, at some instances reduce torsion.

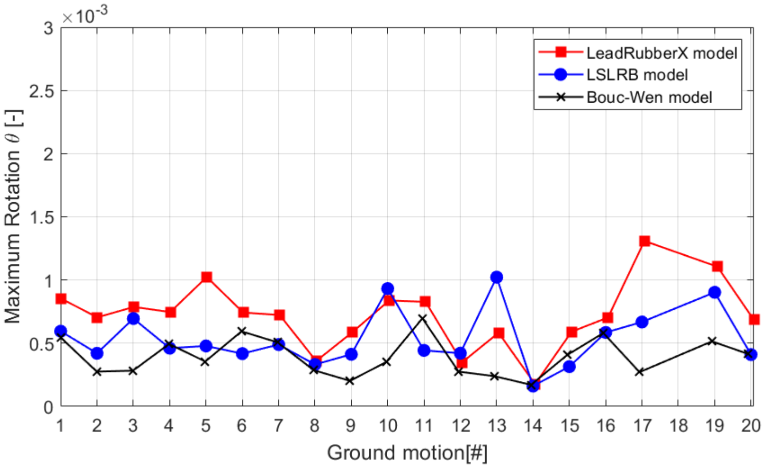

Figure 7-3 Record-to-record maximum rotations comparison between LRB models

7-2-3 Base Shear comparison

The hardening effects of the LSLRB model provide the need to analyze the potential increases in base shear forces that may develop compared to other LRB models. The base shear forces are transferred from the isolation system to the superstructure, and could have an effect on the accelerations experienced. The maximum normalized base shear forces for all three models are analyzed without a moat wall to first observe the pure bearing response (Figure 7-4). It can be observed that the LSLRB model does obtain larger normalized base shear values for 9 of 20 ground motions, with the maximum normalized base shear of 0.42 for ground motion 1. The LSLRB model obtained the largest maximum normalized base shear for ground motion 8, being about ~40% greater than the other models. In some cases, the *LeadRubberX* model obtained larger shear forces due to the large displacements that result from the analysis. Nevertheless, it is important to consider whether accounting for these variations in base shear are more favorable than accounting for the amplification of base shear due to impact, which has been found to cause detrimental effects on the superstructure.

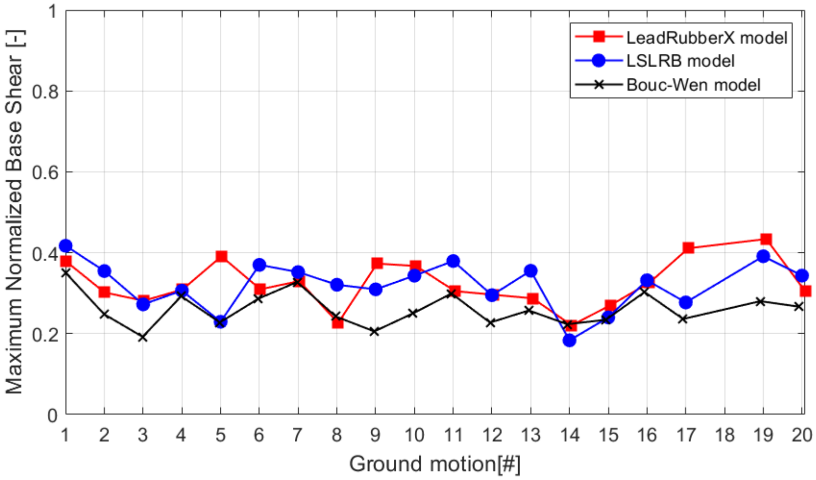

Figure 7-4 Normalized base shear comparison between LRB models

7-2-4 Response of the superstructure considering no moat wall

The average response spectra of the Reactor Containment Building (RCB) are considered for all three models with no moat wall in order to observe any differences between the models and the effects they may have on the superstructure (Figure 7-5). Two peaks can be observed for all models at the fundamental frequency of the isolation system (~0.3hz) and at the fundamental frequency of the RCB (~3.5hz). Importantly, although the LSLRB model accounts for hardening effects, the model does not amplify the acceleration of the RCB when compared to the other models. For the *LeadRubberX* model, the amplification at the fundamental frequency of the isolation system can be observed to reach about ~2g. This amplification may be due to the heating effects and synthetic motions creating large demands on the *LeadRubberX* model causing large degradations, resulting in the model resembling a linear spring, thus creating a large narrow amplitude at the time period of the isolation system. The LSLRB model at the fundamental frequency of the RCB results in reduced floor spectral accelerations compared to the Bouc-Wen model.

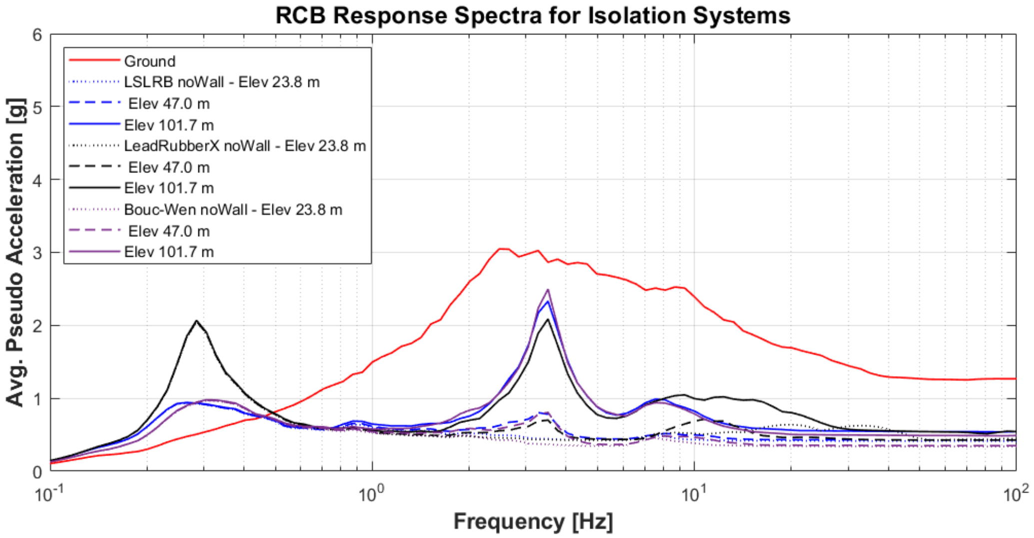

Figure 7-5 Average 2-D floor response spectra of RCB for 20 GMs with no moat wall.

7-2-5 Response of the superstructure considering moat walls

The average pseudo response spectra are considered for various CS for all three models in order to observe any potential benefits of the LSLRB model (Figure 7-6). Important implications can be observed at the fundamental frequency of the RCB as the CS increases from 325% to 375% shear strain, the LSLRB model significantly reduces the average pseudo response spectra from ~4.3g to 2.8g resulting in a decrease of 35%. Comparatively, the other models experience far less reductions when the wall is extended, obtaining reductions of less than 15%. At 375% shear strain, the LSLRB model reduces acceleration levels equivalent to the Bouc-Wen model which has no reduction in lead core shear strength (i.e. no lead core heating). Importantly, considering extending the moat wall and modeling of the nonlinear behaviors exhibited by LRBs have benefits of reducing the response of the superstructure.

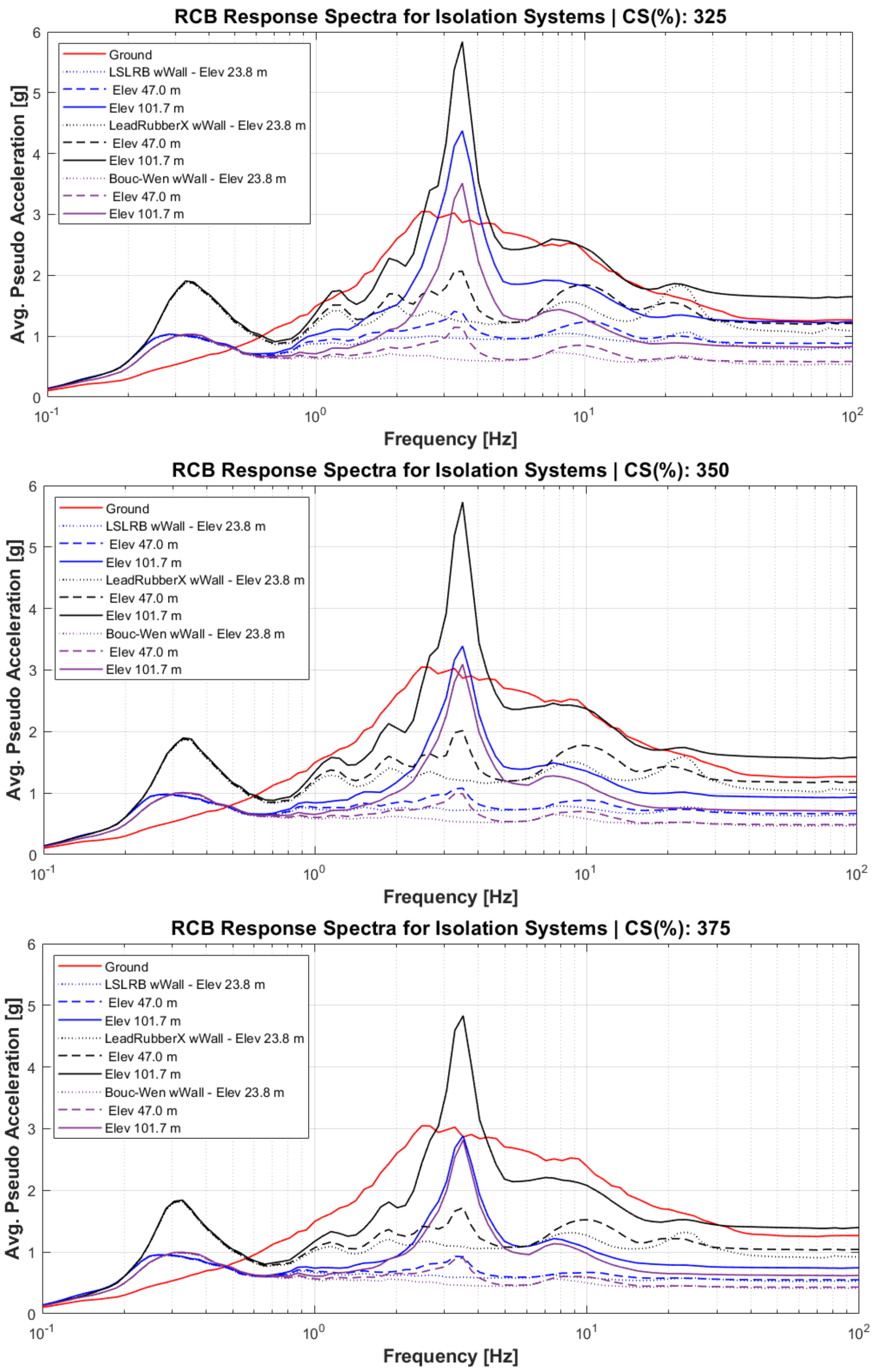

Figure 7-6 Average 2-D floor response spectra of RCB for 20 GMs at CS 325%, 350%, and 375% shear strain.

7-2-6 Impact Evaluation

As previously mentioned, impact can attribute to the amplification of the superstructure response. Therefore, examining the amount of impacts each model obtains is important to understand their ability in reducing the number of impacts. All ground motions, apart from the unrealistic ground motions, were considered when analyzing the total number of impacts (including subsequent impacts) with the moat wall placed at three levels of shear strain 325%, 350%, and 375% (Figure 7-7). Important implications can be realized from this analysis, primarily, that the *LeadRubberX* resulted in excessive number of total impacts (i.e. 325% shear strain). The reason for the excessive impacts may be due to the sensitivity the *LeadRubberX* model has from the long duration ground motions, undergoing excessive strength degradation and consequently larger displacements resulting in excessive impacts. The LSLRB model which includes all nonlinear behaviors, in particular rubber hardening, produce evident reductions in the number of impacts especially for 350% shear strain and greater, at which point the rubber hardening is fully engaged. At a CS of 375% shear strain, the LSLRB model reduces the number of impacts comparable to the number of impacts obtained by the constant Bouc-Wen model.

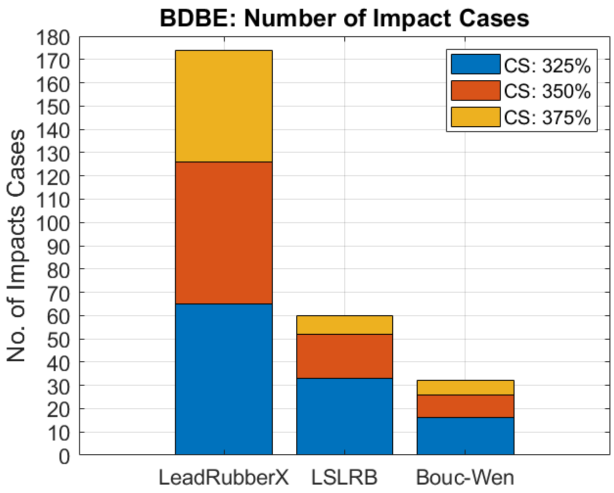

Figure 7-7 Total number of impacts for each model at CS 325%, 350%, and 375% shear strain

To further elucidate the benefits of the LSLRB model, an average response of the three models considering the first three impacts are analyzed for BDBE ground motions (Figure 7-8a-Figure 7-8e). Overall, for the *LeadRubberX* model, the average impact velocities are highly overestimated with comparison to the other LRB models. The LSLRB model tends to be bounded by the Bouc-Wen model and the *LeadRubberX* model. For moderate levels of shear strain (i.e. 300-325%), the LSLRB model does not fully develop its hardening effects and therefore does not significantly reduce impact velocities lower than the Bouc-Wen model. However, the LSLRB model obtains a lower average impact velocity compared to the *LeadRubberX* model which can be mainly attributed to the LSLRB model capturing the initial lead hardening capturing the actual characteristic strength (Chapter 4). For large levels of shear strain (i.e. 350%- 400), the LSLRB model is bounded by both models and can be attributed to the hardening effects reducing the impact velocities. A comparison with and without the unrealistic ground motions are conducted to evaluate the effects these motions may have. For CS 350% shear strain, the LSLRB model tends to converge to the Bouc-Wen model, mainly for the exclusion of the unrealistic ground motions (Figure 7-8c). For CS of 350% shear strain (Figure 7-8b), the LSLRB model obtained lower average impact velocities than the Bouc-Wen model with less deviation. Considering the first impact velocities for the exclusion of unrealistic ground motions at 375% shear strain (Figure 7-8d), the LSLRB model reduced the average impact velocities lower than the Bouc-Wen model and obtained lower deviations. For the third impacts, the LSLRB model tends to quickly converge to the Bouc-Wen model, more so, for ground motions excluding the unrealistic ground motions (Figure 7-8e). Extending the CS to 350-375% shear strain results in achieving the lowest impact velocities.

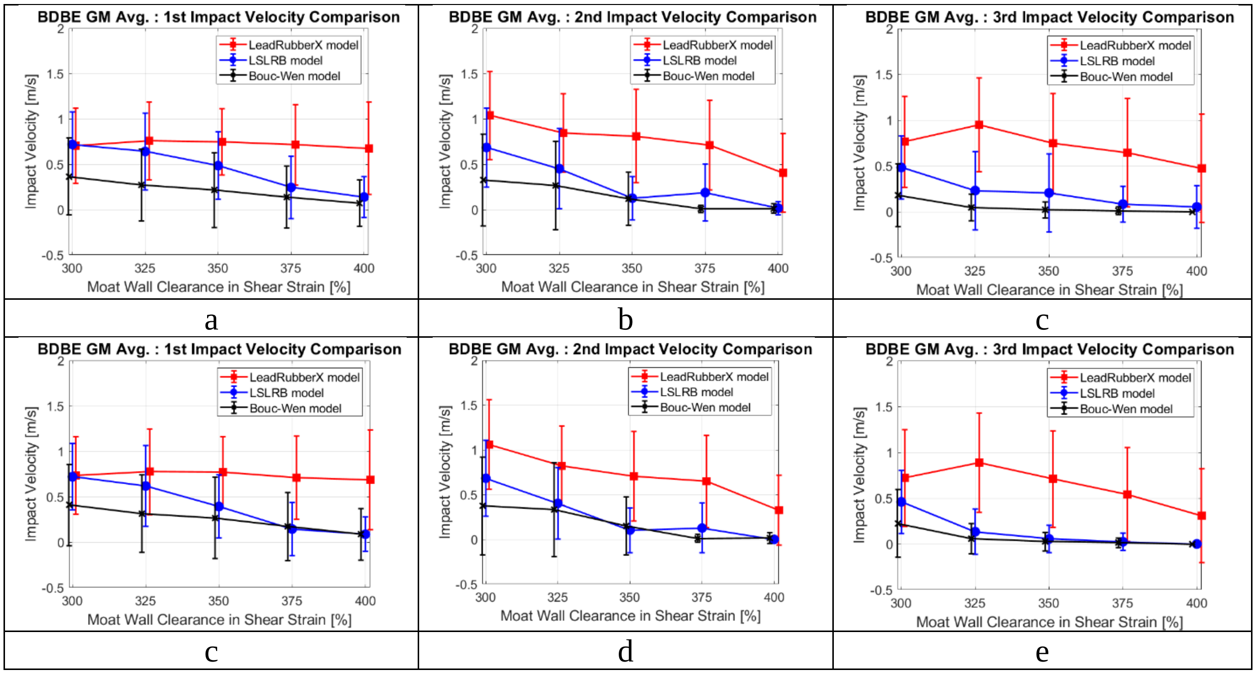

a b c

c d e

Figure 7-8 Avg. impact velocity for 20 GMs versus moat wall clearance, **(a-c)** all ground motions, **(c-e)** excluding unrealistic ground motions: **(a,c)** 1st impact, **(b,d)** 2nd impact, **(c,e)** 3rd impact

7-2-6-1 Penetration impact velocity prediction

The moat wall should be analyzed and designed for impact loading if the CS is smaller than specified as per ASCE 4-16 (2017). In this case, impact velocity may be calculated either by analysis for BDBE ground motions or by assuming cyclic response of the isolated superstructure to the 95 percentile BDBE displacement at a calculated frequency for the isolation system (ASCE 2017a).

In Chapter 5, an extension of a moat wall deformation prediction model was proposed, the model obtained a relationship between the impact velocity and the amount of moat wall deformation. Therefore, accurate modeling of the LRB is critical to obtain a better estimate of the velocity at impact, and consequently obtain a better estimate of the amount of deformation that needs to be accounted for by the isolation system. In Figure 7-9, the recommended design moat wall deformation prediction model described in Chapter 5 is utilized and plotted against the OpenSees simulations considering the first impacts at different levels of CS for all three models. Scenario 2 failure mechanism is assumed for this particular moat wall, as described in Chapter 5, with the inclusion of the backfill soil along with the recommended restitution value of 0.7. The moat wall deformation prediction model resulted in a conservative prediction of the amount of deformation of the moat wall obtained by the OpenSees simulations. Importantly, in some instances, a detailed model with the inclusion of the moat wall may not be required since a SDOF system can be analyzed to obtain the impact velocity. This can potentially be utilized to predict the amount of moat wall deformation and obtain the maximum displacement the isolation system may need to account for. However, it is important for more analysis to be conducted since this is one configuration of a moat wall.

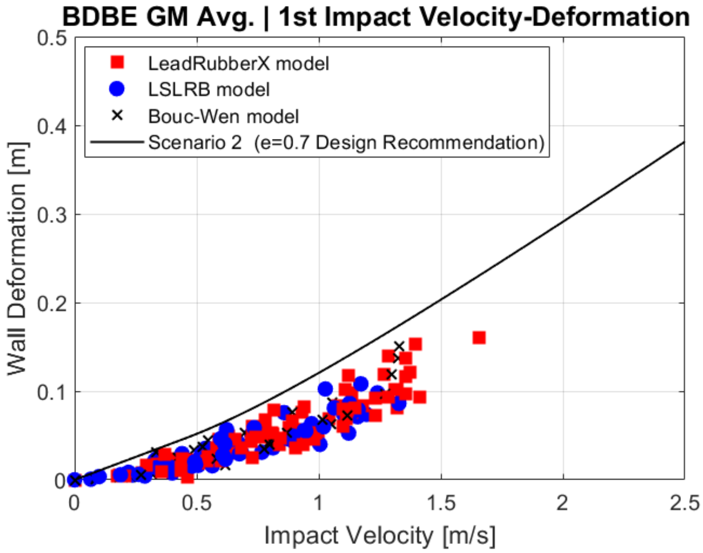

Figure 7-9 Recommendation for prediction of moat wall deformation compared with 1st impacts at different levels of CS for all three models

7-3 Conclusion

The large strain lead rubber bearing (LSLRB) model extended for 2-D simulations is evaluated and compared against other traditional models to determine the response of the archetype nuclear test (ANT) model. Simulations are conducted with and without the moat wall in order to understand the difference in the nonlinear model under both conditions. When comparing the 90th percentile maximum displacements for BDBE ground motions, the LSLRB model achieved displacements comparable to that of the Bouc-Wen (constant characteristic strength) model. The *LeadRubberX* model highly overestimated the displacements compared to the other models and demonstrated high sensitivity to long duration ground motions. The LSLRB model without the moat wall demonstrated no benefits in terms of the maximum rotations of the basemat, however it did not exacerbate the rotational effects. The LSRB model resulted in a base shear of roughly 40% larger compared to the other LRB models for one particular ground motion, and raises awareness of the potential effects of hardening. However the average normalized base shear response for all ground motions are 0.322, 0.320, and 0.261 for the *LeadRubberX*, LSLRB and Bouc-Wen model, respectively. The LSLRB model, in an average sense, does not amplify the maximum normalized base shear.

Since impact to moat walls can amplify the forces on the superstructure, the LRB models were compared considering the moat wall at various clearance to stops (CS). The average velocity at impact for the first three impacts were considered. The CS of 300% shear strain resulted in the largest impact velocities for all models. As the CS was extended to larger shear strains of 350% and 375%, the LSLRB model developed hardening effects reducing velocity at impacts. For CS of 375% shear strain, for the first impact the LSLRB model obtained the lowest average impact velocities compared to that of the Bouc-Wen model demonstrating potential benefits of allowing strain hardening in the rubber prior to impact.

Utilizing the moat wall model and impact deformation procedure from Chapter 5, the design recommendation of accounting for the soil springs and the restitution value 0.7 resulted in a conservative formulation when compared against the OpenSees simulations for all LRB models. The proposed prediction model can function as a design aid although more moat wall configurations should be considered to further verify the model. The average pseudo acceleration with no moat wall was considered, the LSLRB model achieved accelerations comparable to the Bouc-Wen model. When considering a moat wall, the LSLRB model achieved greater reductions in average pseudo acceleration of the superstructure as the CS was extended compared to the *LeadRubberX* and the Bouc-Wen model. Considering the moat wall for CS of 375% shear strain, the LSLRB model provided average response spectra comparable to that of the Bouc-Wen model. For BDBE level shaking, exploring and modeling for these larger levels of shear strain are important to consider for reducing the velocity at impacts and the amount of pseudo accelerations transmitted to the superstructure. These findings coincide with the studies conducted in Chapter 4 and 5 which considered an early version of the model for 1D, observing that the extension of the moat wall to shear strains of 350-375% provide significant reductions in impact velocity and maximum displacements. Furthermore, the extension of the wall not only provides the benefits of reducing impact velocities, provides these benefits without increasing base shear nor base mat rotations and therefore should be further explored.

7-4 References

ASCE. (2017). "Seismic analysis of safety-related nuclear structures, ASCE/SEI Standard 4." American Society of Civil Engineers, Reston, VA.

Fukui, H., Fujitani, H., Mukai, Y., Ito, M., and Mosqueda, G. (2020). "Response Evaluation and Analysis Using Impulse of Base-isolated Buildings during a Collision with Retaining Wall." *Architectural Institute of Japan, Japan Architectural Review*, 66B(3).

Harwood, J. A. C., and Payne, A. R. (1966). "Stress softening in natural rubber vulcanizates. Part IV. Unfilled vulcanizates." *Journal of Applied Polymer Science*, 10(8), 1203–1211.

Kitayama, S., and Constantinou, M. C. (2019). "Effect of displacement restraint on the collapse performance of seismically isolated buildings." *Bulletin of Earthquake Engineering*, Springer Netherlands, 17(5), 2767–2786.

Kumar, M., Whittaker, A. S., and Constantinou, M. C. (2015). *Seismic isolation of nuclear power plants using elastomeric bearings*. *Technical Report MCEER-15-0006*.

Lee, D. M. (1980). "Base isolation for torsion reduction in asymmetric structures under earthquake loading." *Earthquake Engineering & Structural Dynamics*, John Wiley & Sons, Ltd, 8(4), 349–359.

Masroor, A., and Mosqueda, G. (2012). "Experimental simulation of base-isolated buildings pounding against moat wall and effects on superstructure response." *Earthquake Engineering & Structural Dynamics*, 41(14), 2093–2109.

Sarebanha, A. (2018). "Experimental and Numerical Simulation of Seismically Isolated Critical Facilities under Extreme Seismic Loading." University of California, San Diego.

Sarebanha, A., Marquez, J., Hughes, P., and Mosqueda, G. (2021). "Considerations for modeling of base isolated nuclear power plants subjected to beyond design basis shaking." *Nuclear Engineering and Design*, Elsevier Ltd, 379, 111236.

Schellenberg, A., Baker, J., Mahin, S., and Sitar, N. (2014). *Investigation of Seismic Isolation Technology Applied to the APR 1400 Nuclear Power Plant-Volume 2: Selection of Ground Motions*. *Technical Report to KEPCO Engineering and Construction, Pacific Engineering Research Center, University of California, Berkeley, CA.*

Schellenberg, A. H., Sarebanha, A., Schoettler, M. J., Shao, B., Mosqueda, G., and Mahin, S. A. (2016). *Hybrid Simulation of Seismic Isolation Systems applied to an Archetype Nuclear Test (ANT) Power Plant under Design Level Excitation*. PEER.

Shao, B., Mahin, S. A., and Zayas, V. (2017). *Member capacity factors for seismic isolators as required to limit isolated structure collapse risks to within ASCE 7 stipulated structure collapse risk Structural Engineering Mechanics and Materials Member Capacity Factors for Seismic Isolators to Limit*.

U.S. Nuclear Regulatory Commission. (2014). "Design Response Spectra for Seismic Design of Nuclear Power Plants." *Regulatory Guide No. 1.60, Revision 2*.

Chapter 8 SUMMARY AND CONCLUSION

8-1 Summary of Research Work

Seismic isolation is a proven technology in separating the fundamental frequency of a structure from the damaging frequencies of an earthquake, at the expense of concentrated displacements at the isolation level. To accommodate for these concentrated displacements, seismic isolation bearings are designed and tested to sustain the large displacements under the weight of the supported structure. In addition, a large horizontal clearance or a moat is introduced to provide the needed space for the isolation system. A moat wall is inserted around the perimeter and can function as a stop to limit displacements of the bearings to their tested capacity and prevent their failure. This dissertation explores the modeling and application of a common isolation system, the Lead Rubber Bearing (LRB), when subjected to large displacement demands. The LRB is composed of alternating steel and rubber shims with a central lead core insert. The composite rubber and lead exhibit complex behavior with contributions from both materials.

Experiments of a LRB subjected to large cyclic strains demonstrate the complex behaviors of these bearings. Towards the development of more reliable models, a large strain lead rubber bearing (LSLRB) model is proposed that is capable of capturing the observed experimental behavior under large cyclic strains in 1D. The model is then applied to a Nuclear Power Plant (NPP) model in order to identify the effects of the LRB model on the response of the superstructure. The NPP models are considered with and without a moat wall, and the simulations verify that moat wall impact can have significant amplification on the structural response. To better predict the effects of impact, an existing moat wall deformation prediction model is revisited and modified to include the soil contribution and the coefficient of restitution providing a conservative design guideline.

Current seismic isolation design guidelines for NPPs require analysis under high consequence low frequency seismic event, imposing high levels of displacement for the isolation system. The code requires for isolation systems to model the shear forces developed at BDBE demands, however current LRB models did not fully capture the nonlinear behaviors experienced at large strain levels for 2D excitation. The LSLRB model is extended to capture the nonlinear behaviors exhibited under 2D horizontal motion at small to large strains. Additionally, existing isolated buildings having a moat clearance at even moderate levels of strain, typically measured perpendicular to the side of the basemat, and may therefore need to model possible large geometric shear strains at corners, especially for critical structures. The LSLRB model showed to be consistent with other recently proposed models at lower levels of demand. At higher levels of demand, however, the LSLRB model reduced the maximum displacements and impact velocities without significantly increasing the base shear of the NPP model or the basemat torsion. The LSLRB model can more accurately capture the nonlinear effects and therefore provides a more reliable estimate of peak bearing displacements and the velocity at impact to moat walls.

8-2 Contribution to Research

In order to develop a LRB model, various existing models and experimental data on LRBs are examined proving as state-of-art models for LRB. A recently proposed model named *LeadRubberX* utilizes and modifies the Bouc-Wen model to include the lead core strength degradation due to lead core heating. Property modification factors that are used to account for variation in bearing behavior by design codes are evaluated by applying these factors to the material properties of the smooth Bouc-Wen models creating lower and upper bounds (Chapter 3). The models undergo earthquake excitations, and it is found that the *LeadRubberX* model is not conservatively bounded by these modification factors, especially for long duration ground motions.

A parallel model was developed to capture the nonlinear effects observed in LRBs, ranging from small to large shear strains. Experimental tests on large LRBs allowed to deconstrue the various nonlinear behaviors exhibited by the lead core and the rubber (Chapter 4). The lead core exhibited heating causing strength degradation, as well as initial lead hardening phenomenon. The rubber exhibited hardening effects along with softening 'unloading' effects which invoked widening of hysteresis at peak displacements. A SDOF system is considered and compared against typical LRB models demonstrating its effectiveness in reducing displacements and impact velocities.

In Chapter 5, the parallel model is implemented in a full scale NPP model in OpenSees named the archetype nuclear test (ANT) model to observe potential benefits from the nonlinear effects in 1D excitation. The LSLRB model proved to reduce impact velocities along with subsequent impacts. The LSLRB model was able to reduce the average pseudo accelerations in the superstructure as the CS was extended into larger shear strains compared to the other models, reducing by up to 40%. An extension of an existing moat wall deformation prediction model was examined by adding the soil contribution along with a coefficient of restitution. The updated moat wall deformation prediction model demonstrated to conservatively predict the amount of moat wall deformation given an impact velocity, providing a design recommendation.

An extension of the LSLRB model was introduced, providing the ability to account for the various nonlinear behaviors observed in 2D experimental data (Chapter 6). A damage model based on work conducted with high damping rubber (HDR) was utilized and modified due to the commonalities between the natural rubber in LRBs and HDR. A sensitivity study was conducted in order to better understand the effects of model parameters, and to reduce the number of parameters for practicality. Since natural rubber is strain-rate independent compared to HDR, especially for typical strain rate demands of earthquakes, the damage model is modified to become strain-rate independent. The addition of this modified damage model to the LSLRB model, extended the capability of the model to capture the various nonlinear behaviors exhibited in 1D and 2D experimental data. The LSLRB model was examined under various intensity levels compared with current models. At low levels of intensity, the LSLRB model demonstrated to be consistent with the other current models utilized today. At higher levels of intensity, the LSLRB model was able to account for the various nonlinear behaviors developed at large levels of shear strain, demonstrating its versatility and range of applicability. In Chapter 6, the LSLRB model was implemented into the Archetype Nuclear Test (ANT) model in order to exemplify its benefits compared to existing models for 2D excitations at beyond design basis earthquakes. The LSLRB model demonstrated to provide reduced impact velocities and reduce maximum displacements without significant amplification of the maximum base mat rotations nor maximum base shear.

The model proved to reduce impact velocities, as well as, subsequent impacts compared to the other models, specifically, for higher shear strains of 350-375%. The superstructure observed significant benefits with the implementation of the LSLRB model as the moat wall was extended to larger levels of shear strain, achieving reductions in the average pseudo accelerations of about 40% when extended from 325% to 375% shear strain. At 375% shear strain, the LSLRB model obtained an average pseudo acceleration comparable to the constant Bouc-Wen model. Therefore, since LRBs have been shown to withstand large shear strains without failure, extension of the CS to higher levels of shear strains may be beneficial. The LSLRB model has shown to be beneficial for the isolation system and superstructure in avoiding impact or reducing velocities before impact, while at lower levels of intensity performing as typical models perform today. Consistent with 1D, the extended moat wall impact prediction model can provide a conservative prediction for the deformation given an impact velocity.

8-3 Recommendation for future research work

With regards to the investigation of the response of seismically isolated NPP, considering modeling of Lead Rubber Bearings at large strains, this is one of the few studies on this topic. This study provided significant insights into this behavior of LRB and their effect on the superstructure response, however, also revealed several topics that need further study as described below.

- There is limited experimental data on the behavior of LRB under large dynamic cyclic strains. Additional data, especially as related to realistic earthquake excitation could provide the necessary data to fully verify the LSLRB model.

- Due to limitation of experimental data including variable vertical excitation, further investigating into the axial load influence on the hardening effects at large strains is necessary.
- As for the lead core contribution, accounting for the direct relationship between strain-rate and characteristic strength may be of importance in order to verify the lead core heating models.
- Further testing may be needed to completely understand the initial lead core hardening and the core reason for its principal cause to further inform the phenomenological model introduced here.
- Conducting experimental tests on identical LRBs and natural rubber bearings considering various orbital loading types could provide additional data to find the root cause of the inverse reversal loops observed in some tests.
- More studies on various moat wall configurations should be explored in order to provide more confidence in the moat wall deformation prediction provided here.
- Changes in the size of the bearing and shape factors will require recalibration of LSLRB parameters, therefore more LRB test data on various sizes of LRBs may provide a guidance or recommendation of parameters.